

Performance Improvement of Multilevel Load Power System by Using Two-Stages Fuzzy Controller

Baqer Turki Atiyah Al-lamey

Nasseriya Technical Institute

Abstract

This paper presents a new approach to improve the performance of power system by enhancing the voltage profile and reducing the real power losses based on two stages fuzzy controller which is used to select the appropriate size and location of capacitor banks required to minimize the power losses and maintain the voltage profile in permissible limits.

The first stage of fuzzy controller is used to specify the optimal location of capacitors installation, while the optimal size is specified by the second stage. The proposed method is tested on a 34-bus, 74-transmission lines from Iraqi Northern power system with multilevel of loads. The load levels are represented by 50%, 75%, 100% and 125% of peak load and satisfied results are obtained to show the feasibility and flexibility of the proposed method.

Keywords : Load – flow , Fuzzy- logic , optimal ,location , optimal size .

المستخلص

البحث يقدم طريقة جديدة لتحسين أداء منظومة القدرة من خلال تعزيز مقدار الفولتية وتقليل الخسائر بالاعتماد على المسيطر المضرب ذو مرحلتين الذي يستخدم لاختيار القيم المثلى والأماكن المناسبة للتصويب المتسعات اللازمة لتحسين الأداء. المرحلة الأولى من المسيطر المضرب تستخدم لتحديد الأماكن المثلى للتصويب بينما يتم تحديد القيم المثلى للمتسعات باستخدام المرحلة الثانية من المسيطر المضرب. الطريقة المقترحة اختبرت على منظومة قدرة كهربائية مؤلفة من 34- قضيب توصيل عمومي و 74- خط نقل من منظومة شمال العراق بمستويات متعددة من الحمل، مستويات الأحمال التي اعتمدها الدراسة حددت بـ 50%، 75%، 100%، 125% من القيمة القصوى للحمل وتم استحصال النتائج التي بينت فعالية ومرونة الطريقة المقترحة.

1. Introduction

Electricity networks are called to accommodate more and more generation capacity in order to supply the increasing demand. However, social, planning and environmental reasons hinder the expansion of the existing networks, but even where this is possible it raises a tremendous cost for the operator. Therefore, the efficient utilization of the existing transmission and distribution lines is not only suggested for economy, but also imposed by need. Reactor and capacitor banks have long been utilized as a remedy for a series of

technical and economic problems in power systems. Large reactive power surplus or deficiency at light or heavy load operation, respectively, can be tackled with the placement of reactor and capacitors at the appropriate network locations ^[1]. Furthermore, several methods have been suggested for the reduction of transmission losses by the local consumption or production of reactive power from optimally located reactive power compensation banks ^[2]. Finally, a series of methods are attempted to optimally allocate capacitor banks, so that both losses are reduced and power quality is improved, using other inherent capabilities of those elements^[3-5].

In recent years, increased efforts have been centered on developing intelligent control systems that can perform effectively in real-time. These include the development of non-analytical methods of soft computing such as evolutionary computation and fuzzy logic. These methods have proven to be effective in designing intelligent control systems and handling real-time uncertainty, respectively. This paper is an attempt, which is based on fuzzy controller to improve the performance of multilevel power system through voltages profile enhancement and reduced the real power losses by installing capacitor banks on some nodes in that power system.

2. Literature review

Fuzzy set theory applications have received increasing attention in various areas of power systems such as operation, planning and control^[6]. Published literature describes several approaches and techniques to the problem, standing out the analytic methods, heuristic methods, numerical programming, fuzzy logic, ant colony optimization, tabu search, neural networks, genetic algorithms and hybrid methods ^[7]. Mahdad and et.al describe in ^[8] a simple approach based on logic concept. Fuzzy logic approach is described, which achieves a logical and feasible economic cost of operation without the need of exact mathematical formulation. P.V. Prasad and et.al in ^[9], present a novel method to determine suitable candidate nodes in distribution systems for capacitor installation using fuzzy approach and capacitor-sizing problem for loss minimization using Genetic Algorithm method. The proposed method has been tested with several systems.

Tamer Mohamed Khalil and et.al in ^[10], propose a binary particle swarm optimization (PSO) for optimal placement and sizing of fixed capacitor banks in radial distribution lines with nonsinusoidal substation voltages. The objective function includes the cost of power losses and capacitor banks with constraints which include limits on voltage, total harmonic distortion (THD) and sizes of installed capacitors. Housseem Ben Aribia and Hsan Hadj

Abdallah in ^[11], propose an approach based on the evolutionary algorithms (AE) to solve the problem of maintaining an appropriate voltage profile, this task can be done by the minimization of the active losses in the transportation and transmission lines by implantation of reactive power sources to the load buses, in addition to the minimization of the active losses, other criteria can be considered as the compensation devices cost and the voltage deviation.

3. Overview of fuzzy control ^[12, 13]

A fuzzy logic controller (FLC) is an intelligent control system that smoothly interpolates between rules. A fuzzy set may be represented by a mathematical formulation known as a membership function. That is, associated with a given linguistic variable (e.g. speed) there are linguistic values or fuzzy subsets (e.g. slow, fast, etc.) expressed as membership functions which represent uncertainty, vagueness, or imprecision in values of the linguistic variable. This function assigns a numerical degree of membership, in the closed unit interval $[0, 1]$, to a crisp (precise) number. Within this framework, a membership value of zero/one corresponds to an element that is definitely not/definitely a member of the fuzzy set. Partial membership is indicated by values between 0 and 1. Implementation of a fuzzy controller requires assigning membership functions for inputs and outputs. Inputs are usually measured variables, associated with the state of the controlled plant that are assigned membership values before being processed by an inference engine. The heart of the controller inference engine is a set of if-then rules whose antecedents and consequents are made up of linguistic variables and associated fuzzy membership functions. Fuzzy set intersection, or conjunction, operators in the antecedent are generally referred to as t-norms. They commonly employ algebraic *min* or *product* operations on fuzzy membership values. Consequents from different rules are numerically aggregated by fuzzy set union and then defuzzified to yield a single crisp output as the control for the plant.

4. Design of proposed fuzzy controller

The proposed fuzzy controller which is used to specify the optimal sizes and locations of capacitor banks placement consist of two stages which are:-

4.1. First stage fuzzy controller

Fuzzy controller in this stage used to specify the optimal locations which are the capacitor banks installed on it. Node voltages and power loss indices are the inputs to this

fuzzy controller to determine the suitability of a node in the capacitor placement problem. The suitability of a node is chosen from the capacitor suitability index at each node. The higher values of capacitor suitability index are chosen as best locations for capacitor placement. To determine the power loss indices, the power loss reduction is calculated by compensating the self-reactive power at each node at a time by conducting the vector based load flow method. These loss reductions are then linearly normalized into a (0, 1) range with the largest loss reduction having a value of '1' and the smallest loss reduction having a value of '0' for calculation of power loss indices (PLI). Fuzzy variables power losses indices (PLI), voltage in p.u. and capacitor suitability index (CSI) are described by fuzzy terms *low*, *medium-low*, *medium*, *medium-high* and *high*. The fuzzy variables described above are represented by membership functions as shown in Figures (1 and 2). To determine the location of capacitor the voltage and power loss index at each node shall be calculated and represented in fuzzy membership function. By using these voltages and PLI, rules are framed and are summarized in the fuzzy decision matrix as given in Table (1).

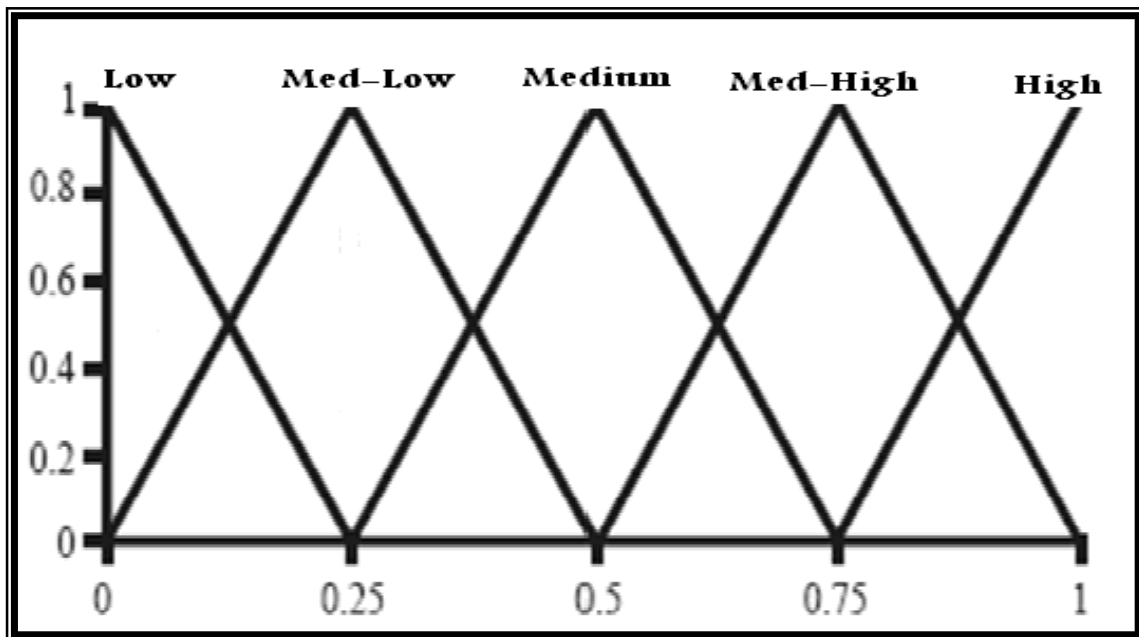


Figure (1). Power losses index and capacitor placement suitability membership functions (1st FLC).

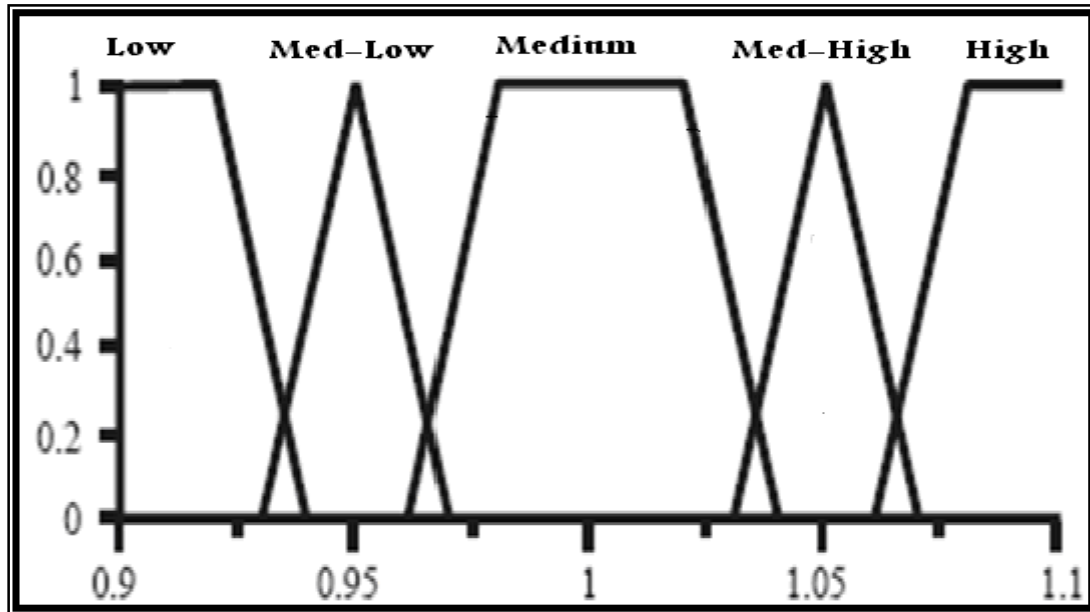


Figure (2). Voltage magnitude membership functions (1st FLC).

Table (1). Decision matrix for determining suitable capacitor location.

DND		Voltage Magnitude				
		Low	Low-Normal	Normal	High-Normal	High
Power Losses Index	Low	Med.- Low	Med.- Low	Low	Low	Low
	Med.- Low	Med.	Med.- Low.	Med.- Low	Low	Low
	Med.	Med.- High	Med.	Med.- Low	Low	Low
	Med.- High	Med.- High	Med.- High	Med.	Med.- Low	Low
	High	High	Med.- High	Med.	Med.- Low	Med.- Low

4.2. Second stage fuzzy controller

Fuzzy controller in this stage is used to specify the optimal sizes which are installed in pre-specified location from first stage fuzzy controller. The inputs to the second stage fuzzy controller are the voltage and load indices, and the output is the size of capacitor in (MVA). The rules in this fuzzy controller are summarized in fuzzy rule table in Table (2), the fuzzy variables; voltage, load, and capacitor size are described by the fuzzy terms; *Down Very Very Small (DVVS)*, *Very Very Small (VVS)*, *Very Small (VS)*, *Small (S)*, *Medium (M)*, *Large (L)* and *Acceptable (A)*. These fuzzy variables described by linguistic terms are represented by membership functions, the membership function are graphically shown in Figures (3, 4

and 5). The construction of these functions can be based on intuition, rank ordering or probabilistic methods ^[13]. The membership functions for describing the voltage have been established based on the ICE standards of acceptable operating voltage ranges for power systems ($1 \pm 5\%$ of *per-unit value* ^[14]). The membership functions for the load and capacitor size are established to provide a ranking. The minimum membership value for the two inputs propagates through the consequent and truncates the membership functions for the consequent of the rule.

Table (2). Decision matrix for determining capacitor size.

AND		LOAD		
		S	M	L
VOLTAGE	VS	VVS	Vs	S
	S	VS	DVVS	S
	M	VVS	VVS	VVS
	L	DVVS	S	VS
	A	None	None	None

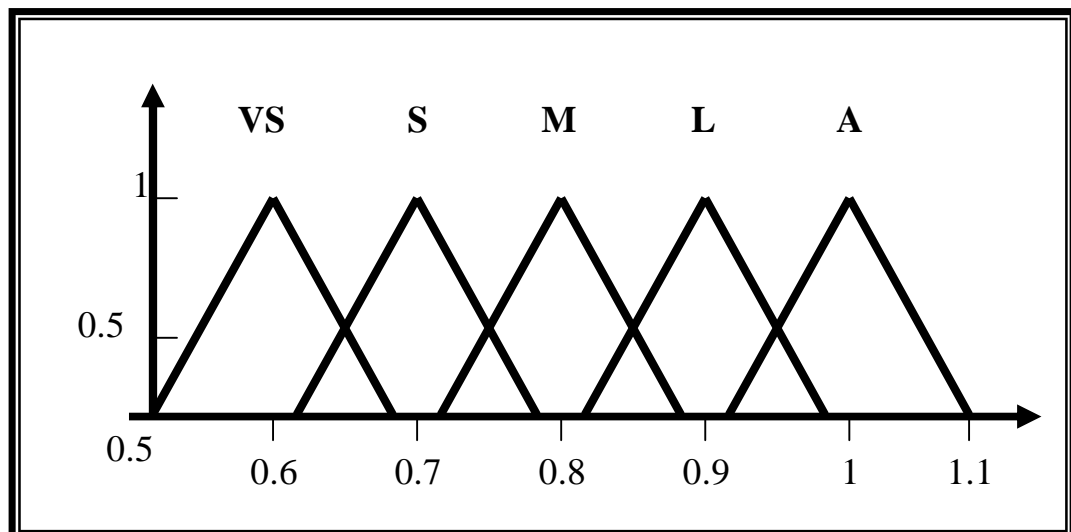


Figure (3). Voltage membership function (2nd controller).

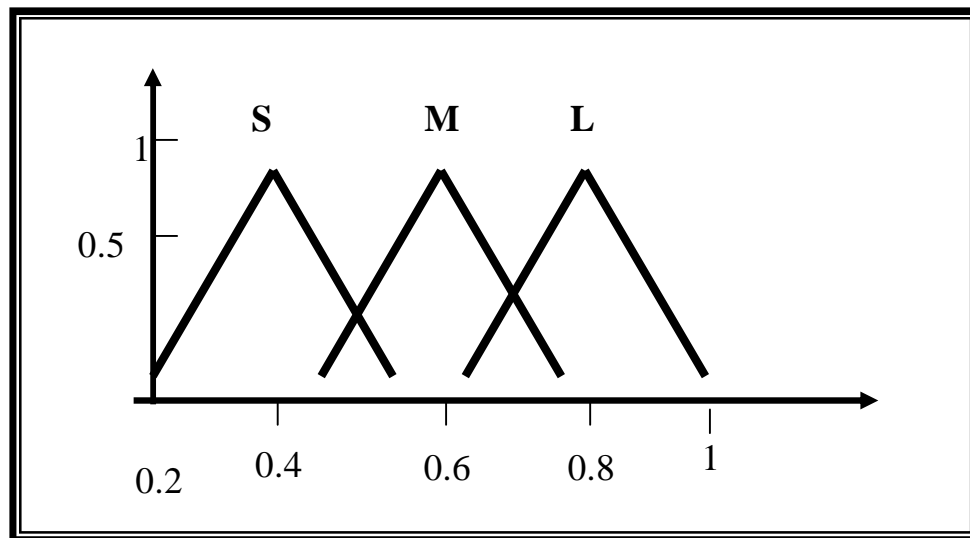


Figure (4). Load membership function (2nd controller).

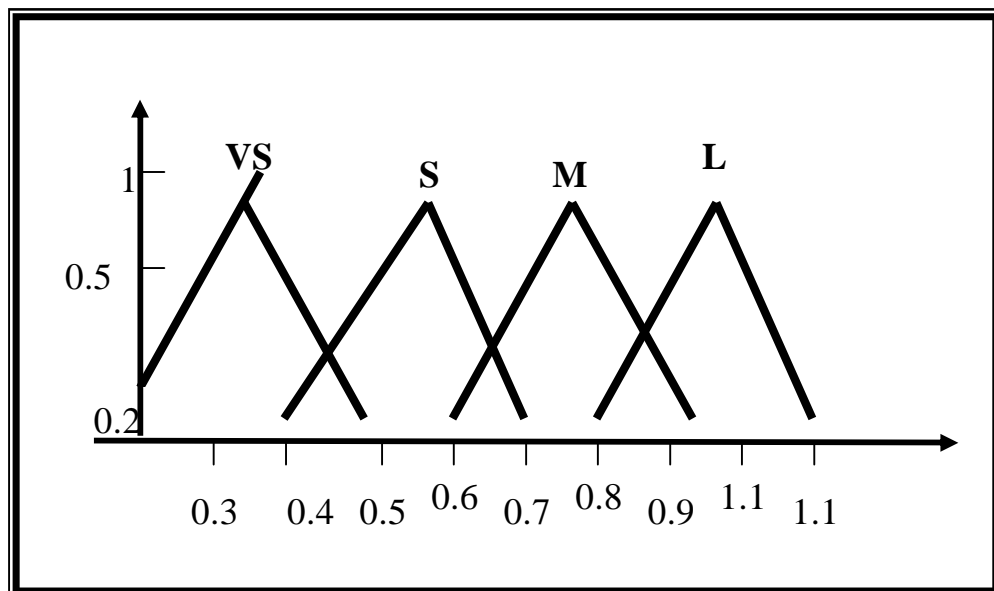


Figure (5). Capacitor size membership function (2nd controller).

5. Fuzzy inferencing and de-fuzzification

After the fuzzy controller receives inputs from the load flow program, several rules may fire with some degree of membership. The MAX-MIN METHOD involves truncating the consequent membership function of each fired rule at the minimum membership value of all the antecedents. A final aggregated membership function is achieved by taking the union of all the truncated consequent membership functions of the fired rules. For the capacitor location problem, resulting capacitor placement suitability membership function, μ_s , of node i for k fired rules is given by:- ^[9]

$$\mu_s(i) = \max_k [\min[\mu_P(i), \mu_V(i)]] \quad (1)$$

Where μ_P and μ_V are the membership functions of the power losses index and voltage magnitude respectively.

For the capacitor size problem, resulting capacitor size membership function, μ_c , of node i for k fired rules is given by:-

$$\mu_c(i) = \max_k [\min[\mu_V(i), \mu_L(i)]] \quad (2)$$

Where μ_V and μ_L are the membership functions of the voltage magnitude and load level respectively.

Once the suitability and capacitor size membership functions of a node is calculated, it must be defuzzified in order to determine the node suitability and size ranking. The centroid method of defuzzification is used; this finds the center of the area of the membership function. Thus, the capacitor suitability and capacitor size indices are determined by:-

$$S \text{ or } C = \frac{\int \mu_{s,c}(z).dz}{\int \mu_{s,c}(z)dz} \quad (3)$$

Where

S, C is the Suitability of optimal location and optimal capacitor size respectively.

$\mu_{s,c}(z)$ is the membership function.

Z is the height of the membership function.

6. Proposed solution method

From studies and experiments with several methods reported in literature, a two- stage fuzzy controller is proposed to solve the problem of voltage collapse and increase in real power losses which effect the performance of power system. First stage fuzzy controller is used to specify the suitability indices of buses, since the buses of highest suitability indices (SI) represent the optimal locations to capacitor placement, the second stage of this fuzzy controller works only with the buses previously selected. The proposed method consists of the following steps:-

- 1- Perform Load-Flow program to calculate bus voltages and power losses considering the original configuration which means without any capacitor installed.
- 2- Bus voltage (BV) is defined for each bus dividing the voltages calculated in step one by the substation voltage.
- 3- Calculate the power losses reduction by injecting the same amount of reactive power at every node of power system.
- 4- The losses reduction calculated by step three are linearly normalized into a "0" and "1" range with the largest losses reduction having a value of "1" and the smallest one having a value of "0", the values between "0" and "1" are the power losses indices (PLI).
- 5- Values which are calculated from steps two and four (BV and PLI) are the input values of 1st stage fuzzy controller to find the optimal locations of capacitor installation which represents the output of this controller.
- 6- After specifying the optimal locations of capacitor installation in steps (1-5), the variables of BV and the amount of load in each load level are processes as input variables to the 2nd stage fuzzy controller to find the optimal sizes of capacitor value in MVA installed in each pre-specified optimal locations. The optimal value of capacitors represents the output of 2nd stage fuzzy controller.
- 7- After finding of optimal sizes and optimal locations by two stages fuzzy controller, the load flow program is then performed again to know the impact of proposed solution method on the real power losses reduction and if the voltage profile within permissible limits ($1 \pm 5\%$ of *per – unit value*) or not.

7. Application

The proposed method is applied to 34-bus, 74- transmission line power system whose single line diagram can be shown in figure (6). This power system is derived from a portion of a transmission power system from Al-Mousel in the north of Iraq found in ^[15]. This power system consists of bus-1 as slack bus, buses 30,31,32,33 and 34 as voltage-controlled buses and buses from 2 to 29 as load buses. The power system under test is subjected to four levels of loads namely Level-1 (50% PL), Level-2 (75%PL), Level -3 (Peak Load) and Level-4 (125%PL). The system parameters and initial buses data are shown in Tables (3-5). ^[15].

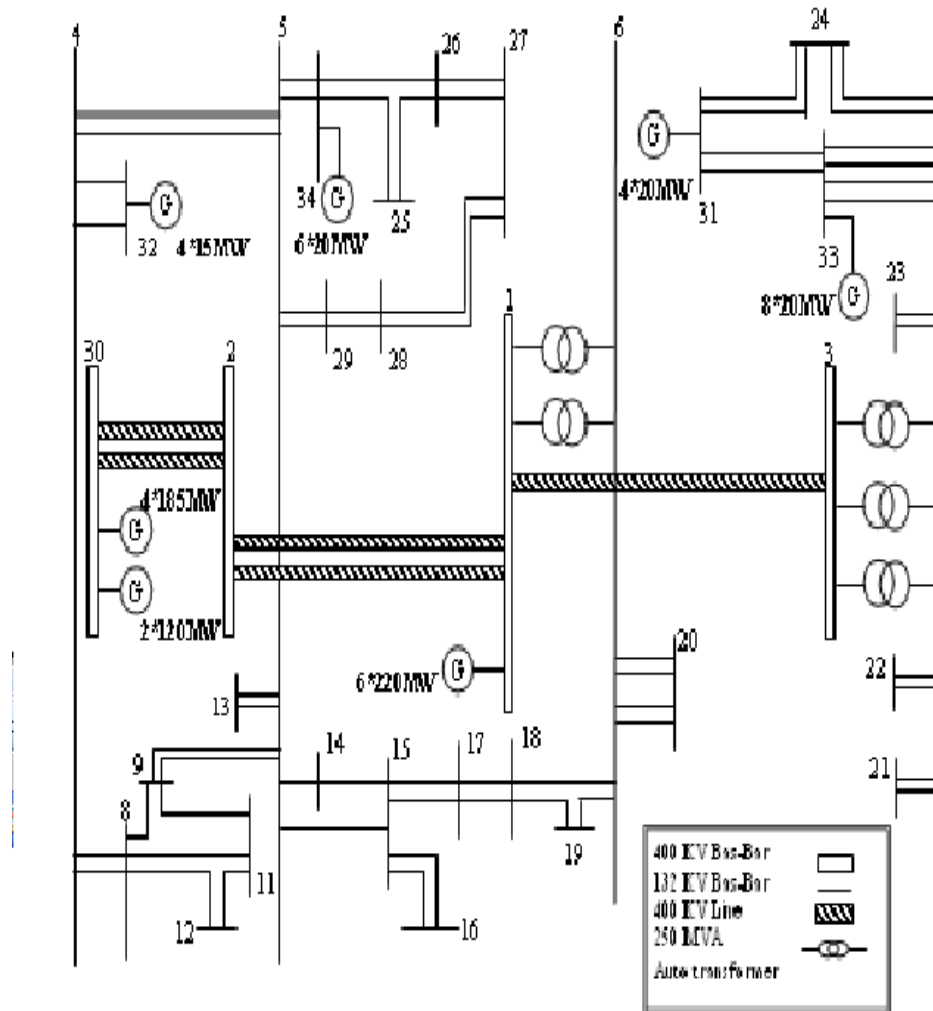


Figure (6). Single line diagram of power system under study . ^[15]

Table (3). Network data .^[15]□

Bus-No	From Bus	To Bus	R (P.U)	X (P.U)	B (P.U)	Length (Km)
1	2	30	0.00143	0.01202	0.3643	63
2	2	30	0.00143	0.01202	0.3643	63
3	2	1	0.004	0.03605	1.068	183
4	2	1	0.004	0.03605	1.068	183
5	1	3	0.00182	0.01654	0.49	84
6	1	6	0	0.036	0	0
7	1	6	0	0.036	0	0
8	2	5	0	0.036	0	0
9	2	5	0	0.036	0	0
10	2	5	0	0.036	0	0
11	3	7	0	0.036	0	0
12	3	7	0	0.036	0	0
13	3	7	0	0.036	0	0
14	4	5	0.0367	0.1465	0.0342	66
15	4	5	0.0367	0.1465	0.0342	66
16	4	32	0.00556	0.0222	0.00518	10
17	4	32	0.00556	0.0222	0.00518	10
18	4	8	0.00725	0.04058	0.01917	26
19	4	8	0.00725	0.04058	0.01917	26
20	5	9	0.0322	0.1288	0.03	58
21	5	9	0.0322	0.1288	0.03	58
22	5	13	0.007	0.0279	0.0065	12.6
23	5	13	0.007	0.0279	0.0065	12.6
24	5	14	0.0247	0.0538	0.0113	23
25	5	15	0.0573	0.1158	0.0238	49
26	5	34	0.0025	0.014	0.0066	9
27	5	34	0.0025	0.014	0.0066	9
28	5	29	0.0016	0.0094	0.0044	6
29	5	29	0.0016	0.0094	0.0044	6
30	6	18	0.0493	0.13615	0.0298	59.5
31	6	19	0.0343	0.09807	0.0216	43
32	6	20	0.0084	0.0229	0.005	10
33	6	20	0.0084	0.0229	0.005	10
34	6	20	0.0084	0.0229	0.005	10
35	6	20	0.0084	0.0229	0.005	10
36	7	21	0.00446	0.0249	0.01179	16
37	7	21	0.00446	0.0249	0.01179	16
38	7	22	0.0118	0.032	0.007	14
39	7	22	0.0118	0.032	0.007	14

Table (3).Continued.^[15]

Bus-No	From Bus	To Bus	R (P.U)	X (P.U)	B (P.U)	Length (Km)
40	7	23	0.0448	0.01215	0.0265	53
41	7	23	0.0448	0.01215	0.0265	53
42	7	24	0.0081	0.0453	0.0214	29
43	7	24	0.0081	0.0453	0.0214	29
44	7	33	0.0169	0.0459	0.01	20
45	7	33	0.0169	0.0459	0.01	20
46	7	33	0.0169	0.0459	0.01	20
47	7	33	0.0169	0.0459	0.01	20
48	8	9	0.0183	0.0732	0.0171	33
49	8	10	0.01337	0.0659	0.0258	38
50	8	11	0.0389	0.01555	0.0362	70
51	8	12	0.0184	0.0859	0.0304	47
52	9	11	0.0205	0.08217	0.0192	37
53	10	12	0.01056	0.0422	0.0098	29
54	14	15	0.0326	0.062	0.0125	26
55	15	16	0.03636	0.0985	0.0215	43
56	15	16	0.03636	0.0985	0.0215	43
57	15	17	0.2114	0.0573	0.0125	25
58	15	17	0.2114	0.0573	0.0125	25
59	17	18	0.03213	0.0871	0.019	37
60	17	18	0.03213	0.0871	0.019	37
61	18	19	0.0169	0.0458	0.01	23.5
62	24	31	0.0515	0.0977	0.0197	41
63	24	31	0.0515	0.0977	0.0197	41
64	31	33	0.01457	0.06411	0.01873	32
65	31	33	0.01457	0.06411	0.01873	32
66	34	25	0.02479	0.0687	0.015	31
67	34	26	0.03128	0.085	0.0185	37
68	25	26	0.0087	0.0251	0.00554	11
69	26	27	0.02114	0.0574	0.0125	25
70	26	27	0.02114	0.0574	0.0125	25
71	27	28	0.00715	0.042	0.202	55
72	27	28	0.00715	0.042	0.202	55
73	29	28	0.00379	0.0212	0.01003	13.6
74	29	28	0.00379	0.0212	0.01003	13.6

Table (4). Load data .^[15]

Bus-No	P (Mw)	Q (Mvar)	Bus-No	P (Mw)	Q (Mvar)
1	0	0	18	37	21
2	595	173	19	35	28
3	0	0	20	172	115
4	0	0	21	89	48
5	0	0	22	63	32
6	0	0	23	32	29
7	0	0	24	104	69.4
8	18	12	25	135	53
9	38	30	26	189	57
10	20	13	27	92	52
11	43	34	28	87	37
12	18	13	29	158.2	56
13	34	24	30	0	0
14	28	22	31	0	0
15	24	20	32	0	0
16	18	10	33	93	61
17	42	26	34	51	27

Table (5). Generators data .^[15]

Base Value (100 MVA)					
Bus-No.	PGi max	QGi min	QGi max	VGi min	VGi max
1	13.2	-2	4	0.95	1.1
30	9.8	-1.5	3.5	0.95	1.1
31	0.8	51-0.	0.25	0.95	1.1
32	0.6	-0.1	0.2	0.95	1.1
33	1.6	-0.2	0.8	0.95	1.1
34	1.4	-0.05	0.5	0.95	1.1

8. Simulation results

An Iterative method of Load-Flow analysis namely Newton-Raphson method is used as a tool to determine the power losses and voltage profile of test power system before and after installing shunt capacitors used to improvement the performance of power system under study. The proposed solution method is based on designing of two-stages fuzzy controller to find the optimal sizes and locations of installed capacitors. The output of 1st stage is the suitability indices of every load buses which are illustrated in Table (6), from this table we find that the optimal locations are Buss 25,26,27 in the first level and Buses 11, 25,26,27,28 in the second level and Buses 11,14,15,16,25,26,27,28 in the third level and 8,11,13,14,15,16,25,26,27,28 in the fourth level due to its highest suitability indices. The output of 2nd stage of designing fuzzy controller is the optimal sizes of capacitors which are illustrated in Table (4). Also the values in Table (7) show that the minimum bus voltages during all four load levels are less than permissible limits of pre-specified minimum allowable bus voltages, then these values became within permissible values after capacitor installation as well as the reduction of real power losses with percentage reduction ratio of 28% in 1st level , 35% in 2nd level, 39.2% in 3rd level and 51.42% in 4th level after the installation process. The differences in the real power system before and after the capacitor placement in all study load level are shown in Figure(7).

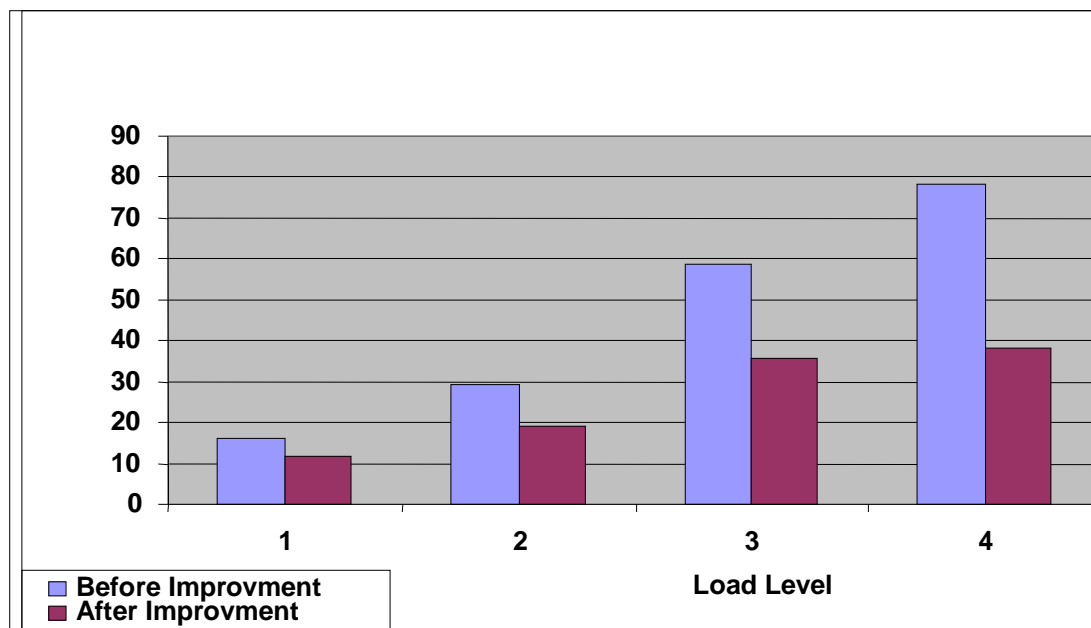


Figure (7). Impact of solution method on power losses reduction.

Table (6). Suitability indices of optimal locations.

Bus No.	Suitability Index of optimal locations			
	Level-1	Level-2	Level-3	Level-4
Bus-2	0.133	0.170	0.203	0.433
Bus-3	0.240	0.315	0.325	0.366
Bus-4	0.185	0.327	0.438	0.345
Bus-5	0.485	0.250	0.438	0.345
Bus-6	0.426	0.320	0.345	0.395
Bus-7	0.285	0.325	0.335	0.413
Bus-8	0.413	0.422	0.439	0.652
Bus-9	0.325	0.388	0.415	0.437
Bus-10	0.24	0.275	0.313	0.417
Bus-11	0.488	0.619	0.625	0.666
Bus-12	0.238	0.326	0.412	0.444
Bus-13	0.335	0.413	0.463	0.736
Bus-14	0.426	0.400	0.776	0.852
Bus-15	0.413	0.390	0.765	0.801
Bus-16	0.400	0.327	0.740	0.810
Bus-17	0.190	0.225	0.250	0.35
Bus-18	0.222	0.250	0.247	0.249
Bus-19	0.312	0.250	0.239	0.246
Bus-20	0.320	0.250	0.313	0.237
Bus-21	0.295	0.245	0.205	0.222
Bus-22	0.315	0.300	0.312	0.381
Bus-23	0.240	0.251	0.255	0.275
Bus-24	0.312	0.285	0.222	0.295
Bus-25	0.710	0.783	0.883	0.950
Bus-26	0.701	0.783	0.883	0.930
Bus-27	0.665	0.755	0.855	0.950
Bus-28	0.239	0.676	0.825	0.925
Bus-29	0.180	0.250	0.247	0.211

Table (7). Simulation results of proposed solution method.

Load Level	Optimal Locations	Optimal Sizes (MVar)	Minimum Voltage (P.U)		Real Power Losses (MW)	
			Before improvement	After improvement	Before improvement	After improvement
Level-1	Bus-25	15.00	0.9240	0.9606	16.3644	11.7730
	Bus-26	15.85	0.9204	0.9576		
	Bus-27	16.15	0.9255	0.9630		
Level-2	Bus-11	18.00	0.9377	0.9690	29.2004	18.9847
	Bus-25	15.00	0.9094	0.9577		
	Bus-26	15.85	0.9036	0.9537		
	Bus-27	16.15	0.9163	0.9509		
	Bus-28	16.50	0.9324	0.9659		
Level-3	Bus-11	18.00	0.9126	0.9511	58.4939	35.5592
	Bus-14	16.50	0.9078	0.9683		
	Bus-15	16.65	0.8765	0.9475		
	Bus-16	18.00	0.8592	0.9625		
	Bus-25	17.50	0.8810	0.9507		
	Bus-26	21.85	0.8723	0.9565		
	Bus-27	18.15	0.8705	0.9505		
	Bus-28	18.50	0.9012	0.9604		
Level-4	Bus-8	19.50	0.8954	0.9687	78.1732	37.9732
	Bus-11	18.00	0.8933	0.9579		
	Bus-13	15.60	0.8722	0.9543		
	Bus-14	16.50	0.8255	0.9265		
	Bus-15	16.65	0.8029	0.9586		
	Bus-16	18.00	0.8974	0.9607		
	Bus-25	17.50	0.8577	0.9573		
	Bus-26	21.85	0.8454	0.9525		
	Bus-27	18.15	0.8370	0.9607		
	Bus-28	18.50	0.8720	0.9511		

9. Conclusions

A simulation program for improving the performance of multi-level load power system by using two-stage fuzzy controller is prepared in the MATLAB-7.5 programming language to specify the optimal sizes and locations of shunt capacitors. The fuzzy logic approach is very appropriate to solve the size, location, and control problem, it is more efficient to solve this kind of problem especially when specialist's knowledge about the problem is included. This paper presents a proposed controller for managing the voltage at the different nodes of multilevel power system; it is based on the fuzzy technique using shunt capacitors. A real case study has been introduced indicating the applicability and effectiveness of fuzzy set theory to

manage the voltage in power systems in addition to reduction of power losses. Fuzzy logic approach reduces the search space and consequently decreases the execution time, increasing the chances to reach the global optimal solution.

10. References

- [1] Elrazaz Z. and Al-Ohaly A. A., July 1993,"Optimal Coordination of Shunt Recators to Enhance System Performance at Light Load Operation.," IEE Proceedings on Generation, Transmission and Distribution, vol. 140, pp. 293-298.
- [2] H. N. Ng, Salama M. M. A., and Chikhani A. Y., January 2000,"Classification of Capacitor Allocation Techniques," IEEE Transactions on Power Delivery, vol. 15, pp. 387-392.
- [3] Martins R. M., Oliveira A. de, and de Paula Silva S. F., 1998,"A New Proposal to Capacitor Bank Allocation Using Fuzzy Logic," presented at International Conference on Power Electronic Drives and Energy Systems for Industrial Growth.
- [4] Masoum M. A. S., Ladjevardi M., Jafarian A., and Fuchs E. F., 2004,"Optimal Placement, Replacement and Sizing of Capacitor Banks in Distorted Distribution Networks by Genetic Algorithms," IEEE Transactions on Power Delivery, vol. 19, pp. 1794-1801.
- [5] Sivanagaraju S., Giridhar M.S., Jagadeesh Babu E., and Srikanth Y., 2004, "A Novel Load Flow Technique for Radial Distribution System", in Proc. National Power System Conference, NPSC-2, IIT Madras, India, pp. 140-144.
- [6] Bansal R.C, Nov.2003,"Bibliography on the Fuzzy Set Theory Applications in Power Systems (1994-2001)", IEEE Trans. Power Systems, Vol. 18, No.4, pp.1291-1299.
- [7] Issicaba D., Bettiol A. L., Coelho J. and Alcantara M. V. P., 2006,"A New Approach for Optimal Capacitor Placement in Distribution Systems", Proceedings of the 6th WSEAS International Conference on Power Systems, Lisbon, Portugal, September 22-24.
- [8] Mahdad B., Bouktir T., and Srairi K., July-December 2005," Dynamic Compensation of the Reactive Energy using a Fuzzy Controller", Leonardo Electronic Journal of Practices and Technologies ISSN 1583-1078 Issue 7.
- [9] Prasad, P.V. , Sivanagaraju, S. and Sreenivasulu, N., June, 2007," A Fuzzy Genetic Algorithm for Optimal Capacitor Placement in Radial Distribution System", ARPJN Journal of Engineering and Applied Sciences, Vol. 2, No. 3.
- [10] Tamer M. K., Hosam K.M. Y. and Abdel A., 13 - 15 June 2006,"A Binary Particle Swarm Optimization for Optimal Placement and Sizing of Capacitor Banks in Radial

- Distribution Feeders with Distorted Substation Voltages", AIML 06 International Conference, Sharm El Sheikh, Egypt.
- [11] Housseem B. A. and Hsan H. A., January-June 2007" Multi Objectives Reactive Dispatch Optimization of an Electrical Network", Leonardo Journal of Sciences, ISSN 1583-0233, Issue 10.
- [12] Ng H. N., Salama M.M. and Chikhani A. Y., January 2000," Capacitor Allocation by Approximate Reasoning: Fuzzy Capacitor Placement", IEEE Transactions on Power Delivery, Vol. 15, No. 1.
- [13] Ross T.J., 1995,"Fuzzy Logic with Engineering Applications", McGraw-Hill Inc.
- [14] Dilek , Murat , 2001" Integrated Design of Electrical Distribution Systems: Phase Balancing and Phase Prediction Case Studies", Ph.D. Thesis, Virginia Polytechnic Institute and State University.
- [15] AL-Suhamei , Wared S.W., 2002," Minimization of Losses In The Iraqi Northern Network of 400Kv &132Kv ", Msc Thesis, College of Engineering, University of Mosul.

Study of Natural Convection in a Horizontal Square Enclosure with 4-Inner Heated Rods

Muneer A. Ismael

Mechanical Engineering Department
College of Engineering
Basra University
muneerismael@yahoo.com

Falah A. Abood

Mechanical Engineering Department
College of Engineering
Basra University

Sana J. Yaseen

Mechanical Engineering Department
College of Engineering
Basra University

Abstract

Laminar, natural convection heat transfer of air filling horizontal space between isothermal (cold) square enclosure and four isothermal (hot) cylindrical rods has been theoretically studied. Finite element method has been used to solve the conservation of governing equations by using software package (FlexPDE).

Parametric study has been conducted for the range of Rayleigh number $10^3 \leq Ra \leq 10^5$, Aspect ratio $0.11 \leq AR \leq 0.28$. Results are presented in the form of streamlines, isotherms contours and Nusselt numbers. Results showed that the overall heat transfer increases with increasing of both Ra and AR. The values of mean Nusselt numbers are compared with data reported in Ref. [6] and [15], and good agreement has been achieved.

Keywords: Natural convection, square enclosure, penalty.

دراسة نظرية للحمل الحر داخل فجوة أفقية مسخنة بأربعة قضبان أسطوانية

المستخلص

تم في هذا البحث دراسة نظرية لانتقال الحرارة بالحمل الحر الطبقي لهواء داخل فجوة أفقية بين أربعة قضبان اسطوانية مسخنة بدرجة حرارة ثابتة موضوعة داخل وعاء مربع الشكل معرض لدرجة حرارة ثابتة (بارد). استخدمت طريقة العناصر المحددة بمساعدة الحقيبة البرمجية (Flex PDE) لحل معادلات الحفظ الحاكمة. كانت قيم المتغيرات لرقم رايلي تتراوح بين 10^3 الى 10^5 وقيم النسبة الثابتة من قطر الانبوب الى طول ضلع المربع Aspect ratio D/L تتراوح بين 0.11 الى 0.28. مثلت النتائج بواسطة خطوط الجريان والتحرار ورقم نسلت حيث أظهرت النتائج تحسن انتقال الحرارة مع زيادة كل من Ra و AR. قورنت النتائج لمعدل رقم نسلت مع النتائج المنشورة في [6] و [15] وظهرت توافقاً جيداً.

1. Introduction

The flow and thermal fields in enclosed space are of great importance due to their wide applications such as in solar collector-receivers, insulation and flooding protection for buried pipes used for district heating and cooling, cooling systems in nuclear reactors, etc. Large numbers of researches were published in the past few decades. Concentric and eccentric cases in a horizontal annulus between two circular cylinders have been well studied. The extensive research studies using various numerical simulations reported by ^[1-5] ensure that several attempts have been made to acquire a basic understanding of natural convection flows and heat transfer characteristics in an enclosure. Shu et al ^[6] studied numerically the natural convection in an eccentric annulus between a square outer cylinder and a circular inner cylinder using Different Quadrate (DQ) method, a symmetric study is conducted for the analysis and thermal fields at different eccentricities and angular positions. Shi and Khodadi ^[7] indicated that a partition attached to the heated vertical wall of square cavity degraded the heat transfer capacity on the wall of the cavity. The work of ^[8] also considered the natural convection in a square cavity with special side-wall temperature variation. Wu and Ching ^[9] investigated experimentally a square cavities with a temperature difference a cross the top and bottom walls. They found the flow pattern in the partitioned cavity was dependent on the top wall temperature of the cavity, the partition height and partition location. Mobedi ^[10] used the heat line technique to observe heat transport in the entire domain of a square cavity with thick horizontal walls. Recently, the heat line and streamline formulations were employed by ^[11] to demonstrate the heat flow for differentially and distributed heating walls with cavities. Wu and Ching ^[12] studies were on partitioned cavities with temperature difference in both horizontal and vertical directions, although results from cavities with smooth walls suggest of a partitioned square cavity. However, in the present research, the effect of four inner rods aspect ratio on natural convection heat transfer is to be studied for different Rayleigh numbers. The tool of investigation is finite element method implicated in a Flex PDE software package.

2. Governing equations

A schematic view of a horizontal space between a square enclosure and 4-inner cylindrical rods is shown in Fig.1. Heat is generated uniformly in the circular inner rods. Thermo physical properties of the fluid in the flow model assumed to be constant except the density variations causing a body force term in the momentum equation. The Boussinesq approximation is invoked for the fluid properties to relate density changes, and to couple in

this way the temperature field to the flow field. The governing equations for the steady natural convection flow using conservation of mass, momentum and energy can be written in the dimensionless form as:

$$\frac{\partial U}{\partial X} + \frac{\partial V}{\partial Y} = 0 \quad (1)$$

$$U \frac{\partial U}{\partial X} + V \frac{\partial U}{\partial Y} = -\frac{\partial P}{\partial X} + \frac{\partial^2 U}{\partial X^2} + \frac{\partial^2 U}{\partial Y^2} \quad (2)$$

$$U \frac{\partial V}{\partial X} + V \frac{\partial V}{\partial Y} = -\frac{\partial P}{\partial Y} + \frac{\partial^2 V}{\partial X^2} + \frac{\partial^2 V}{\partial Y^2} + \left(\frac{Ra}{Pr}\right)\theta \quad (3)$$

$$U \frac{\partial \theta}{\partial X} + V \frac{\partial \theta}{\partial Y} = \frac{1}{Pr} \left(\frac{\partial^2 \theta}{\partial X^2} + \frac{\partial^2 \theta}{\partial Y^2} \right) \quad (4)$$

Non-dimensional parameters can be given as follows

$$X = \frac{x}{L}, \quad Y = \frac{y}{L}, \quad U = \frac{uL}{\nu}, \quad V = \frac{vL}{\nu}, \quad \theta = \frac{T - T_o}{T_i - T_o}, \quad P = \frac{(p + \rho gy)L^2}{\rho \nu^2}, \text{ Prandtl number}$$

$$Pr = \frac{\nu}{\alpha} \text{ and Rayleigh number } Ra = \frac{g\beta(T_i - T_o)L^3}{\nu\alpha}$$

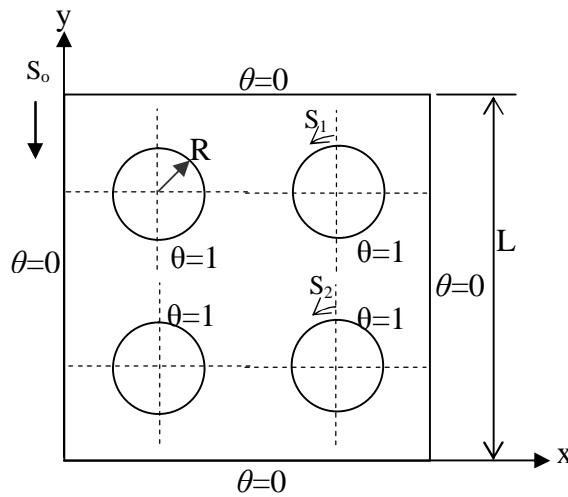


Figure (1). Schematic diagram of the physical domain.

The following Boundary conditions are used:

- 1- Isothermal surfaces i.e. $\theta=1$ on the inner rods walls and $\theta=0$ on the outer square walls.
- 2- No-slip velocity boundary condition, $U=V=0$ on all solid walls.

3- Pressure gradient normal to all surfaces is zero, $\frac{\partial P}{\partial n} = 0$ where n is normal unit vector.

Here X and Y are dimensionless coordinates varying along horizontal and vertical directions respectively; U and V are dimensionless velocity components in the X and Y directions, respectively. θ is the dimensionless temperature; P is dimensionless pressure.

3. Numerical solution

The momentum and energy balance equations are solved using finite element software Package (FlexPDE) ^[13]. The continuity Equation (1) is to be used as a constraint due to mass conservation and this constraint may be used to obtain the pressure distribution ^[14]. In order to solve Equations.(2)-(4), we use a penalty parameter and the incompressibility criterion by Equation.(1) which results in:

$$\nabla^2 P = \lambda \left(\frac{\partial U}{\partial X} + \frac{\partial V}{\partial Y} \right) \quad (5)$$

λ is a penalty parameter that should be chosen either from physical knowledge or by other means^[12]. A most convenient value for λ was attained in this study to be $(10^{11} * \mu/L^2)$. The numerical solutions are obtained in terms of velocity components (U, V) and the stream function (ψ) is evaluated using the relationship between the stream function (ψ) and velocity components (U, V) as:

$$\frac{\partial^2 \Psi}{\partial X^2} + \frac{\partial^2 \Psi}{\partial Y^2} = \frac{\partial U}{\partial Y} - \frac{\partial V}{\partial X} \quad (6)$$

It may be noted that the positive sign of ψ denotes anti-clockwise circulation and the clockwise circulation is represented by the negative sign of ψ .

The no-slip condition is valid at all solid boundaries as there is no cross-flow, hence $\psi=0$ is used for the solid boundaries.

The heat transfer coefficient in terms of the local Nusselt number Nu_L along the inner rod surface and the outer wall is defined by:

$$Nu_L = -\frac{\partial \theta}{\partial n} \quad (7)$$

Where n is the normal direction on a plane. At steady- state it is obvious that the mean Nusselt numbers along both the inner and outer walls are exactly identical. Hence, the average Nusselt number can be evaluated along the outer wall only as:

$$Nu_m = \frac{1}{S_o} \int_{S_o} Nu_L ds_o \quad (8)$$

4. Validations

4.1 Software validation

To check the validation of the software, the grid dependency and the continuity equation in addition are checked. The obtained results showed an exactly validation of the velocity distribution for a grid size obtained by imposing an accuracy of 10^{-4} . This accuracy is a compromised value between the results accuracy and the time consumed in each run. The girded domain for the enclosure of AR=0.23 is shown in Figure (2a) and the distribution of the values of $(\partial U/\partial X + \partial V/\partial Y)$ over the domain, is presented in Figure (2b).

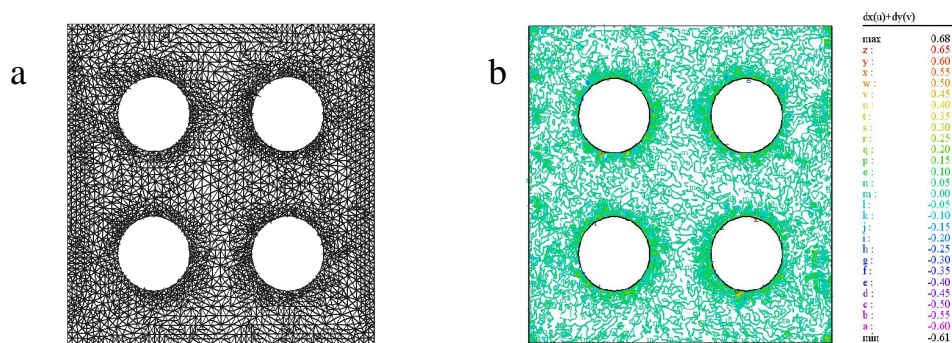


Figure (2). (a) Grid distribution over the domain (b) Validation of continuity equation, for 10^{-4} accuracy.

4.2 Validation of numerical results

In order to validate the employed numerical method more and more, results are obtained and compared with some reported data and found in good agreement. In the work of [6] work of [15], a single circular inner heated rod was concentrically located inside a square enclosure. The average Nusselt number Nu_m along the outer wall between the present work and the work of [6] is compared for $Ra=10^4$, $Pr=0.71$ for different values of $(RR = L/2R)$ equal to 1.67, 2.5 and 5 as shown in Table (1). From this table, it can be seen that the present results generally agree well with that reported in [15] and very well with [6].

Table (1). Comparison of Nu_m between the present work and the works of ^[6] and ^[15] for $Ra=10^4$

L/D	Nu_m (present)	Nu_m ^[6]	Nu_m ^[15]
1.67	5.386	5.395	5.82
2.5	3.282	3.245	3.331
5	2.229	2.082	2.071

5. Results and discussion

5.1 Analyses of flow and thermal fields

To evaluate the aim of the present study, the streamlines, isothermal lines, and local and average Nusselt numbers were visualized and examined for different cases composed of different Rayleigh numbers ($Ra=10^3$ - 10^5) and different aspect ratios ($AR= 0.11, 0.16, 0.23, 0.28$).

The streamlines inside the enclosure of $AR=0.23$ are presented in the left side of Figure (3) for three values of Ra . At $Ra=10^3$, Figure (3a), six circulation cells are formed inside the enclosure. Four of them are localized in each space between each rod and enclosure corner. The other two circulation cells are more strength and localized near the mid span of each vertical wall. The mechanism of forming the circulation is that the hot fluid is pumped from the heated surfaces and mixes with surrounding cold fluid especially that near the cold walls. The clockwise circulation has the negative sign and the anticlockwise circulation have positive sign. The number of circulation cells decreases when Ra increases as shown in Figure (3b) where it can be seen that cells in the upper two corners begin to fusion with the two strong cells localized in mid span of vertical walls. Due to the increase of convection effect here ($Ra=10^4$), it can be seen that the strength of circulation is higher than that of the above ($Ra=10^3$) approximately by a factor of 10. When Ra is further increases to 10^5 , the circulation becomes stronger and more effective inside the enclosure as shown in Figure (3c) where the convection heat transfer is dominated over the conduction.

The isothermal lines for the same above parameters are gathered in the right side of Figure (3). According to the mechanism of fluid moving from around hot surfaces that previously mentioned, equivalent four plumes like distribution are jut out from the space between each two rods towards the enclosure center. This scenario is only observed at low Rayleigh number ($Ra=10^3$, Figure (3a) right). At high Ra ($Ra=10^4$), upper plum like diminishes, the two side plume like remain unchanged while the lower one is more arise towards the enclosure center. At higher Ra ($Ra=10^5$, Figure (3c) right), the lower plume

becomes more dominated in such a way it overcomes the other three plumes where the upper plume completely diminishes. This is an indication to the convection domination.

The effect of aspect ratio on the enclosure thermal performance is displayed in Figure (4) where the isotherms (right) and streamlines (left) are visualized for three aspect ratios ($AR=0.16, 0.23$ and 0.28) all for $Ra=10^4$. The effect of aspect ratio on the streamlines is shown in left side of Figure (4) where it can be seen that at lower aspect ratio ($AR=0.16$) the streamlines become more dense and an additional two cells are formed in the upper part of enclosure because of the available space which permits to fluid to freely circulate. Also it can be seen that the magnitude of stream function decreases with increasing the aspect ratio. This can be attributed to the lack in the space required to fluid circulation at higher AR . On the other hand, the isothermal lines (right side of Figure (4)) give more clarification to the above attribution where at higher aspect ratio the isothermal lines become more parallel and concentrated in the space between the rods and the outer wall of the enclosure.

5.2 Nusselt number

The distribution of local Nusselt numbers are examined along the circumference of inner rods and along the enclosure outer surfaces as follows: Figure (5) shows the variation of the local Nusselt number along the upper right rod for $AR=0.23$ and different Ra 's. As can be seen from this figure, for $Ra=10^3$ at the upper point of the rod, the value of Nu_L increases with increasing of Ra and for $Ra=10^4$, the distribution of local Nusselt number Nu_L is similar where it reaches its minimum value at $S_1=0.375$ and increases sinusoidally otherwise. At $Ra=10^5$, the distribution slightly differs, where along the segment $S_1=0.25-0.5$ we have larger values of Nu_L than that of low Ra and lesser otherwise. This is due to the plume like distribution of the isotherms through the space between the heated rods is greatly spread at high Ra due to the increase of the streamlines strength which dominates the convection. This scenario is clearly characterized from the isothermal lines of Figure (3). Where it is clear that the temperature gradient is minimum at $S_1=0.375$ for $Ra=10^3$ and $Ra=10^4$, and at $S_1=0.16$ for $Ra=10^5$. The Nusselt number Nu_L is proportional to temperature gradient; hence it will follow this variation in temperature gradient. The distribution of Nu_L along the lower right rod for the same parameters mentioned above is shown in Figure (6). The curves have a similar bell shape with one peak except at $Ra=10^5$ where two peaks are noticed. The values of Nu_L are increased with increasing Ra . For $Ra=10^4$, the Nu_L reduces from the top point $S_2=0$ to $S_2=0.375$ due to the domination of conduction heat transfer, then it increases gradually at the rod lower half part to make maximum values along the segment $S_2=0.5-0.75$. This may be

attributed to the enhancement of heat transfer process. For $Ra=10^5$, a similar trend is seen except it has two maximum peaks, one at the bottom point ($S_2=0.5$) and the other at the right point ($S_2=0.75$).

The minimum value of Nu_L appears at the point corresponding to the lower right corner of the enclosure ($S_2=0.675$). Figure(7) shows the Nu_L distribution along the outer boundaries of the enclosure for the same above parameter. For $Ra=10^3$ and 10^4 , the distribution exhibits the same form, namely sinusoidal behavior with four M shaped peaks. Each peak is corresponding to one wall of the enclosure. Each zero value of Nu_L is corresponding to one corner. When Ra increases to 10^5 , the behavior is completely differing from the lower Ra 's. The vertical walls (left, $S_0=0-0.25$ and right, $S_0=0.5-0.75$) have the same behavior. The base ($S_0=0.25-0.5$) has a strong M shape and the lowest values of Nu_L due to the separation of isothermal lines between two lower rods and make a plume like distribution which in turn dominate the convection at the enclosure center and conduction near the bottom wall as can be seen from Figure3c right. The upper wall has sinusoidal distribution with very high values of Nu_L where it double times larger than other walls. This can be demonstrated by the steep temperature gradient along the upper wall of enclosure as in Figure(3c) right.

The effect of aspect ratio on Nu_L is studied by examine the variation of Nu_L for three values of $AR=0.16$, 0.23 and 0.28 , with $Ra=10^4$. Figure (8) shows the variation of Nu_L along the upper right rod. A sinusoidal behavior is seen with all these aspect ratios. The interpretation of maximum and minimum regions of Nu_L is the same that discussed in Figure (5). But it can be seen from this figure that the values of Nu_L of $AR=0.16$ are higher than of $AR=0.23$ along all surfaces of the upper rod except that along the segment $S_1=0.5-0.75$ (where the value of Nu_L are approximately the same). This behavior is attributed to the following: at low aspect ratio, the surface area of the cylinder is reduced and these surfaces become farther from the cold outer walls of enclosure, hence the density of streamlines and flow strength here are higher as shown in Figure (4a) left when it compared with Figure (4b) left. From this figure also, it can be seen that the distribution of Nu_L for $AR=0.28$ has different localizations of maximum and minimum values. This due to that the hot surfaces become closer to each other and closer to the cold walls leading to high temperature gradients. Regarding with lower right rod Figure (9), we can say that the same reason above is the cause of alterations in the Nu_L values with aspect ratio, but the locality of this rod is the cause of the different localization of maximum and minimum values of Nu_L .

The effect of aspect ratio on Nu_L is greatly clarified in Figure (10) which shows the distribution of Nu_L along the outer walls of the enclosure. It appears from this figure how Nu_L

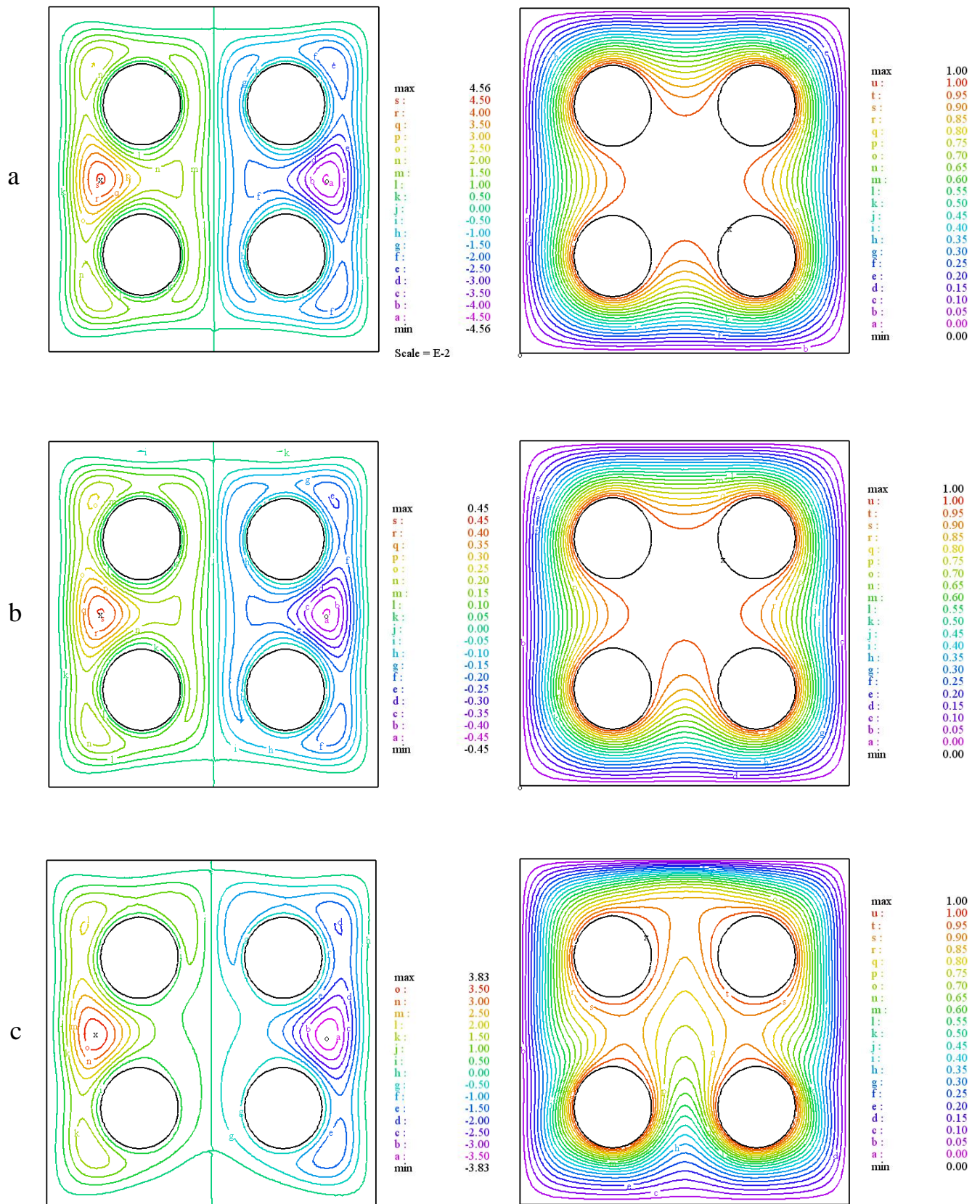
increases as AR increases. A general insight to this figure shows a repeated M shaped distribution along each flat wall of the enclosure. At the enclosure upper wall ($S_o=0.75-1.0$), the recorded Nu_L values are greater than otherwise especially at lowest aspect ratio. This may be attributed to that the moving up stream in low AR is dominated over that moving towards other walls. The M shape distribution is originated due to the reduction in temperature gradient between the walls (left, bottom, right and upper) and the space between the two neighboring rods i.e. the space of plume like origin as can be seen in isothermal lines of Figure (4) right.

Finally, the effect of the parameters under scope (Ra and AR) on the global heat transfer process is plotted in Figure (11) and Figure (12) respectively. It can be seen from these two figures that the mean Nusselt number is an increasing function of both Ra and AR. However it is well known that increasing Ra leads to a good mixing inside enclosure resulting in strong convection. On the other hand and as previously mentioned, increasing aspect ratio means two things, first; increasing the surface area of heating say element and second; nearness of the hot surfaces closer to the cold surface. Also it is worth mentioning to explain that at higher aspect ratio (large rods), and at higher Rayleigh number the wakes forming on the top of rods become larger i.e. separating of the fluid near the rod surfaces become earlier resulting in a good mixing which in turn increase the heat transfer.

6. Conclusions

The natural convection inside a square enclosure heated by four inner rods placed at equal distances from the enclosure center was studied numerically using a Galarkin finite element software package. The effects of aspect ratio (0.11-0.28) and Rayleigh number (10^3 - 10^5) on the heat transfer process were conducted. The following concluding remarks could be extracted from the obtained results:

- 1-As it expected and common reported in the literature, the stream function and the average Nusselt number are increasing functions to Rayleigh number.
- 2-The convection heat transfer could be enhanced by increasing the aspect ratio i.e. by increasing the surface area of the heated rods.
- 3- The effect of Rayleigh number on the mean Nusselt number is more significant at the lower aspect ratios.
- 4- Within the studied ranges of Rayleigh numbers and aspect ratios, the enhancement of mean Nusselt number due to the aspect ratio is more than that due to Rayleigh number.



Figure(3). Streamlines (left) and isotherms (right) for AR=0.23, (a) $Ra=10^3$, (b) $Ra=10^4$, (c) $Ra=10^5$.

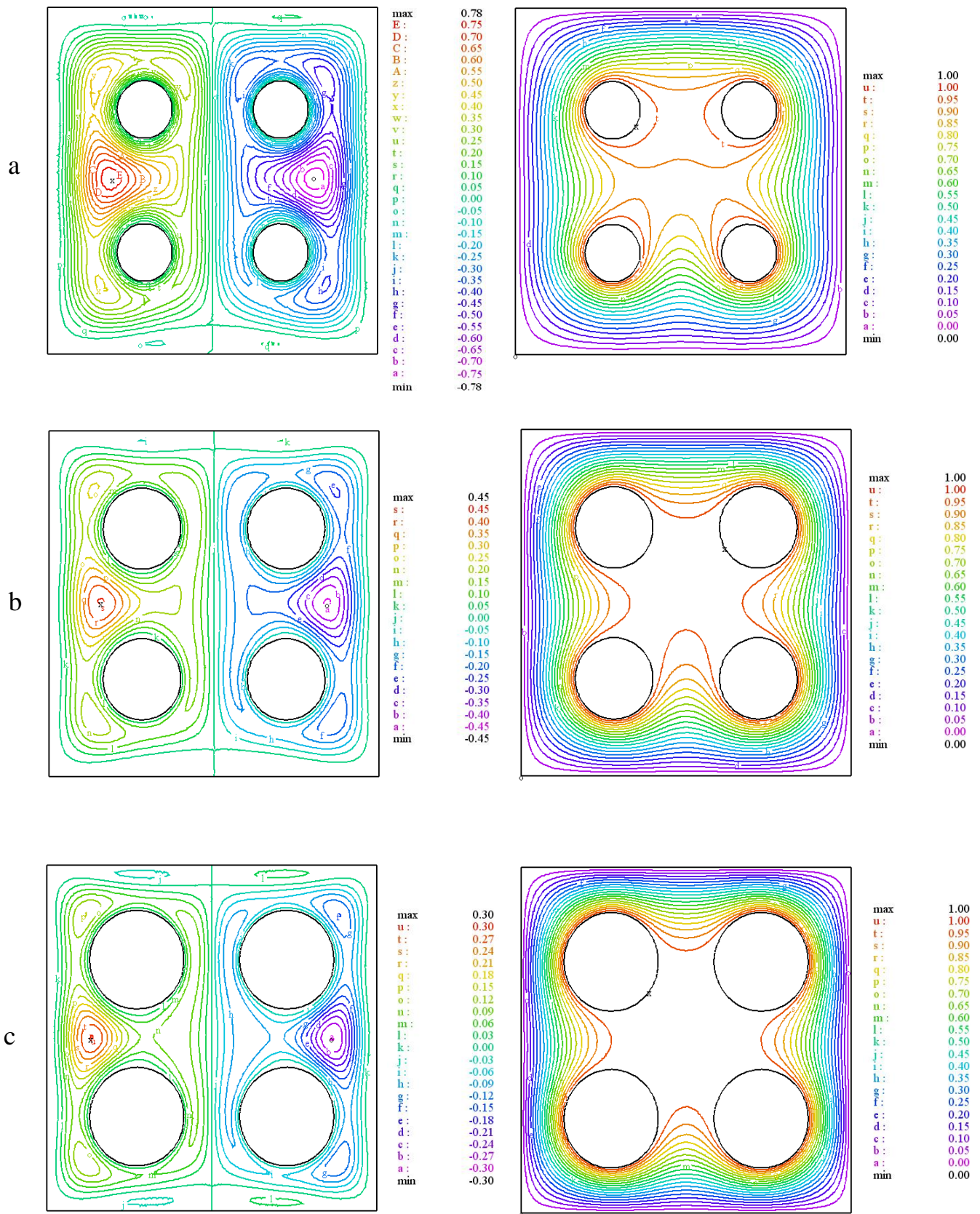


Figure (4). Streamlines (left) and isotherms (right) for $Ra=10^4$ (a) $AR=0.16$, (b) $AR=0.23$ (c) $AR=0.28$.

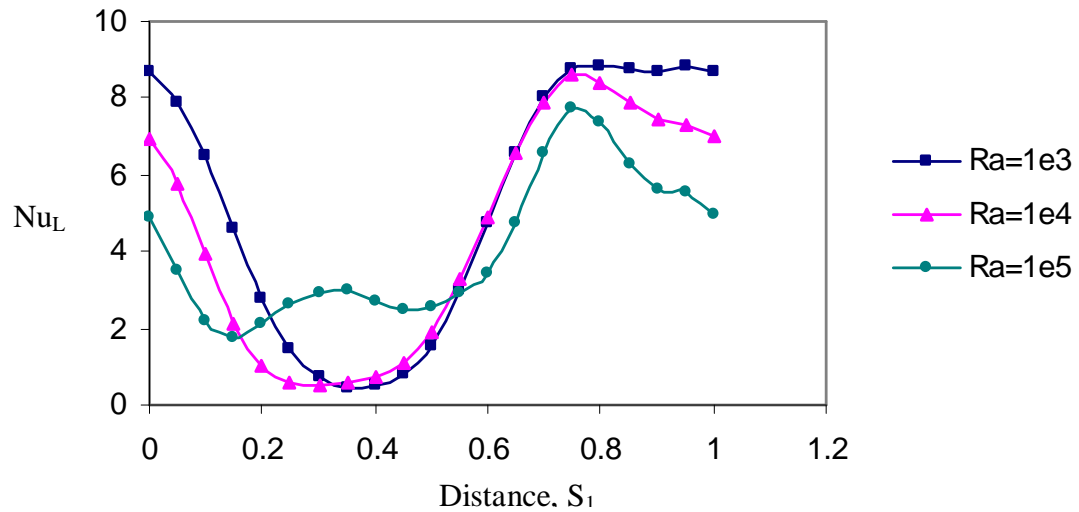


Figure (5). Variation of the local Nusselt number along the upper rod , $AR=0.23$.

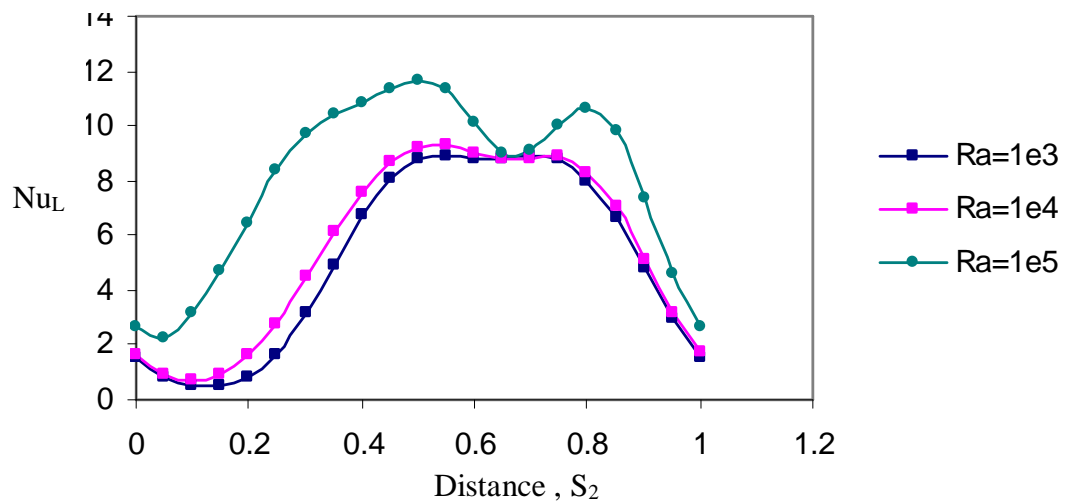


Figure (6). Variation of the local Nusselt number along the inner rod , $AR=0.23$.

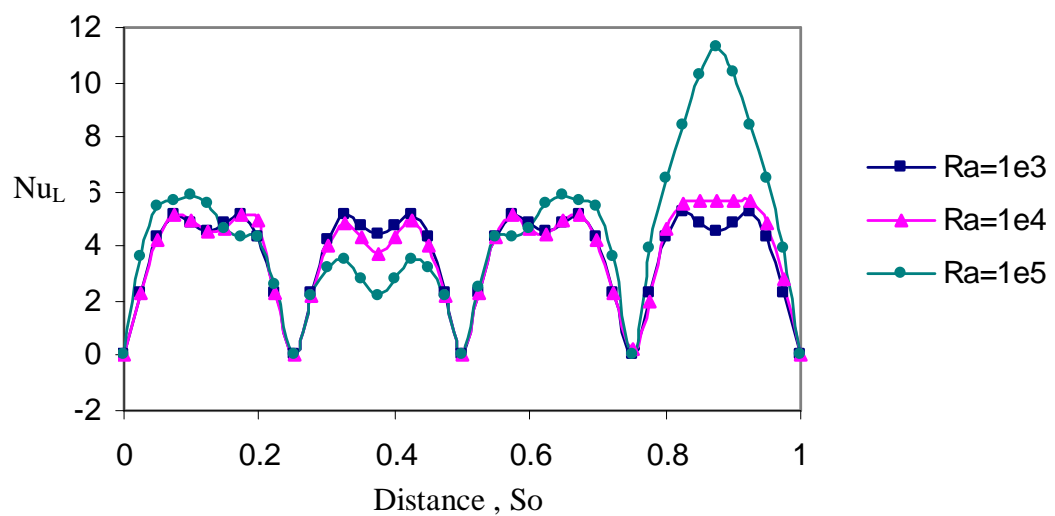


Figure (7). Variation of the local Nusselt number along the outer wall , $AR=0.23$.

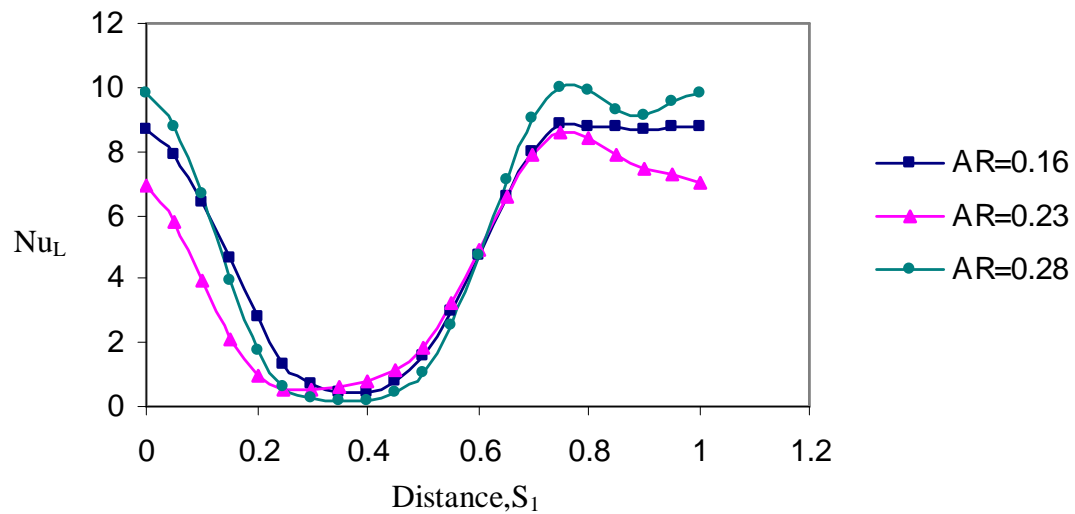


Figure (8). Variation of the local Nusselt number along the upper rod , $Ra=10^4$.

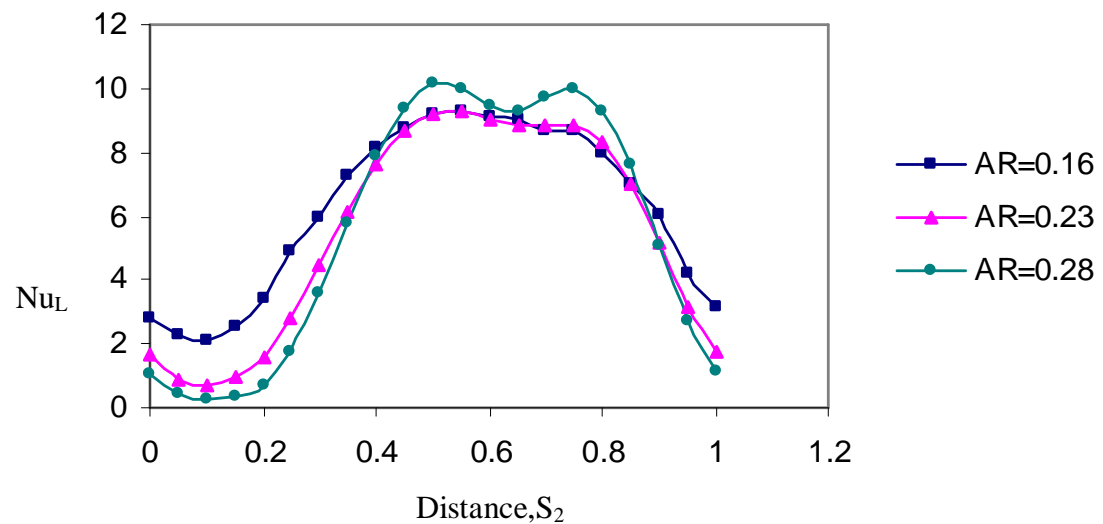


Figure (9). Variation of the local Nusselt number along the lower rod, $Ra=10^4$.

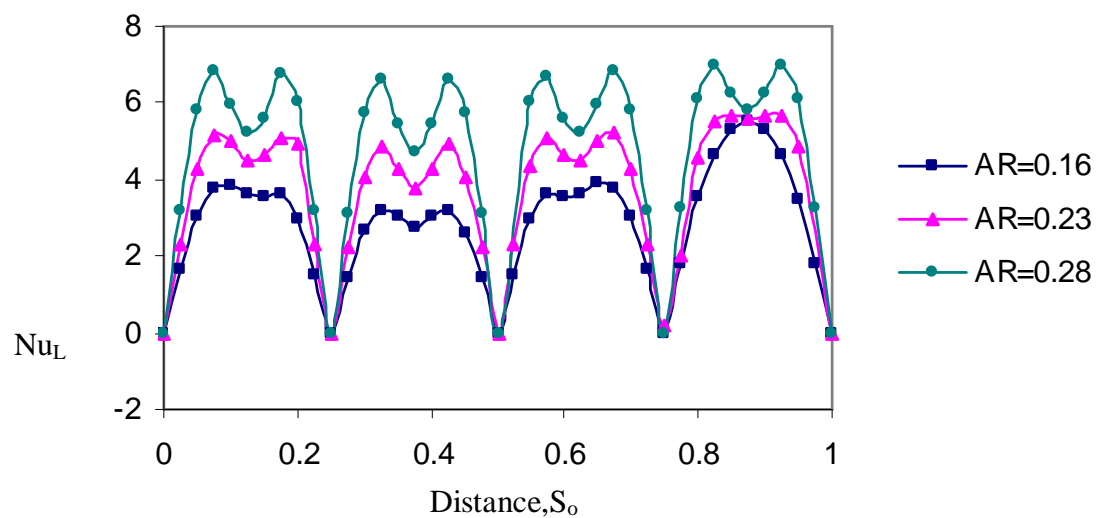


Figure (10). Variation of the local Nusselt number along the outer wall, $Ra=10^4$.

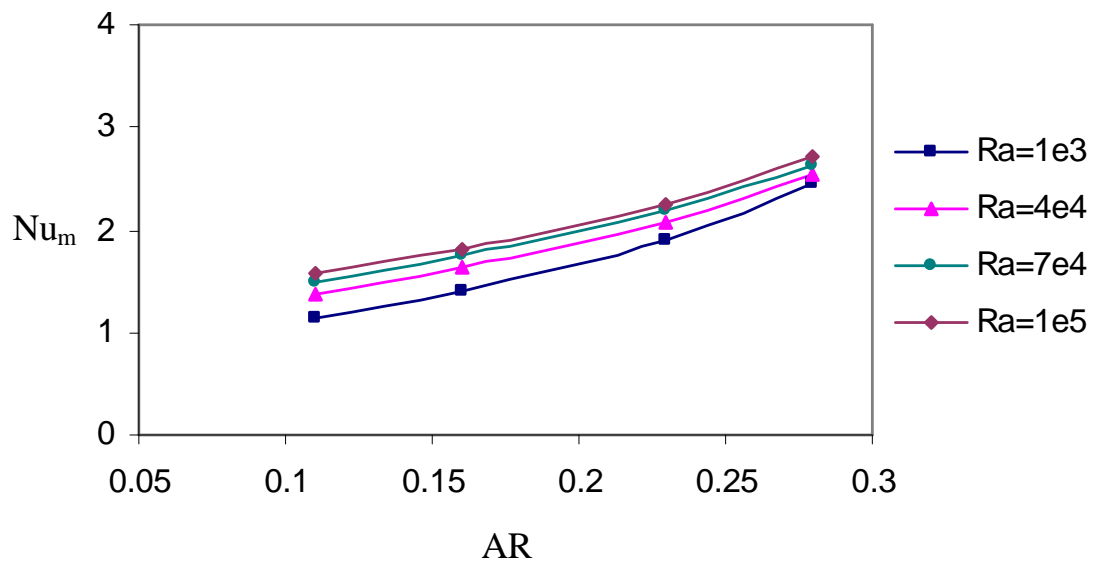


Figure (11). Variation of the mean nusselt number with aspect ratio along the outer wall for different Rayleigh numbers .

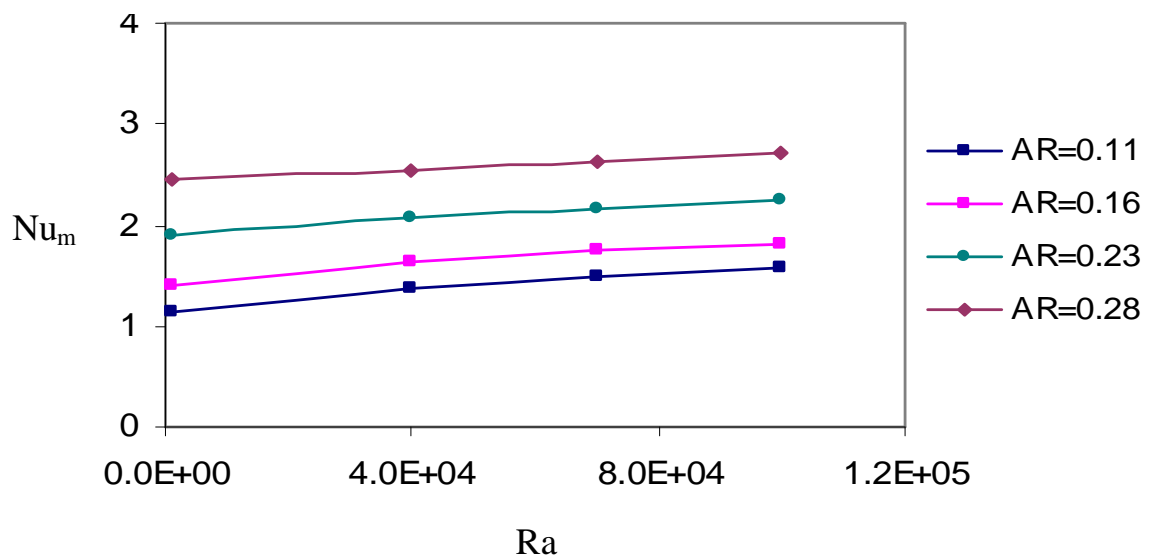


Figure (12). Variation of the mean nusselt number with Rayleigh number along the outer wall for different aspect ratios .

7. References

- [1] Nicolette V.F., Yang K.T., Lioid J.R., 1985, "Transient cooling by natural convection in a two dimensional square enclosure" Int.J.Heat Mass Transfer 28 1721-1732
- [2] Hyun J.M., Lee J.W., 1989, "Numerical solution of transient natural convection in a square cavity with different side wall" Int.J. Heat fluid 10 146-151.

- [3] Fusegi T., Hyun J.M., Kuwabare K., 1992, "Natural convection in a differentially heated square cavity with internal heat generation" *Numer-Heat Transfer* A21 215-229.
- [4] Ganzarolli M.M., Malanez L.F., 1995, "Natural convection in rectangular enclosure heated from below and symmetrically cooled from the sides" *Int.J. Heat Mass Transfer* 38 1063-1073.
- [5] Ekundayo C.O., Probert S.D. and Newborough M.,1998, "Heat transfer from a horizontal cylinder in a rectangular enclosure " *APPL.Energy* 61 57-78.
- [6] Suh C., Xue H., Zhu Y.D ,2001, " Numerical study of natural convection in eccentric annulus between a square outer cylinder and a circular inner cylinder using DQ method" *Int. J. Heat Mass Transfer* 44 3321-3331.
- [7] Shi X. J. Khodadi M., 2003, "Laminar natural convection heat transfer in a differentially heated square cavity due to thin film on the hot wall" *J. Heat Trans* 125 624-634.
- [8] Saeid N.H., Yaacob Y. 2006, "Natural convection in a square cavity with special side-wall temperature variation" *Numer-Heat Transfer. A49* (7) 683-697.
- [9] Wu W., Ching C.Y. , 2008, "The effect of partitions on the laminar convection in square cavity" *HT 2008-56193* in: 2008. ASME summer Heat Transfer conference. Jacksonville. Florida. USA 2008.
- [10] Mobedi M., 2008, "Conjugate natural in a square cavity with finite thickness horizontal walls" *Int. Commum. Heat Transfer* 35 503-513.
- [11] Basak T., Roy S. ,2008, "Role of Bajans heatlines in heat flow visualization and optimal thermal mixing for differentially heated square enclosure " *Int.J. Heat Mass Transfer* 51 3486-3503.
- [12] Wu W., Ching C.Y., 2009, "The effect of the top wall temperature on the laminar natural convection in rectangular cavities with different aspect ratios" *J. Heat Transfer* 131 1-11.
- [13] Gunor Backstrom , 2005, "Field of physics by finite element analysis using FlexPDE" GB publishing and Gunner Backstrom Malmo, Sweedn.
- [14] Roy S., Basak T., 2005, "Finite element analysis of natural convection flows in a square cavity with non uniformaly heated walls" *Int.J.Eng.Sci* 43 668-680.
- [15] Moukalled F., Acharya S. ,1996, "Natural convection in the annulus between concentric horizontal circular and square cylinders " *J. Thermophys. Heat Transfer* 10(30)

8. Nomenclature

AR	aspect ratio D/L
C_p	specific heat ($J/kg\ K$)
D	diameter of circle (m)
g	gravitational acceleration (m/s^2)
h	heat transfer coefficient ($W/m^2\ K$)
L	enclosure side length (m)
Nu	local Nusselt number
Nu_m	mean Nusselt number
p, P	dimensional and dimensionless pressure
Pr	Prandtl number
R	radius of circular rod (m)
RR	ratio of $L/2R$

Ra	Rayleigh number
s, S	dimensional and dimensionless local coordinates
T	temperature (K)
u, U	dimensional and dimensionless horizontal velocity component
v, V	dimensional and dimensionless vertical velocity component

Greek Symbols

Ψ	dimensionless stream function
θ	dimensionless temperature
α	thermal diffusivity (m^2/s)
β	thermal expansion coefficient ($1/K$)
ρ	fluid density (kg/m^3)
ν	kinematic viscosity (m^2/s)

Novel Space Time Spreading Scheme

Ahmed Abdel Hadi Fadhel

Electrical & Electronic Engineering Department

College of Engineering

University of Thi_Qar

Abstract

In this paper two spreading schemes and their detection methods were proposed and compared. The comparison depends on the performance of each scheme in Rayleigh flat fading channel. Space Time Spreading (STS) codes are used with Layered Space Time Codes (LST), with Vertical Bell Laboratories Space Time codes (V-BLAST) in particular. Also, Direct Sequence Code Division Multiple Access system (DS-CDMA) was used as a multi-user criterion. As a result of this spreading, a simple decoding algorithm was used. The simulation shows that STS-LST-DS-CDMA system with 3TX-3RX (3 transmitting antennas- 3 receiving antennas) using all paths between transmitter and receiver was better than LST-DS-CDMA system by about 4dB in SNR at BER of 10^{-4} . More detailed results are shown in Table 1. Also, the proposed scheme (may be partially) solves the problem of the code reuse.

Keywords: Space time spreading, Direct sequence code division multiple access, Layered space time coding, Bit error rate, Flat fading.

المستخلص

في هذا البحث تم اقتراح ومقارنة نموذجين لتوزيع المعلومات و طرق استرجاعها. المقارنة اعتمدت على الاداء في قناة Rayleigh flat fading. وتم استخدام شيفرة التوزيع الزماني والفضائي STS بالإضافة الى شيفرة التوزيع الفضائي والزماني الطبقي LST والتي تم اخذ احد انواعها وهي V-BLAST. كذلك تم استعمال نظام DS-CDMA لدمج عدة مستخدمين بالإضافة للشيفرات المذكورة. اوضحت المحاكاة ان نظام STS-LST-DS-CDMA الذي يستعمل ثلاثة هوائيات في الارسال و الاستلام مع استعمال كل المسارات بين المرسل و المستقبل كان افضل من نظام LST-DS-CDMA بمقدار 4dB عند نسبة خطأ 10^{-4} . نتائج مفصلة اكثر ممكن الحصول عليها من الجدول 1. كذلك فأن نظام STS-LST-DS-CDMA قد حل مشكلة اعادة استخدام الشيفرة ولو جزئيا.

1. Introduction

CDMA is a multiplexing technique where a number of users simultaneously and asynchronously access a channel by modulating and spread their information-bearing signals with preassigned signature sequences ^[1]. In the DS-CDMA technique, the serial to-parallel converted data stream is multiplied with the spreading sequence and then the chips belonging to the same symbol modulate the same carrier, the spreading is done in the time domain. The modulator for DS-CDMA is shown in Figure (1) ^[2].

Foschini ^[3] proposed a layered space-time (LST) architecture that can attain a tight lower bound on the MIMO channel capacity. The distinguishing feature of this architecture is that it allows processing of multidimensional signals in the space domain by 1-D processing steps, where 1-D refers to one dimension in space. The method relies on powerful signal processing techniques at the receiver and conventional 1-D channel codes ^[4]. There is a number of various LST architectures, depending on whether error control coding is used or not and on the way the modulated symbols are assigned to transmit antennas. An uncoded LST structure, known as Vertical Layered Space-Time (VLST) or Vertical Bell Laboratories Layered Space-Time (VBLAST) scheme ^[4,5], is illustrated in Figure (2).

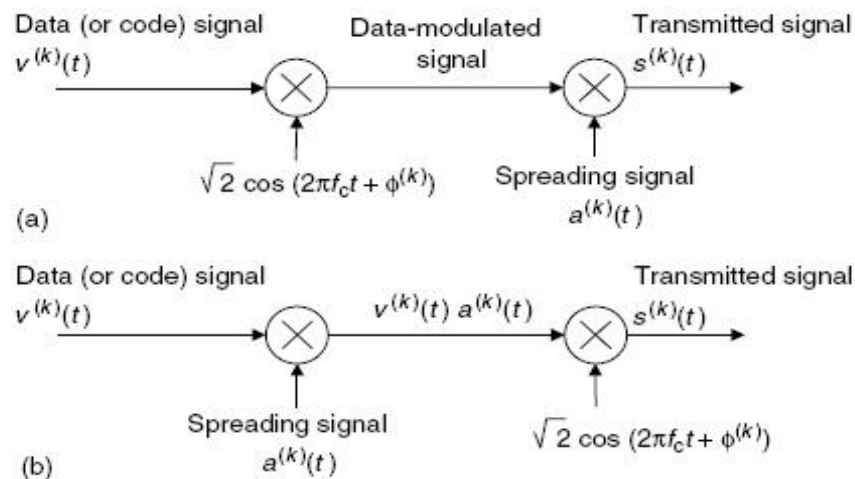


Figure (1). BPSK modulator for the k^{th} user in the DS-CDMA system.

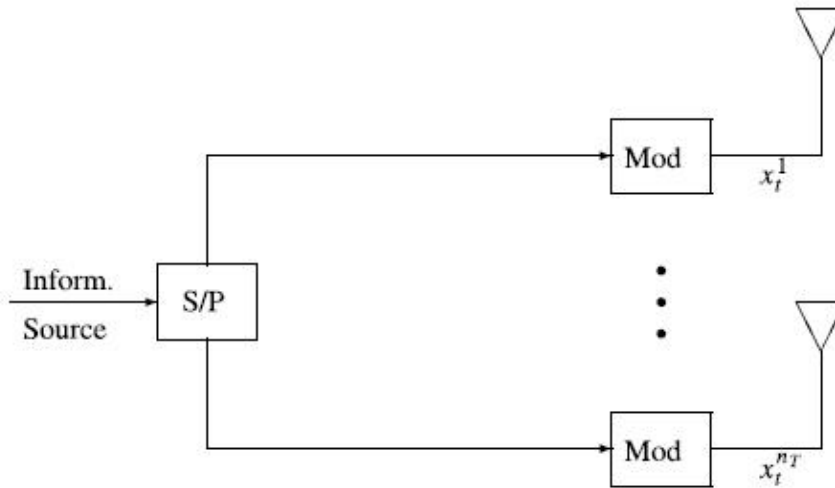


Figure (2). A VLST architecture.

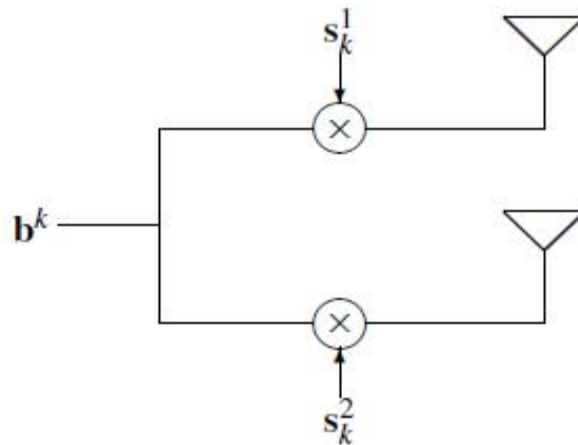


Figure (3). An open-loop transmit diversity.

The Open Loop Transmit Diversity proposed in [6] and the block diagram of an open-loop transmit diversity scheme is shown in Figure3. In this scheme, two different spreading sequences are assigned to each user. The same BPSK modulated symbols are transmitted from two transmit antennas [4]. There are other space time spreading schemes can be found in [4,6].

The proposed LST-STs-DS-CDMA system increases the SNR at each receiver antenna by using all the available paths between the transmitter and the receiver antennas not like the usual LST system which suppress the contribution of the other antennas [4]. It doesn't require any CSI information to be sent back to the transmitter as with MIMO beamforming system [7]. The multi-user detection also performed using the CSI at receiver only not like the Singular Value Decomposition (SVD) procedure proposed in [8].

The STS scheme proposed by [6] transmits the same signal over two different spreading codes over different antennas. This scheme uses M spreading sequences for M transmitting

antennas to each user^[4]. Since the spreading sequences are the resources in CDMA systems and the number of orthogonal codes is limited for a given spreading gain, this will reduce the number of users that can be simultaneously supported by the system^[4]. On the other hand LST-STS-DS-CDMA system uses one spreading sequence to each antenna to all users and another spreading sequence to each user. So, if we are using the system in^[6] and we have 3TX antennas and 3-users then we will need to each user 3 different spreading sequences. While in LST-STS-DS-CDMA system with the same inputs we'll need one spreading sequence to each user only at the DS-CDMA phase. And this spreading sequence can be reused as a spreading sequence at one of the transmitting antennas.

The LST-DS-CDMA system is equivalent to MIMO beam former^[7] from the number of paths between the transmitter and the receiver it used, but still having the advantage of not needing any CSI at the transmitter.

The drawback of this scheme is the need for perfect CSI information at the receiver, and care should be taken when implement it in frequency selective channel. That is because any shift in the spreading codes will lead to destroy the orthogonality between them, which leads to serious errors.

We didn't use 2TX-2RX system in this paper because it is believed that using Alamouti scheme would be more advantageous from complexity, and decoding aspects.

Another spreading scheme was proposed by^[9], where a new method is proposed for designing the spreading permutations based on space time block code matrices for MIMO-CDMA systems.

2. Proposed System

2.1. Layered Space Time Code-Space Time Spreading-Direct Sequence Code Division Multiple Access (LST-STS-DS-CDMA) System

The block diagram is shown in Figure 4. The data is first modulated by Binary Phase Shift Keying (BPSK) modulator, then encoded using DS-CDMA encoder. It should be noted that the length of the resulting codeword used here + the length of the code used in STS-encoder = the length of the codeword that would be generated if using DS-CDMA system alone. So, the bandwidth used by both systems is the same. This criterion is applied in all proposed systems below. The data then mapped to several transmitting antennas according to LST- coding criteria. The code used for layering is Vertical Bell Laboratories Space Time Codes (V-BLAST). The data is then transmitted through Rayleigh flat fading channel and Additive White Gaussian Noise (AWGN) was added at the receiver.

On the receiver side (which is the antenna terminal of user1 (U1)), the usual way is to use for example QR- factorization to solve the interference caused by multiple signal received at each receiving antenna, but, here we do not need it because of using the spreading sequence and our need to this interference as it will be shown later. The De-space time spreading is used to prepare the data to the combiner. The combiner function is to combine the signal from the multiple transmitting and multiple receiving antennas and add the original signal and its copies together to enhance the Signal to Noise Ratio (SNR). In other words, it is using all the available paths between the transmitter side and the receiver side. Till now all the users have the same data, the next step is the DS-CDMA decoder which translates this data into different users. Then the decoded message is demodulated using BPSK-demodulator. Because this system uses all paths between the transmitter and the receiver we'll call it all paths system.

The function of STS-LST encoder is shown in Figure (5). The function of the combiner is demonstrated in Figure (6).

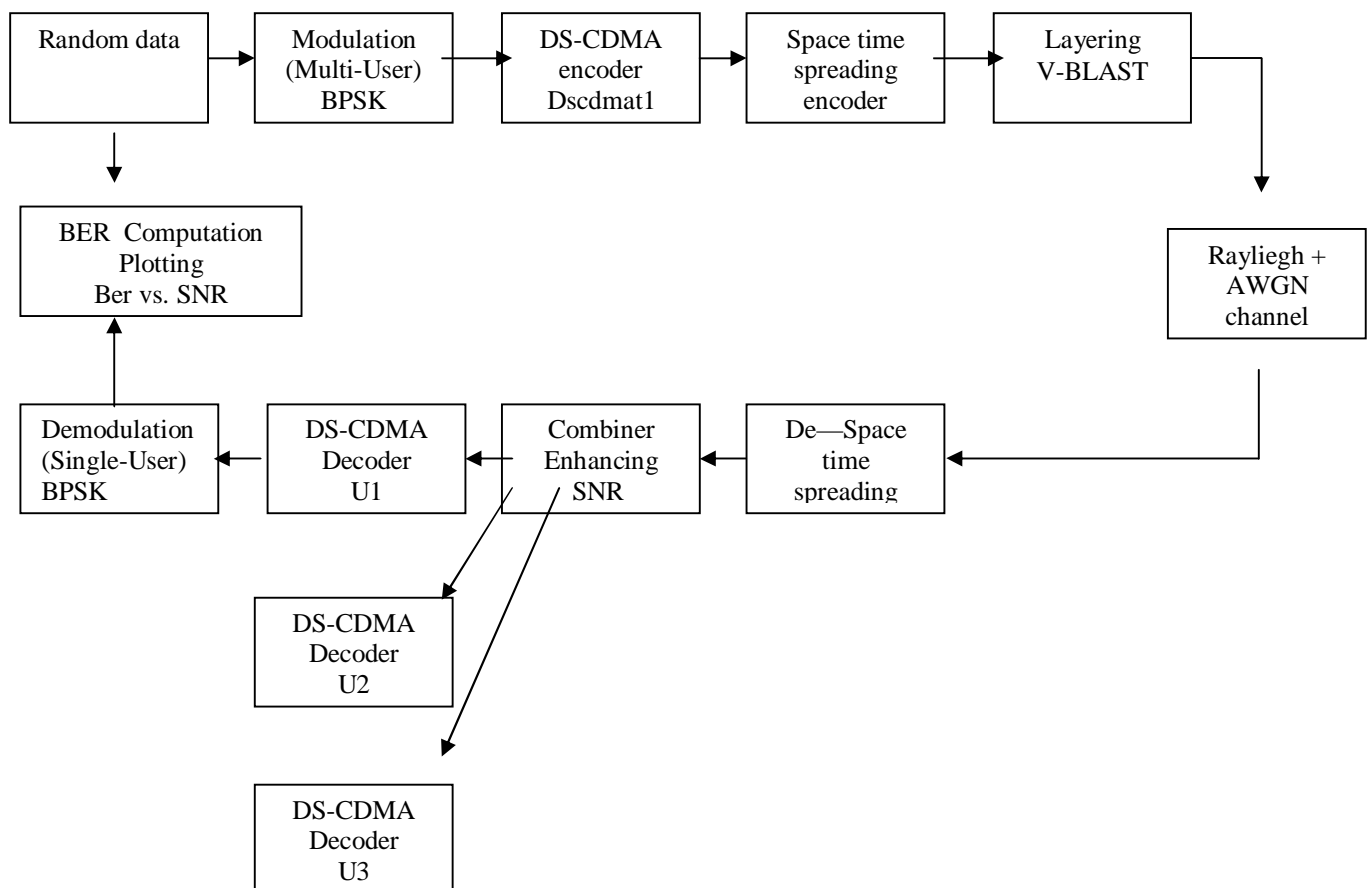


Figure (4). LST-STDS-CDMA System.

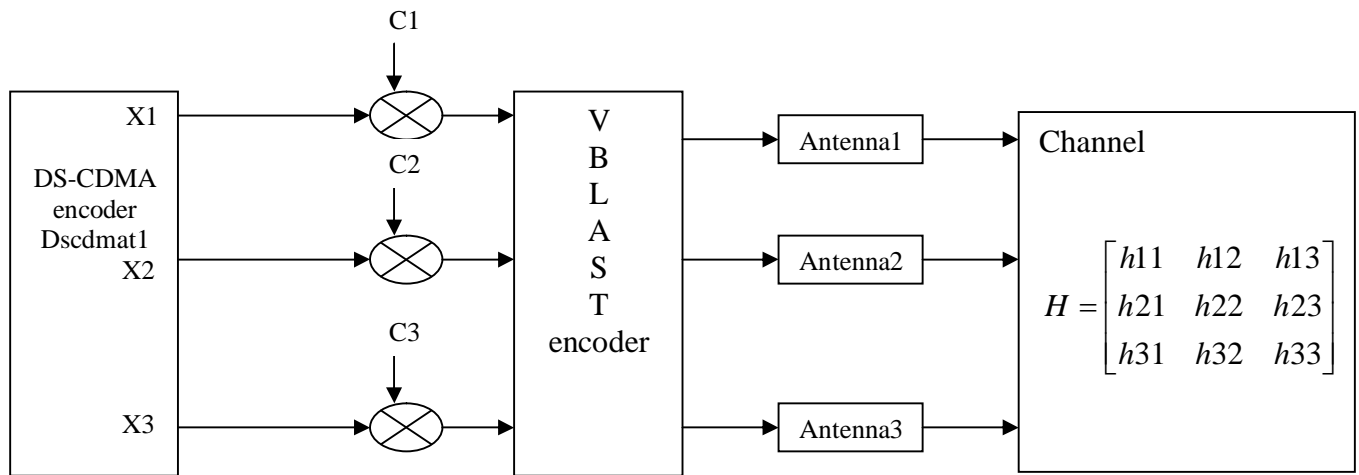


Figure (5). STS block + LST block.

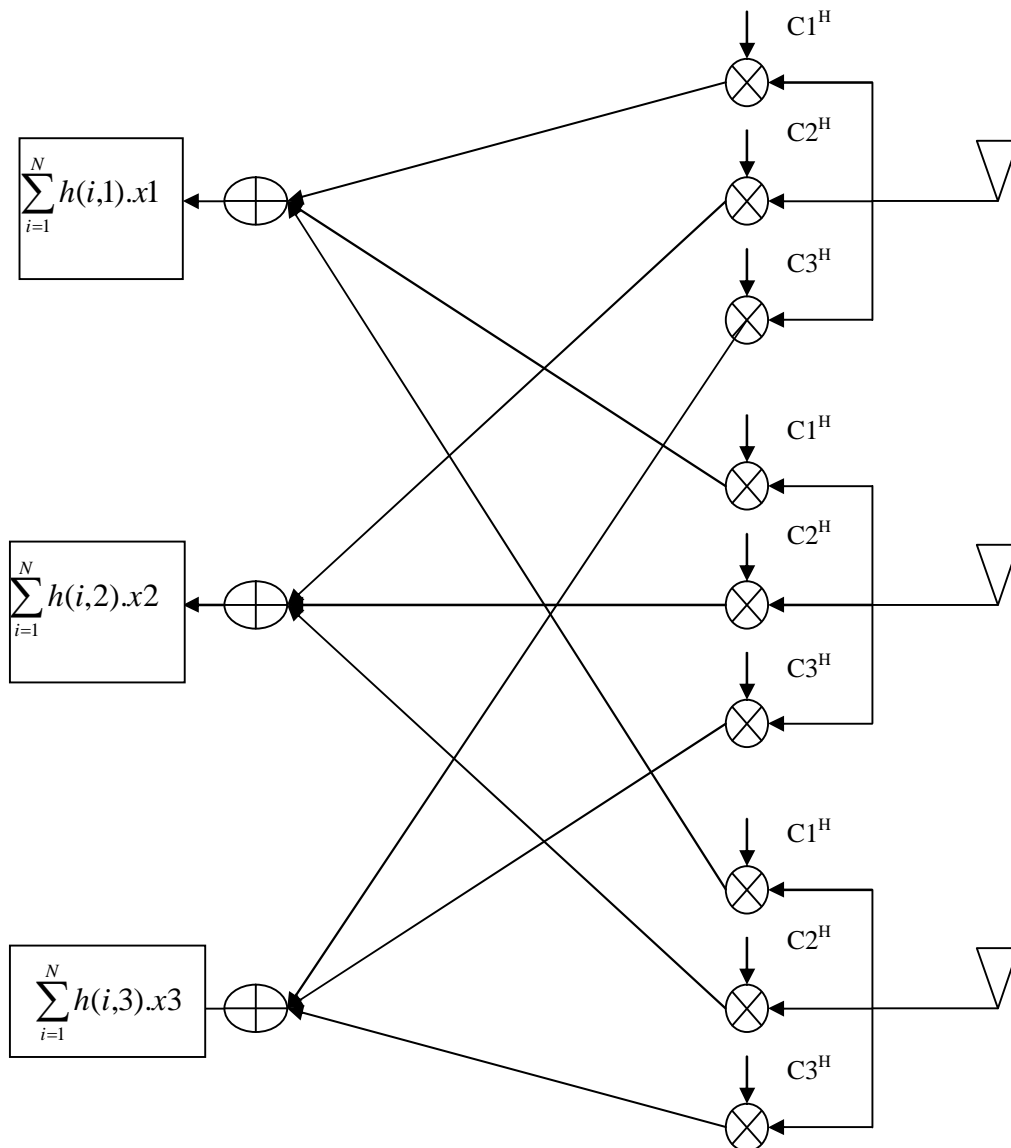


Figure (6). ST-dispreading and combiner block diagram.

The combiner in Figure (6) can be simplified to give a similar structure to SVD decoder with the advantage of not using the channel state information at the transmitter side. This is done by multiplying each received signal at each receiving antenna by its spreading code only, i.e.:

Let r_i be the received signal at antenna i . We'll take the case where there are 3TX-3RX antennas, and take the signal received by the first antenna as a demonstration example:

$$r_1 C_1^H = h_{11} x_1 C_1^H + h_{12} x_2 C_1^H + h_{13} x_3 C_1^H + n_1 C_1^H$$

$$C_i C_j^H = 0$$

$$C_i C_i^H = 1$$

$$r_1 C_1^H = h_{11} d_1 + n_1 C_1^H$$

Where n_1 is AWGN at receiving antenna 1.

Since the channel coefficients are assumed perfectly estimated, the last equation gives the data transmitted from the first antenna. This data still having the multi-user information and must be processed further by DS-SS-SSSS to give each user his information.

Because this system uses one channel coefficient we'll call it one-path system.

2.2. Layered space time code- direct sequence code division multiple access (LST-DS-SSSS) system

The block diagram of this system is similar to the block diagram in Figure (3) with removing the STS-blocks from the transmitter and receiver.

3. Simulation results

All simulations carried out in Rayleigh flat fading channel + AWGN. The channel coefficients are assumed perfectly estimated at the receiver. The MATLAB2009 is used as a programming package. The Spreading Factor (SF) (Processing Gain) is 16. The results are shown in Figure (7). The Table (1) shows the SNR values for all systems at BER of 10^{-4} .

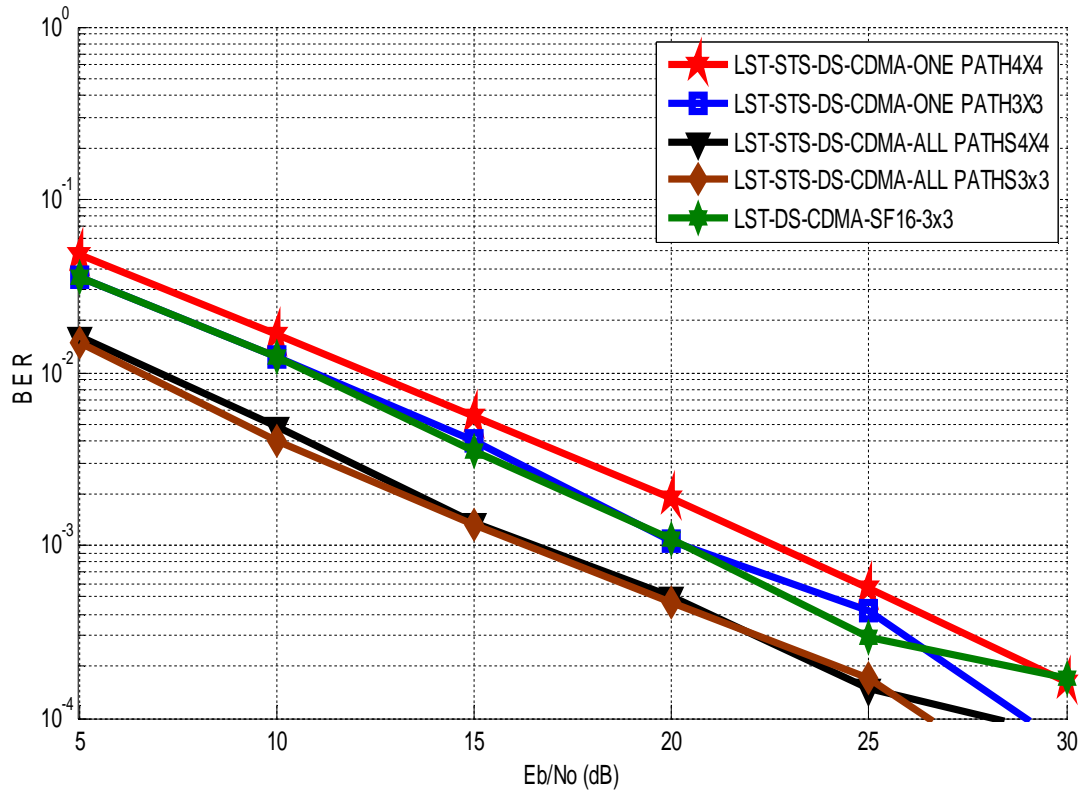


Figure (7). BER Vs. SNR in flat fading + WAGN channel.

Table (1). The SNR values for all systems at BER of 10^{-4} .

System used	SNR (E_b/N_0) dB
LST-STDS-CDMA-One Path-4X4	>30
LST-STDS-CDMA-One Path-3X3	29
LST-STDS-CDMA-All Paths-4X4	28.25
LST-STDS-CDMA-All Paths-3X3	26.5
LST -DS-CDMA-SF16-3X3	>30

4. Discussion

From Figure (7), it can be seen that the LST-STDS-CDMA with 3TX-3RX system is the best one. The LST-STDS-CDMA with 4TX-4RX achieves relatively the same as the LST-STDS-CDMA with 3TX-3RX system. Maybe this loss of performance is due to the amount added by using one more path (channel coefficient) and doesn't contribute too much to the received power.

The same thing can be said about the LST-DS-CDMA with 3TX-3RX system and LST-STS-DS-CDMA with 4TX-4RX-one path. Also, we should note that the amount of information conveyed by the 4TX-4RX systems is 25% higher than the 3TX-3RX systems because of the nature of signal spreading codes that requires more information processed.

The LST-DS-CDMA with 3TX-3RX system achieves a comparable performance to LST-STS-DS-CDMA with 3TX-3RX with one path system, with some advantage of the last one at higher SNRs. This is because the LST-STS-DS-CDMA with 3TX-3RX system uses two stages of spreading which leads to spread the noise then adding it and spreading it again. As a result, some noise components may cancel each other and at the same time the SNR increased.

5. References

- [1] Hara S., Prasad R., 1997, "Overview of Multicarrier CDMA", IEEE Communications Magazine, 35, (12), 126-133.
- [2] Zigangirov K. SH., 2004, "Theory of Code Division Multiple Access Communication", First Edition, USA, Wiley.IEEE Press.
- [3] Foschini G., 1996, "Layered space-time architecture for wireless communication in a fading environment when using multi-element antennas", Bell Labs Technical Journal, pp. 41–59.
- [4] Vucetic B., Yuan J., 2003, "Space-Time Coding", First Edition, USA, John Wiley & Sons Ltd.
- [5] Golden G. D., Foschini G. J., Valenzuela R. A. and Wolniansky P. W., 1999, "Detection algorithm and initial laboratory results using the V-BLAST space-time communication architecture", Electronics Letters, vol. 35, no. 1, Jan. 7, pp. 14–15.
- [6] Hochwald B., Marzetta T. L. and Papadias C. B., 2001, "A transmitter diversity scheme for wideband CDMA systems based on space-time spreading", IEEE Journal on Selected Areas in Communication., vol. 19, no. 1, pp. 48–60.
- [7] Goldsmith A., 2005, "Wireless Communications", First Edition, USA, Cambridge University Press.
- [8] Kim J., Cioffi J. M., 2000, "Spatial Multiuser Access with Antenna Diversity using Singular Value Decomposition", IEEE International Conference on Communication, vol. 3, pp. 1253-1257.
- [9] Shi M., D'Amours C., and Yongacoglu A., 2010, "Design of Spreading Permutations for MIMO-CDMA Based on Space-Time Block Codes", IEEE Communications letters, Vol. 14, no. 1.

Evaluation the Efficiency of Installing Stone Columns in Ground Improvement of Al-Nassiriya City Soil

Esraa Abdulaemma Mandhour

Nesreen Kurdy Thabbah Al-Obaidy

College of Science
University of Thi_Qar

Civil Engineering Dept.
College of Engineering
University of Thi_Qar

Abstract

This paper investigates the performance of stone columns in soft soil of Al-Nassiriya city (one of Iraqi cities in the south). A geotechnical study of physical and mechanical properties of the soil has been carried out for a selected areas from Al-Nassiriya city. A finite difference Matlab program has been employed in simulation of installing stone columns in the aforementioned soil. Results of the study illustrate using stone columns reduces the settlement of the soil for different values of the modular ratio and replacement ratio, thus the W_{max} maximum settlement ratio changes from 30% to 16% of the modular ratios (E_c/E_s)=10 and 50 respectively. The effect of spacing and column width is taken into consideration.

All results are reasonable and harmonic with most last studies.

Keywords : Geotechnical ,stone columns , finite difference .

تقييم كفاءة استخدام الاعمدة الحجرية في تحسين تربة مدينة الناصرية

المستخلص

ان هذا البحث يدرس كفاءة استخدام طريقة تسليح تربة مدينة الناصرية الضعيفة بتقنية الركائز الحجرية. وقد تم عمل جميع فحوصات التربة المختبرية لنماذج منتقاة من احد المواقع في مدينة الناصرية وذلك لمعرفة الخواص الفيزيائية والميكانيكية للتربة .

و قدمت الباحثتان في هذا البحث محاكاة نموذج ميكانيكي لتربة مدينة الناصرية الضعيفة مسلحة بعمود حجري موضوع فوقها طبقة حبيبية باستخدام برنامج الماتلاب وحسب طريقة الفروق المحددة وبالاستفادة من نتائج الفحوصات المختبرية لتمثل بيانات ادخال المسألة.

لقد اثبتت النتائج فعالية تسليح تربة مدينة الناصرية بأعمدة حجرية ، اذ أعطى هذا النوع من التسليح تقليل من مقدار الهبوط الكلي وبالتالي زيادة في قيمة قابلية التحمل لتربة مدينة الناصرية .ولقد اعطت النتائج في هذه الدراسة توافقا مع دراسات سابقة كثيرة.

1. Introduction

Al-Nassiriyah city, the centre (capital) of Thi-Qar governorate is situated in the south of Iraq at about 225 miles (370 km) southeast of Baghdad. Recently many engineering projects have been performed as a result to rebuilding movement in Thi-Qar province. The basic construction problem is related to the foundation because the soil is soft and the underground water exists at shallow depth of the soil.

Based on our site observations, stone columns are adopted to increase load carrying capacity and reduce the total settlement. In addition to the advantage of getting a drainage path for solving a problem of high underground water.

The main objectives for using stone column in soil reinforcement are, to increase the bearing capacity, reduce settlement, improve slope stability and the resistance to liquefaction (Greenwood, 1970; Baumann & Bauer, 1974; Hughes, J. M. O. & Withers, 1974; Priebe, 1976; Madhav & Vitkar, 1978; Goughnour & Bayuk, 1979; Balaam & Booker, 1981; Schweiger & Pande, 1986; and Canetta, & Nova, 1989). In 2010 Deb studied the advantage of providing a drainage path (as stone column behaves similar to sand column). Moreover soil reinforcement by stone column can be considered as a very economic solution for soil improvement (Al-Obaidy 2000).

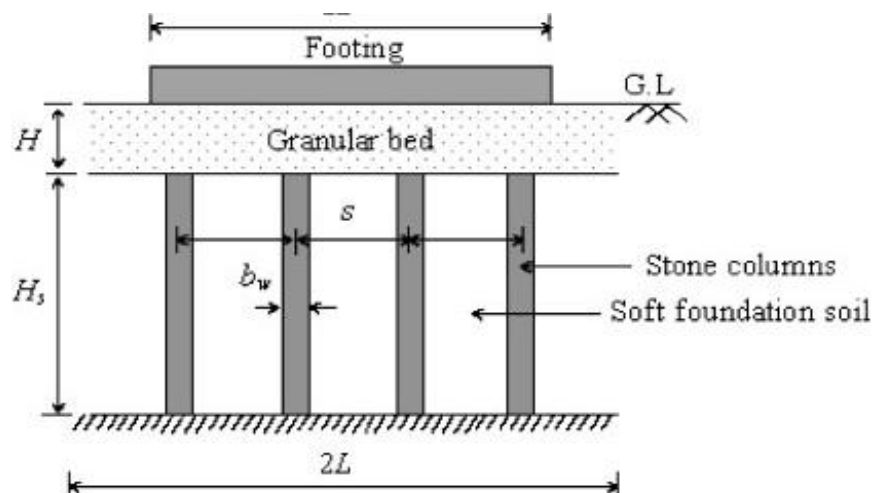
A number of publications have been written on the development of theoretical solutions for estimating settlement and bearing capacity of soft soils reinforced by stone columns. Many researchers simulated their studies of stone columns by finite element method, see : Acharya, et al, 2005; Al-Obaidy, 2005; Elshazly et al 2007 & 2008; Frikha et al 2008; Sadek and Shahrour 2008; and Hassen et al, 2010. Whereas others introduced their numerical model using finite difference method such as: Buggy et al, 1994; Taberlet et al, 2006; Deb et al, 2007; El Shamy, 2007; Han et al, 2007; Murali, et al 2007; and Deb, 2010.

A granular layer of sand or gravel is usually placed over top of the stone columns (Mitchell, 1981) as shown in Figure (1). This granular layer or sand bed acts as drainage layer and also distributes the stresses coming from the embankments.. The embankment has been modeled by Pasternak shear layer with variable thickness as proposed by Sharma in 1989. The granular layer and the soft soil have been idealized by the Pasternak shear layer and spring-dashpot system, respectively as described by Shukla and Chandra, 1994 :[see Figure (2)].

In the present study, the mechanical model shown in Figure (2) have been adopted and a numerical study is conducted to investigate the efficiency of installing stone columns in Al-

Nasiriyah city soil in increasing load carrying capacity and reducing the amount of settlement of the soil.

In the present paper, there are two steps, The first one is performing laboratory tests to get the input data which represent the case of Al-Nasiriyah city soil and then using these data in the second step. The second one is programming the case study using Matlab program to simulate the case of Al-Nasiriyah soil improvement by reinforcing it by stone columns have different modular ratio and replacement area.



Figure(1). A granular fill-stone column-reinforced soft soil system.

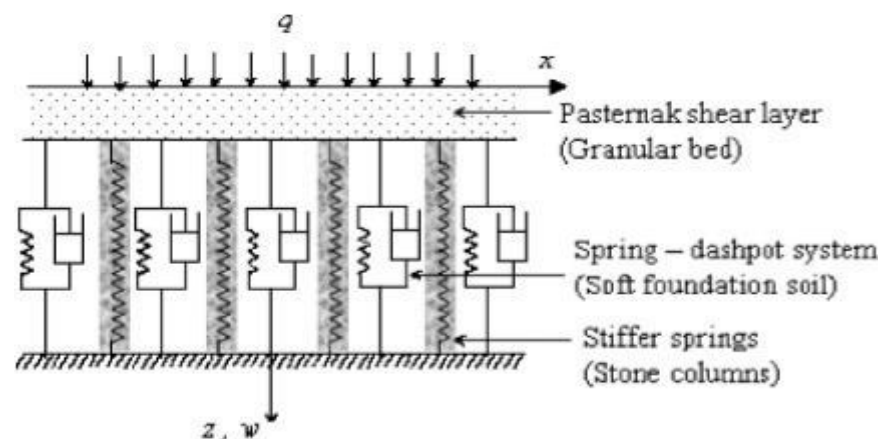


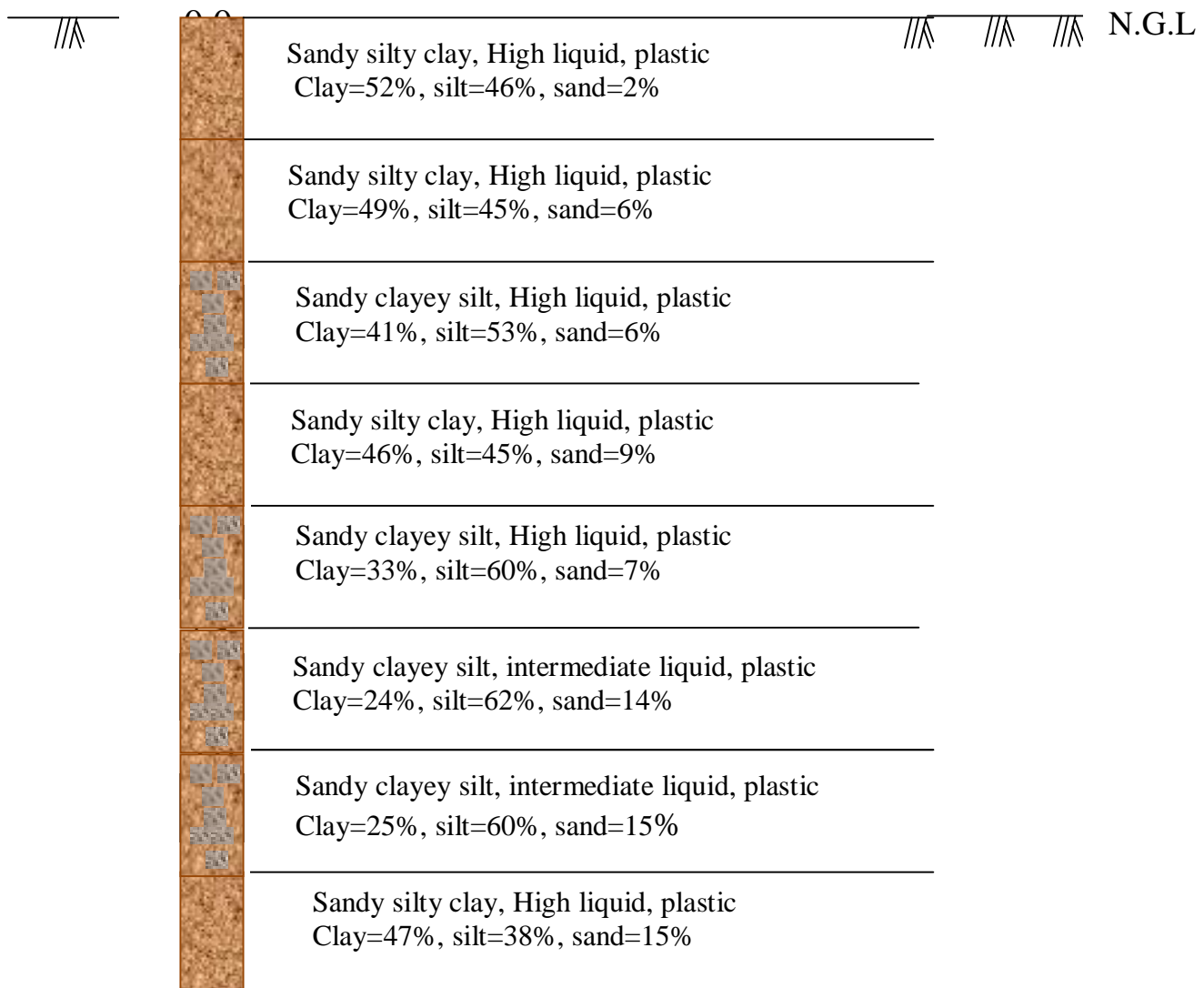
Figure (2). The mechanical Model (Pasternak shear layer-stiffer spring-spring & dashpot).

2. Soil properties from experiments

Soil specimen has been taken from bore holes in Al -Shumukh area in Al-Nasiriyah city and number of soil samples have been tested. The laboratory tests are carried out in the National Centre For Construction Laboratories (NCCL) at Thi-Qar governorate & the soil mechanics laboratory at Civil Engineering Department, College of Engineering, University of

Baghdad. The geotechnical properties for soil are determined according to the American society for testing and material (1984) and standard procedures adopted by the British standard (BS1377; 1975).

Figure (3) shows the soil profile for site study, while Table(1) represents a complete summary of all laboratory test results which belong to Al- Shumukh area soil which has been simulated to be reinforced with stone column.



Figure(3). Al -Shumukh area soil profile.

Table (1). The physical and mechanical properties of the soil of Al -Shumukh site in Al-Nasiriyah city.

Depth of sample (m)	Index tests			Mc	Ic	Specific gravity	Total density g/cm ³	Swelling potential	Mechanical Properties	
	LL	PL	PI						C kg/cm ²	ϕ^0
0.0 - 0.5	62	32	30	36	0.866	2.7		9.618		
0.5 - 1.0	57	28	29	32	0.862	2.7	1.82	8.485	0.5	11
1.0 - 1.5	55	25	30	37	0.6	2.7		8.14		
1.5 - 2.0	57	29	28	28	1.035	2.68		7.423		
2.0 - 2.5	58	30	28	30	1	2.7	1.79	6.025	0.3	10
2.5 - 3.0	43	26	17	27	0.941	2.68	1.9	1.532		
3.0 - 3.5	42	25	17	30	0.705	2.7	1.85	1.559		
3.5 - 4.0	50	31	19	24	1.368	2.7	1.9	2.935		

3.Theoretical analysis

The uniform load of intensity (q) which is applied on the foundation of $2B$ width at time ($t>0$) is expressed by Deb et al in 2007 for the same mechanical visco - elastic model shown in Figure (2) as follow:

$$q = q_s - GH \frac{\partial^2 w}{\partial x^2} \quad (1)$$

Where:

q_s : vertical stress acting on the saturated soft foundation soil

H : thickness of the granular layer placed over the soft soil

$w(x,t)$: vertical displacement

G : shear modulus of the granular layer which can be expressed based on hyperbolic shear stress- shear strain response proposed by Gosh and Madhav (1994) as:

$$G = \frac{G_0}{\left[1 + \frac{G_0 / \partial w / \partial x}{\tau_u} \right]^2}$$

Where G_0 and τ_u : initial modulus of the shear layer and ultimate shear resistance of the granular layer respectively.

The vertical stress q_s at time ($t>0$) considering the hyperboilic non-linear stress-displacement relationship and the consolidation effect of the soft soil can be expressed as Deb et al in 2007 as the following equation:

$$q_s = \frac{k_{s0}w}{U[1 + k_{s0}(w/q_u)]} \quad (2)$$

Where:

k_{s0} : initial modulus of a subgrade reaction of the saturated soft soil

q_u : ultimate bearing capacity of the saturated soft soil

U : average degree of consolidation at any time (t)

By substitution eq. 2 in eq.1 that yields:

$$q = \frac{k_{s0}w}{U[1 + k_{s0}(w/q_u)]} - GH \frac{\partial^2 w}{\partial x^2} \quad (3)$$

Since the vertical stress acting on the stone column is $q_c = k_{c0}w$

(where: k_{c0} : modulus of the subgrade reaction of the stone column)

Eq.3 can be written in the following form to govern the differential equation within the stone column region:

$$q = k_{c0}w - GH \frac{\partial^2 w}{\partial x^2} \quad (4)$$

Using the non-dimensional parameters as:

$$X=x/B, W=w/B, G^*=GH/k_{s0}B^2, G_0^*=G_0H/k_{s0}B^2, q^*=q/k_{s0}B, q_u^*=q_u/k_{s0}B, \tau_u^*=\tau_uH/k_{s0}B^2, \alpha=k_{c0}/k_{s0}, q_s^*=q_s/k_{s0}B, q_c^*=q_c/k_{s0}B, q_c^*=\alpha W$$

The governing differential equation at time $t>0$ can be expressed in a non-dimensional form as:

$$q^* = CW - G^* \frac{\partial^2 w}{\partial x^2} \quad (5)$$

Where:

$$C = \frac{1}{U[1 + (W/q_u^*)]} \quad \text{within the soft foundation}$$

$$= \alpha \quad \text{within the stone column region}$$

The modulus of the subgrade reaction of the soft soil (spring stiffness) can be expressed in terms of the modulus of elasticity and Poisson ratio ,see Bowels in 1988:

$$k_{s0} = \frac{E_s}{H_s(1 + \mu_s)(1 - 2\mu_s)} \quad (6)$$

Where :

H_s : thickness of the soft soil

E_s : modulus of elasticity

μ_s : Poisson's ratio

The modulus of the subgrade reaction of the stone column using stone column length equal to the length of soft soil according to the above equation will be:

$$k_{c0} = \frac{E_c}{H_c(1+\mu_c)(1-2\mu_c)} \quad (7)$$

Where :

H_c : length of stone pile

E_c : modulus of elasticity of the stone column

μ_c : Poisson's ratio of the stone pile

Thus the subgrade modulus or spring constant ratio (α) can be calculated as:

$$\alpha = \frac{(1+\mu_s)(1-2\mu_s)E_c}{(1+\mu_c)(1-2\mu_c)E_s} \quad (8)$$

The degree of consolidation of the stone column-reinforced soft soil at any time has been calculated as mentioned by Deb et al in 2007 , in which the width of the plain strain unit cell is taken to be equal to the diameter of the unit cell in the axi-symmetric condition , they introduce An approximate solution if U is greater than 30% to be expressed as:

$$U = 1 - \frac{8}{\pi^2} \exp^{-[8/F(N_{PL})]T'_r - [\pi^2/4]T'_v} \quad (9)$$

Where

$T'_r = c'_r t / 4B_e^2$: a modified time factor in the radial flow, B_e is half plain-strain unit cell width

$T'_v = c'_v t / H_s^2$: a modified time factor in the vertical flow

$F(N_{PL}) = 2/3$, N_{pl} is width ratio ($=2B_e/b_w$), b_w is width of the stone and C_v are modified coefficient of consolidation in radial and vertical directions respectively

$$c_r = c_r \left(1 + \beta \frac{1}{N_{pl}^2 - 1} \right) \text{ and } c_v = c_v \left(1 + \beta \frac{1}{N_{pl}^2 - 1} \right)$$

c'_r and c'_v are modified coefficient of consolidation in radial and vertical directions

β : is the stress concentration ratio as the consolidation complete

$$= \xi \frac{E_c}{E_s} \text{ where } \xi \text{ is the Poisson ratio factor which equal to: } \frac{(1+\mu_s)(1-2\mu_s)(1-\mu_c)}{(1+\mu_c)(1-2\mu_c)(1-\mu_s)}$$

4. Presentation of the implemented program

The application of the theory developed above is obtained with the help of the MATLAB Virgin R2008b , its software offering various functions and facilities to compile and to visualize complex mathematical operations. The implemented program is subdivided into different logic subprograms accomplishing specific tasks from data input to output visualisation .

The governing differential equation (eq.5 in the previous section)has been programmed using finite difference method by dividing the length L/B into n number of elements with $(n+1)$ number of node points ($i = 1, 2, 3, 4$ to n);thus, the mesh size (ΔX) can be expressed as, ΔX . the governing differential equation in a finite difference form, for an interior node (i, j) (where i and j are the indices for space and time, respectively) as expressed below:

$$q_i^* = C_{i,j} W_{i,j} - G_t \left[\frac{W_{i-1,j} - 2W_{i,j} + W_{i+1,j}}{(\Delta X)^2} \right] \quad (10)$$

where

$$C_{i,j} = \frac{1}{U_j \left[1 + \left(W_{i,j} / q_u^* \right) \right]} \quad \text{within the soft foundation soil}$$

$$= \alpha \quad \text{within the stone column region}$$

One half of the system is depended as the problem is symmetric,. Thus, at the centre of the loaded region $X = 0$ or $x = 0$, due to symmetry, the slope $\partial W / \partial X$ will be zero. The width of the granular fill considered in the analysis is sufficient enough so that at the edge [at $X = L/B$ (or $x = L$)] the slope $\partial W / \partial X$ of the settlement-distance profile will also be zero.

The continuity at the edge of the stone columns is automatically satisfied. The loading conditions considered are given as:

$$q_i^*(X) = q^* \quad \text{for } |X| \leq 1.0$$

$$= 0 \quad \text{for } |X| > 1.0 \quad (11)$$

5. Results and discussion

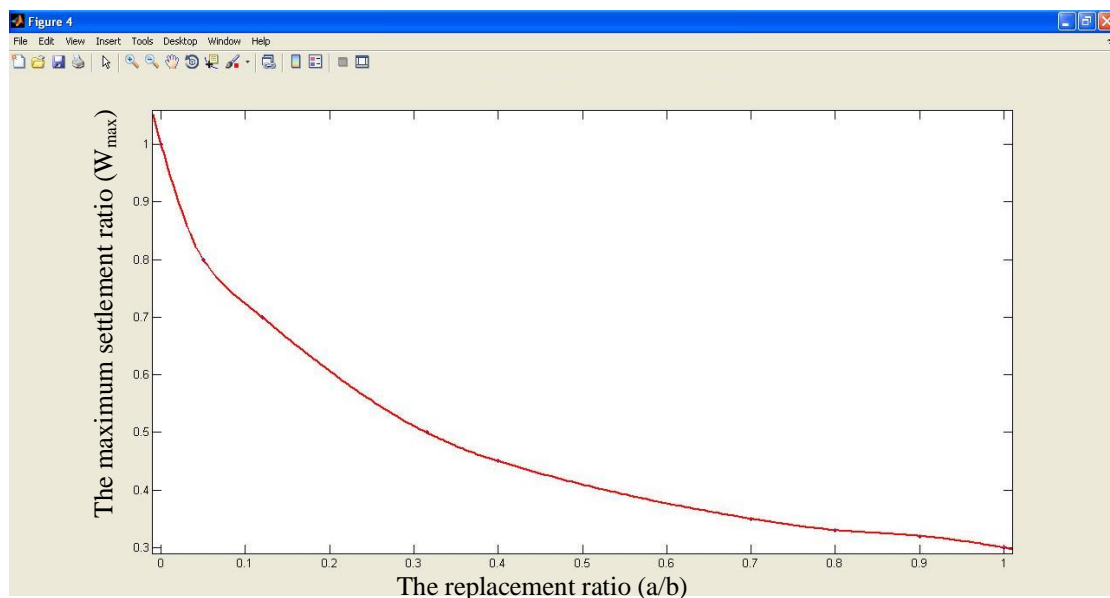
Figure (4) illustrates the variations of maximum settlement ratio of the improved ground to that of an unimproved ground with replacement ratio a/b (where $a = bw/2$ and $b = s/2$, where s is the center to center distance between the stone columns) .It can be observed from Figure (4) that, when a/b is zero (no stone column) no reduction in the maximum settlement has been observed, but as the value of a/b increases settlement decreases and when a/b is 1, in that case,

the soft foundation soil is completely replaced by stone columns, and reduction of the settlement is maximum at that point. As the stiffness of the stone columns is increased compared with the soft foundation soil, settlement is reduced further. This is because of the fact that as stiffness of the stone columns is increased more stress is transferred onto the stone column from the soft soil due to their stiffness difference which causes more settlement reduction. However, after $a/b=0.5$, no significant change in the amount of the maximum settlement ratio.

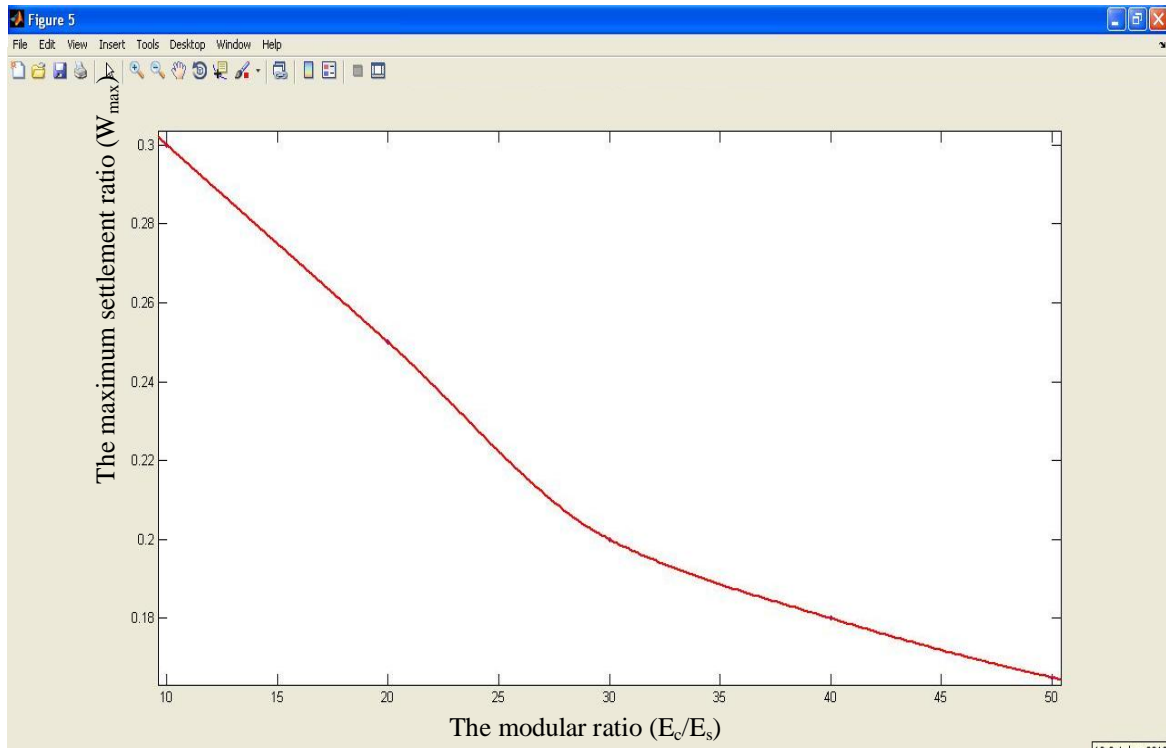
Figure (5) shows the effect of the modular ratio E_c/E_s on the amount of the maximum settlement. Obviously, it can be seen that as the modular ratio E_c/E_s increases as the maximum settlement decreases, thus the value of the maximum settlement ratio ranges between 0.3 and 0.15 for modular ratios E_c/E_s from 10 to 50. That may be explaining how the stiffer stone column carries more load which subjected on the composed cell of stone column and its surrounding area.

The relationship between maximum settlement and the ratio of spacing and the width of the stone column s/b_w for different values of the modular ratio is shown in Figure (6). There is a remarkable change in the value of the maximum settlement with respect to the ratio of s/b_w .

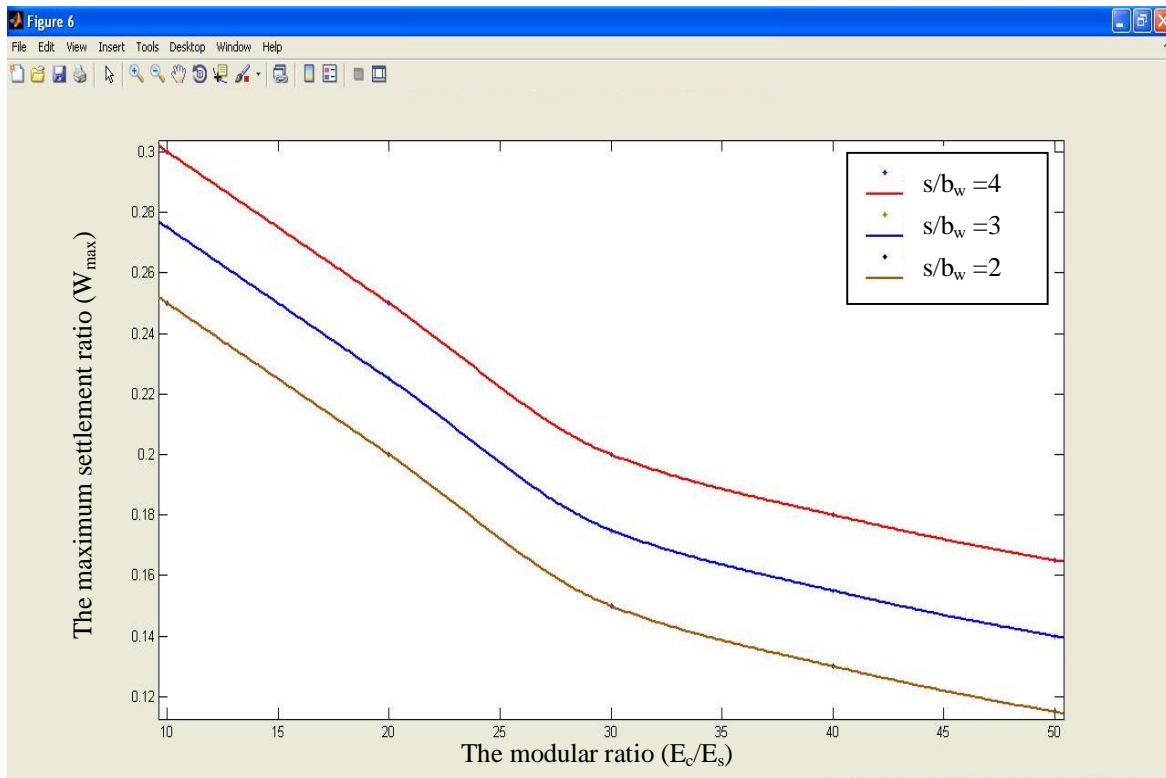
The results of this study are harmonic with last the studies results such as Balaam and booker 1981; Alamgir, et al 1996 and Al-Obaidy, 2005.



Figure(4). The maximum settlement ratio versus the replacement ratio.



Figure(5). The maximum settlement ratio versus the modular ratio (E_c/E_s).



Figure(6). The maximum settlement ratio versus the modular ratio for different values of s/b_w .

6. Conclusion

From the above discussions it can be said that the installation of stone column in Al-Nasiriyah soil is quite useful to reduce the amount of settlement and subsequently increasing the amount of the bearing capacity, thus the maximum settlement ratio changes from 30% to 16% of the modular ratios (E_c/E_s) =10 and 50 respectively. In addition there is an advantage of getting a drainage path for the stone column acts as sand drain for solving a problem of high underground water in Al-Nasiriyah soil. Moreover the material of stone column is very cheap if compare with others material, so it can be considered an economic solution for ground improvement.

7. References

- [1] Acharya; Biswajit; Dasgupta; & Shambhu P. , 2005, "Consolidation of stone-columned soils", Electronic Journal of Geotechnical Engineering, V10 E.
- [2] Alamgir, M.; Miura, N., Poorooshab, H. B., & Madhav, M.R. , 1996, "Deformation analysis of soft ground reinforced by columnar Inclusions", Computers and Geotechnics, 18(4): pp.267–290.
- [3] Al-Obaidy, N. K. , 2000, "Full scale tests on stone piles", Baghdad University .Master Thesis,.
- [4] Al-Obaidy, N. K. , 2005, "Evaluate the effect of relative stiffness between stone pile & reinforced soil (E_p/E_s) on degree of improvement using finite element method", Al-Fateh Magazine, Scientific Magazine, DIALA University, No.21, pp. 93-106.
- [5] ASTM, 1984, "Manual book of ASTM standard by the American society for testing and material", Vol. 04 – 08.
- [6] Balaam, N.P. & Booker J. R., 1981, "Analysis of rigid raft supported by granular piles", International Journal for Numerical and Analytical Methods in Geomechanics, 5: pp.379–403.
- [7] Baumann, V. & Bauer, G. E. A., 1974, "The performance of foundation on various soils stabilized by vibrocompaction method", Canadian Geotechnique . J.11 5099530
- [8] British standards institution, 1975, "Methods of testing soils for civil engineering purposes", (B. S. 1377).
- [9] Buggy, Fintan J. , Martinez, Ramon E. , Hussin, James D. , & Deschamps, Richard J. , 1994, "Performance of oil storage tanks on vibroflotation improved hydraulic fill in the Port of Tampa, Florida", Geotechnical Special Publication, V. 1, N. 40, pp. 548-560.

- [10] Canetta, G. & Nova, R., A. , 1989, "Numerical method for the analysis of ground improved by columnar inclusions", *Computers Geotech.* 7, pp. 99 - 114.
- [11] Deb, Kousik; Sivakugan, N.; Chandra, Sarvesh, & Basudhar, P.K. , 2007, "Numerical analysis of multi layer geosynthetic-reinforced granular bed over soft fill", *Geotechnical and Geological Engineering*, V 25, N 6, pp. 639-646.
- [12] Deb, Kousik, 2010, "A mathematical model to study the soil arching effect in stone column-supported embankment resting on soft foundation soil", *Applied Mathematical Modelling*, V 34, N 12, pp. 3871-3883.
- [13] El Shamy and Zeghal, M. , 2007, "A micro-mechanical study of soil-pile interaction during dynamic excitations", *Geotechnical Special Publication*, N 173, p 29, *Proceedings of Sessions of Geo-Denver 2007 Congress: Advances in Measurement and Modeling of Soil Behavior*.
- [14] Elshazly, H.; Hafez, D.; & Mossaad, M. , 2007, "Settlement of circular foundations on stone-column-reinforced grounds", *Ground Improvement*, V 11, N 3, pp. 163-170.
- [15] Elshazly, Hesham; Elkasabgy, Mohamed; & Elleboudy, Azza, 2008, "Effect of inter-column spacing on soil stresses due to vibro - installed stone columns: Interesting findings", *Geotechnical and Geological Engineering*, V. 26, N. 2, pp. 225-236.
- [16] Frikha, Wissem¹; Bouassida, Mounir¹; & Canou, Jean, 2008, "Calibration of an elastoplastic model for the prediction of stone column ultimate bearing capacity", *Geotechnical Special Publication*, N 178, pp. 604-611, *Proceedings of session of Geo. Congress 2008*.
- [17] Ghosh, C., Madhav, M. R. , 1994, "Settlement response of a reinforced shallow earth bed", *Geotextile and Geomembranes*, 13(9):pp. 643-656.
- [18] Goughnour, R. R. & Bayuk, A. A. , 1979, "Field study of long-term settlement of loads supported by stone columns in soft ground", *Proc. Int. Conf Soil Reinfor: Reinfor. Earth & Other Techniques*, Paris, Vol. 1, pp. 279-286.
- [19] Greenwood, D. A. , 1970, "Mechanical improvement of soils below ground surface", *Proc. Ground Engineering Conf. Institution of Civil Engineers*, pp. 9-20.
- [20] Han, Jie; Oztoprak, Sadik; Parsons, Robert L.; & Huang, Jie, 2007, "Numerical analysis of foundation columns to support widening of embankments", *Computers and Geotechnics*, V 34, N 6, pp. 435-448.
- [21] Hassen, Ghazi; Buhan, Patrick de; & Abdelkrim, Malek, 2010, "Finite element implementation of a homogenized constitutive law for stone column-reinforced

- foundation soils, with application to the design of structures”, *Computers and Geotechnics*, V 37, N 1-2, pp. 40-49.
- [22] Hughes, J. M. O. & Withers, N. J. , 1974, “Reinforcing soft cohesive soil with stone Columns”, *Ground Eng.* 7, pp. 42-49.
- [23] Madhav, M. R. and Vitkar P. P. , 1978, “Strip footing on weak clay stabilized with granular trench or piles”, *Canadian Geotechnical Journal*; 15: pp. 605–609.
- [24] Mitchell, J.K. , 1981, “Soil improvement – state of the art report”, in: *Proceedings of 10th International Conference on Soil Mechanics and Foundation Engineering*, Balkema, Rotterdam, The Netherlands, Vol. 4, pp. 509–565.
- [25] Murali Krishna, A.; Madhav, M.R.; & Madhavi Latha, G. , 2007, “Densification effect of granular piles on settlement response of treated ground”, *Ground Improvement*, V 11, N 3, pp. 127-136.
- [26] Priebe, H. , 1976, “Estimating settlements in a gravel column consolidated soil”, *Die Bautechnik* 53, pp. 160-162.
- [27] Sadek, M.& Shahrour, I. , 2008, “Eccentricity effect on a footing supported by a stone column”, *Proceedings of the Institution of Civil Engineers: Ground Improvement*, V 161, N 2, pp. 65-70.
- [28] Schweiger, H. F & Pande, G. N. , 1986, “Numerical analysis of stone column supported foundation”, *Computers Geotech.* 2, pp. 347-372.
- [29] Shukla, S.K. and Chandra, S. , 1994, “A generalized mechanical model for geosynthetic-reinforced foundation soil”, *Geotext. Geomembr.* 13 (3), pp. 813–825.
- [30] Taberlet, Nicolas; Richard, Patrick; & John Hinch, E., 2006, “S shape of a granular pile in a rotating drum”, *Physical Review E - Statistical, Nonlinear, and Soft Matter Physics*, V 73, N 5.

Modeling of the Dissolved Oxygen Profile in Marsh Water by Numerical Solution of ADE Using Finite Difference Method

Mohammed Dekheel Selman

Marshes Research Centre

Thi Qar University

Abstract

To evaluate the environmental impact of pollution, mathematical models play a major role in predicting the pollution level in the regions under consideration. Computer models are becoming increasingly important tools in every environmental management aspects. A general one dimensional water quality model (Advection-diffusion Equation ADE) has been developed the dissolved oxygen in Abu-Zirig marsh water. The general one-dimensional model equation was solved using the numerical solution by finite difference discretization and procedure was prepared by writing a computer program in MATLAB program (version 7.6).

Keywords : Finite difference , water pollution , dissolved oxygen.

المستخلص

لتقييم الأثر البيئي من التلوث ، والنماذج الرياضية تلعب دوراً رئيسياً في التنبؤ مستوى التلوث في المناطق التي هي قيد الدراسة. أصبحت النماذج الحاسوبية أدوات هامة على نحو متزايد في كل جوانب الإدارة البيئية. تم في هذا البحث نمذجة رياضية لنوعية المياه ذات البعد الواحد (معادلة التدفق والانتشار) للمكون البيئي الأوكسجين الذائب في مياه هور ابوزرك. تم حل المعادلة النموذجية الرياضية عددياً باستخدام طريقة Finite Difference بالاستعانة ببرنامج كومبيوتر (Matlab v . 7.6).

1. Introduction

Marshes of Iraq are located in the Southern part of the country. They cover an area of about 20000 km². Abu Zirig marsh is located in the south of Iraq, at the tail end of Gharraf River southerly of Al Islah District in north of Nassiriah Governorate. This marsh is located in the west of the marshes in Iraq in longitude E 46° 36' 33.0" and latitude N 31° 09' 54.9" in north of the marsh, as shown in Figure(1).

The two main towns around the marsh are the cities of Al Islah (pop. 9,000) in the north and Al Fuhud (pop. 18,000) in the south. Scattered villages of fishermen are located all along the embankments that surround the marsh. ^[1]

Site Location:

Lat (N) 31° 09' 54.9", Lon (E) 46° 36' 33.0"

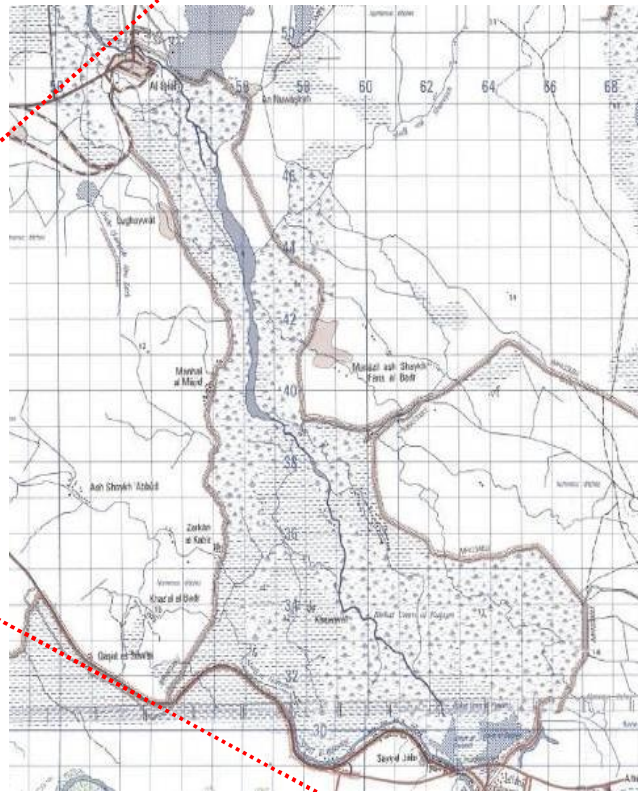


Figure (1). The location of Abu Zirig marsh in Iraq. ^[5]

Most of the researchers studied the water quality parameters in Iraqi marshes, but the studies about the modeling of pollutant transport in the marsh water are limited. The Abu Zirig marsh water is used for a several purposes mainly as potable water and for irrigation, The major sources of Abu Zirig marsh water pollution are industrial effluents released through shat-Algharaf and municipal wastewater.

The marsh is located in a natural depression. A series of embankments, built in 1920, protects the agricultural farms around the perimeter of the natural depression that forms the deep marsh of Abu Zirig. The main supply of water to the marsh is through Shatt Abu Lihia and the channel of this river runs through the marsh until it dissipates at the tail end into the larger marsh (Central Marsh). This marsh re-flooded in June 2003 as a result of the direct action of the local population. The area is about 120 km², and recovery is progressing very well, with reeds growing higher than 2 meters. Water flow into the marsh has been regulated in the Gharraf River. As a result of regulation of Gharraf River, the marsh remains in a very healthy state, despite the oncoming of summer months. ^[2]

Abu Zirig marsh is about 3% of all marshes in Iraq, and dried in 1991 with all the central marshes. This marsh has a single inlet in the north (Gharraf River) and 20 small

outlets in the south. These outlets discharge to the central marsh (Qurnah Marsh) between Tigris and Euphrates^[3]. This marsh is divided into two zones ,the first zone is the upper zone, and other zone is the lower zone, which are divided by road, as shown in Figure (2). This road has pipes and broken areas in 6 points collection between them^[4].

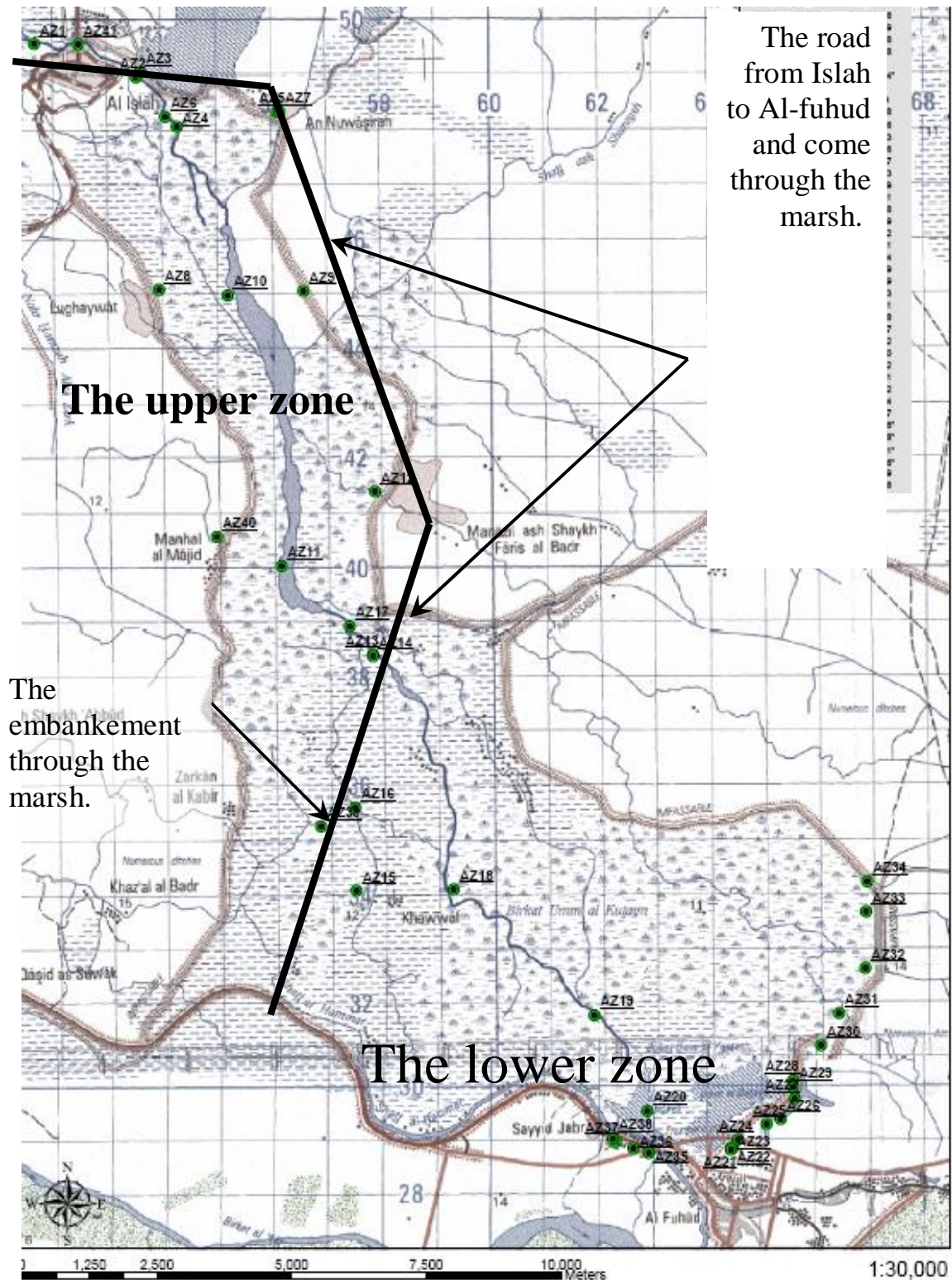


Figure (2). The upper & lower zone in Abu Zirig marshes.

3. Previous studies

Hassan F. M. (1988) studied the physical and chemical properties of Hammar marsh and their effects on the plants. This study covered the water temperature, pH, and electrical conductivity in Hammar Marsh seasonally for one year. He found that water temperature ranges from 9.9 to 34.3°C, the pH ranges from 7.2 to 8.7 and conductivity ranges from 1730 to 7100 $\mu\text{S}/\text{cm}$.

Hussein N. A. (1994) studied the main marshes, and made many measurements like air temperature, water temperature, salinity, pH, conductivity, and dissolved oxygen with some chemical, physical, and biological parameters. All these studies were seasonally in all the marshes in south of Iraq. These researches indicate that salinity increased to 6.250 ppt (parts per thousand) in 1991 depending on the inlet water from Tigris and Euphrates and there is more than the salinity in the northern part of the rivers. The D.O. depends on the plants and is less than 4 mg/l in the closed area.

Schaffranek, R.W., and Lai, C., (1996), used the friction-slope term in the unsteady open-channel flow equations which were examined using two numerical models based on different formulations of the governing equations and employing different solution methods. Results of numerical experiments illustrate that a given model can respond inconsistently for the identical resistance-coefficient value under different types and combinations of boundary conditions. Discussion of qualitative considerations and quantitative experimental results provides insight into the proper treatment, evaluation, and significance of the friction-slope term, thereby offering practical guidelines for model implementation and calibration.

Chapra (1997) classifies water quality models as empirical and mechanistic models. The empirical models are based on an inductive or data-based approach. It involves obtaining set of model input data from many systems that are similar to the water system going to be modeled (Chapra, 1997). The mechanistic models are based on a deductive or theoretical approach. The mechanistic model involves the use of theoretical relationships or organizing principles.

IMET and IF-2 (2004) calculate the area of water surfaces of all big marshes. The area of water surfaces of the Central Marsh is about 3000 km². 700 km² of the Central Marsh are natural lakes with a flow rate of about 400 m³/s. with an average depth of about 1.75 m and salinity ranging from 0.2 ppt to 1.5 ppt. The area of water surface of Hawaizah Marsh is about 3500 km² and 650 km² of Hawaizah Marsh is permanent marsh with average depth of 2.5 m and salinity ranging from 0.3 ppt to 2 ppt. At flood season, the area of water surface of

Hammar Marsh reaches 3000 km² and the total storage of 5 BCM (billion cubic meters). At dry season, the area of water surface of Hammar Marsh is 600 km² and the total storage capacity is approximately of 0.18 BCM, with a high salinity of about 0.5 ppt to 10 ppt.

4. Data collection

4.1 Hydrological balance(water –budget)

Discharge: The marsh, for this purpose has been divided into two sectors namely the Upper zone between Islah and Said Yousha'a road embankment and the Lower zone between Said Yousha'a and Al Fuhud Figure (3). Discharge inlet to the upper zone in Islah Breach is computed and output discharge in Al- Subahaa and Abu Al-jarry was also estimated the output discharge is the same input discharge to the lower zone of Abu Zirig marsh output of the lower zone and marsh also computed, It should be noted that when water levels are high, the culverts built under the embankment suffer from piping and frequent road cuts result this past flood season from the high water flows.

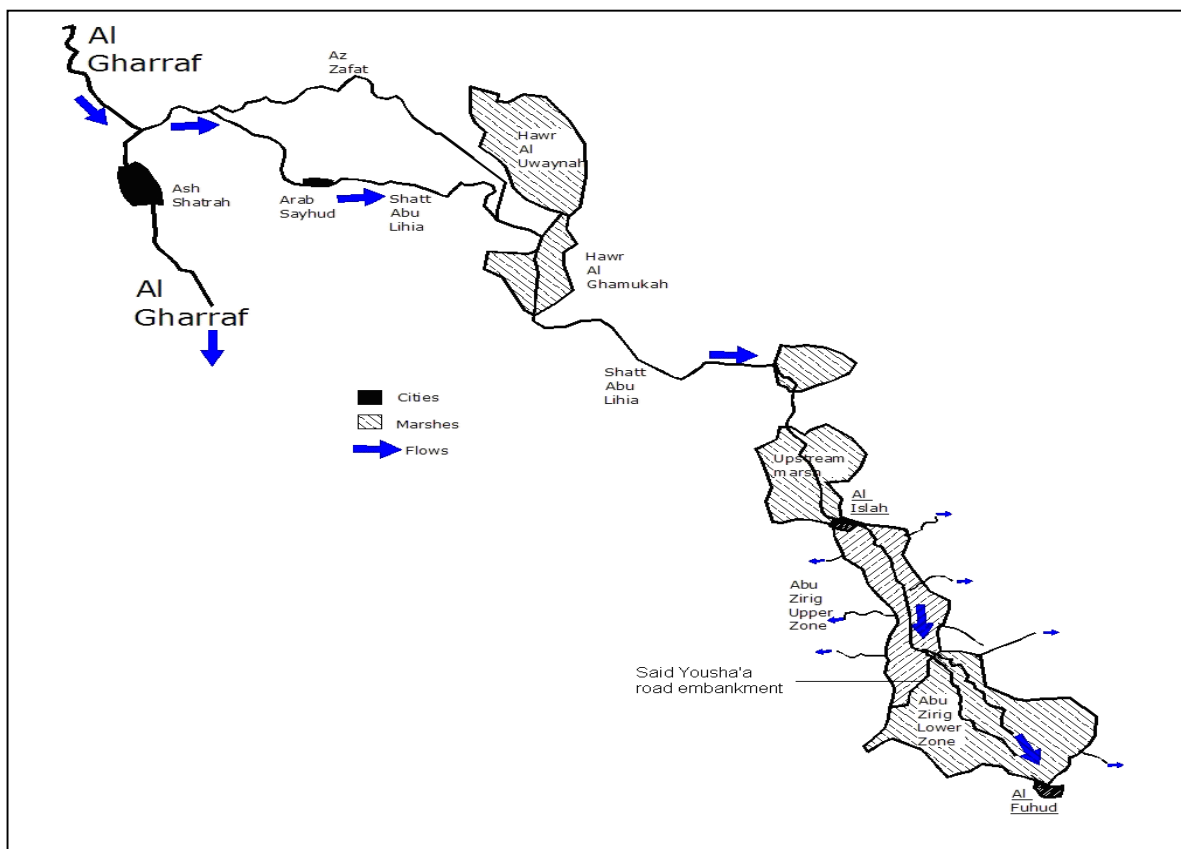


Figure (3). The hydrologic network and the road halves Abu Zirig marsh to the upper and lower part.

Discharge is calculated upstream Islah bridge in Abu Lihia River at the tail end of Gharraf River before entering the marsh, the discharge is calculated at this location by a stage measure which is readily available to measure the water surface elevation (it is attached to the bridge) and so as to be able to account for the water losses between inlet area and the main entrance to the marsh. The values of discharge are listed in table (1) from April 2004 to March 2005^[7], average flow through this location is 32.485 m³/s.

The second location for computing discharge is the Inlet area at the Islah Breach this is the main inlet to the marsh. Water entering this section should be the one measured at upstream Islah bridge minus the one exiting at Islah Channel. In reality, it is not always possible to balance this simple equation (possibly due to error in the measurements as well as uncounted outlets or losses). The average flow through this location is 25 m³/sec. It also should be noted that water fluctuation during the months is not directly related to water availability in the rest of the country (Rzoska J. et al 1980)^[9].

It has been observed that, when water discharge exceeds 25-30 m³/s at the Islah Bridge, this might cause dangerous conditions inside the marshes both for the local population (which gets flooded) and the vegetation (which starts dying due to the excess of water). It should also be noted that, during December 2004, the local population opened a second breach along the north embankment^[2] so as to modify the amount of water entering Abu Zirig from the Islah breach.

The third location is the output from upper zone in which there are many output from this zone (between al-subahaa & al-smesm, al-subahaa and Abu Aljarry) this location represents the inlet supply water to the lower zone in the marsh.

The fourth point represents the output from the lower zone and marsh these points located in right and left Al-Fhud city

Table (1) presents a detailed description of each average inlet and outlet discharge in Abu Zirig marsh for 2004 and 2005^[5].

Table (1). Water balance between Upstream ,Upper &lower zone.

months	Average discharge				
	Upstream	Upper zone		Lower zone	
		In	Out	In	Out
Apr 04	46.01	32.133	18.33	18.33	1.43
May 04	33.28	22.42	14.52	14.52	12.49
June 04	34.23	28.06	18.06	18.06	16.63
July 04	25.08	24.42	16.303	16.303	15.868
Aug 04	19.28	17.5	15.214	15.214	14.703
Sep 04	32.167	28.12	16.938	16.938	15.62
Oct 04	42.067	31.774	25.882	25.882	5.877
Nov 04	24.574	18.5	9.278	9.278	6.369
Dec 04	27.45	19.867	11.25	11.25	9.375
Jan 05	42.45	33.32	21.75	21.75	17.5
Feb 05	44.56	32	20.55	20.55	17.765
Mar 05	38.65	22.42	13.45	13.45	11.45

Table (2). Monthly water quality.

Month	Sample Site	Discharge Q m ³ /s	Dissolved Oxygen Ppm	Velocity m/s	Height m
April	AZ2	28.08	7.7	0.334	1.87
	AZ14	5.506	11.2	0.19	1.7
	AZ20	0.212	7.03	0.012	2.1
May	AZ2	16.38	8.4	0.31	1.76
	AZ14	7.989	7	0.27	1.825
	AZ20	3.745	11.2	0.57	0.65
June	AZ2	28.06	6.4	0.46	2
	AZ14	11.36	4.5	1.08	1.52
	AZ20	7.8	6.716	0.39	1.65
July	AZ2	21.6	6.64	0.28	1.56
	AZ14	9.55	3.35	0.99	1.71
	AZ20	3.637	0.1	0.24	1.25

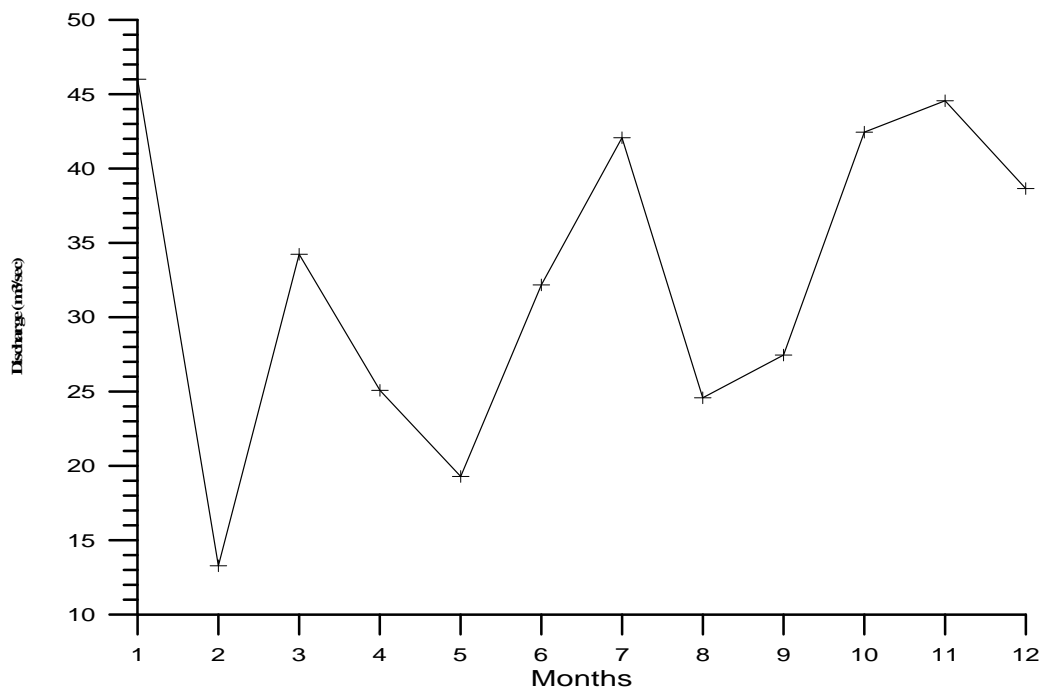


Figure (4). Discharge upstream Islah bridge in Abu Lihia river.

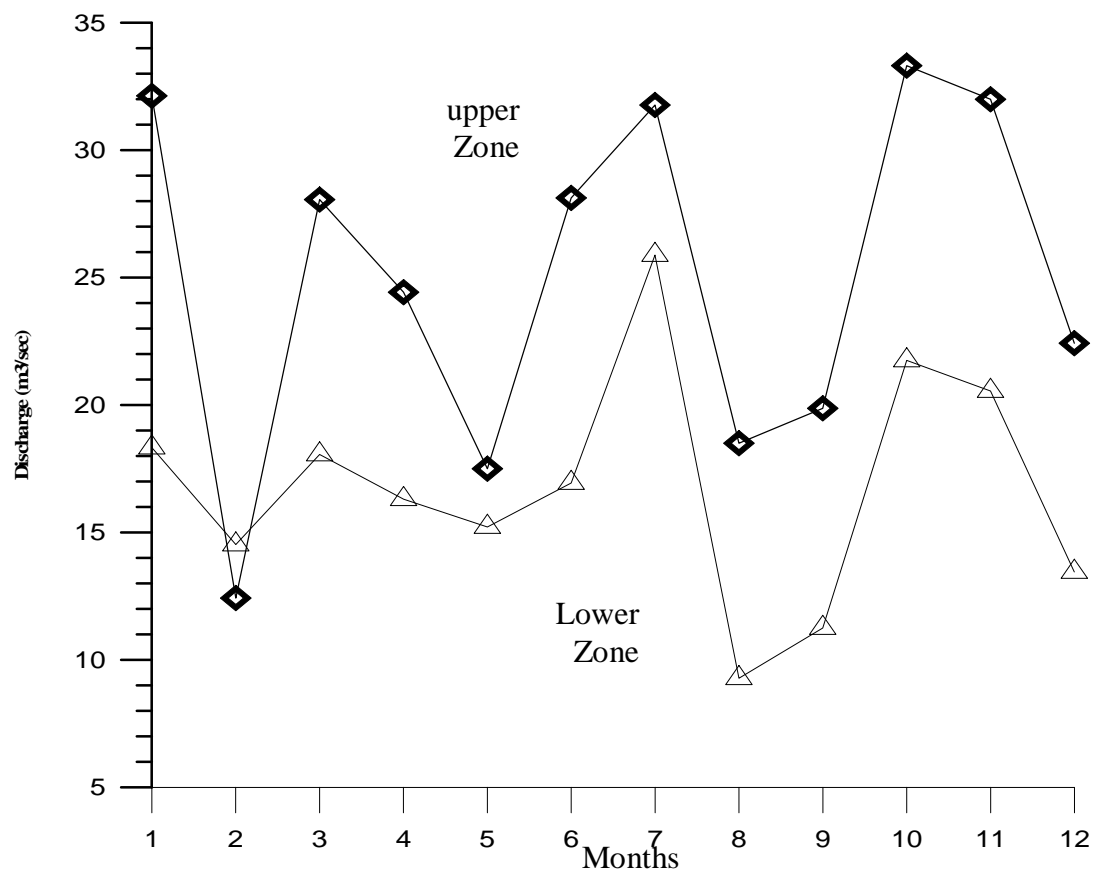


Figure (5). Inlet and outlet discharge from upper zone.

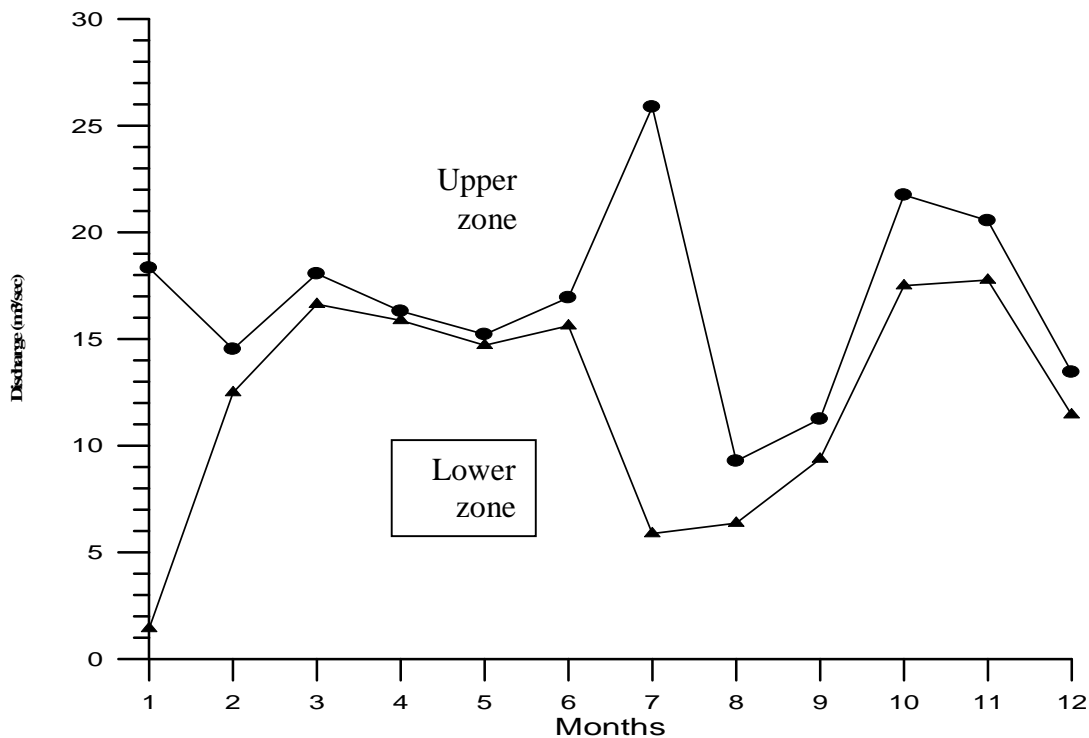


Figure (6). Inlet and outlet discharge from lower zone.

4.2 Dissolved Oxygen

Oxygen is required to support aquatic life and maintain water quality, it is the most important dissolved gas in water. Water in equilibrium with air at 25°C contains 8.3 mg/L of dissolved O₂. Although water molecules contain an oxygen atom, this oxygen is not available for aquatic organisms use in natural waters. A small amount of oxygen, up to ten molecules of oxygen per million of water, is actually dissolved in water. Fish and zooplankton breath dissolved oxygen, and without sufficient oxygen mortality will occur.

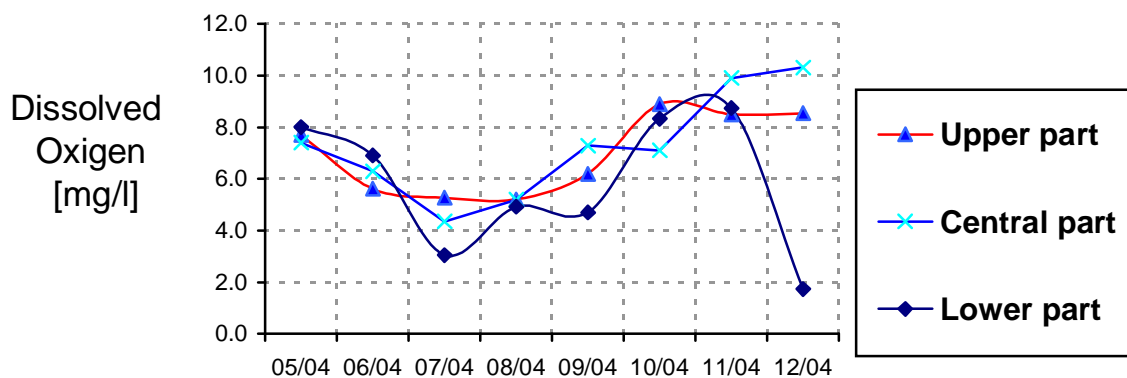


Figure (7) .Dissolved Oxygen concentration for three parts of Abu Zirig water.

5. Mass transport terms for deriving the basic model

The 1-D transport equation can be generalized for dissolved oxygen constituent as :

$$\frac{\partial M}{\partial t} = \frac{\partial \left(AD \frac{\partial C}{\partial x} \right)}{\partial x} dx - \frac{\partial (AVC)}{\partial x} dx + (A dx) \frac{dC}{dt} + S \quad (1)$$

Where:

- M = mass (Kg)
- X = distance (m)
- t = time (Sec.)
- C = concentration (Kg m⁻³)
- Ax = cross-sectional area (m²)
- DL = dispersion coefficient (m².sec.⁻¹)
- U = mean velocity (m. sec⁻¹)
- S = external source or sinks (m. sec⁻¹)

5.1 Assumptions and functional modifications

The basic equation solved in the study was the one dimensional advection-dispersion mass transport equation as defined by (Eq.3 and 4). In the study, this general equation was modified based on the following assumptions:

Because M = VC, we can write

$$\frac{\partial M}{\partial t} = \frac{\partial (CV^*)}{\partial t} = V^* \frac{\partial C}{\partial t} + C \frac{\partial V^*}{\partial t} \quad (2)$$

- With steady state, non uniform flow velocity i.e $\frac{\partial Q}{\partial t} = 0, \frac{\partial V^*}{\partial t} = 0$.
- No external source or sink therefore, the term (S=0).
- Conservative (non-reactive contaminant) was considered $V^* \frac{dC}{dt} = 0$

Divide equ.(1) by $V^* = A dx$ becomes

$$\frac{\partial C}{\partial t} = \frac{\partial \left(D \frac{\partial C}{\partial x} \right)}{\partial x} - \frac{\partial (VC)}{\partial x} \quad (3)$$

$$\frac{\partial C}{\partial t} = D \frac{\partial^2 C}{\partial x^2} - V \frac{\partial C}{\partial x} \quad (4)$$

Clearly, Equation (3) demonstrates the direct dependency of pollutants transport to longitudinal dispersion coefficient. Owing to the importance of longitudinal dispersion coefficient in water quality related issues, many studies have been developed to predict longitudinal dispersion coefficient in surface water after the first study of Taylor in 1953. When the 1D dispersion model is applied to predict concentration variation in surface water, the selection of a proper dispersion coefficient is the most important task. When mixing and dispersion characteristics are unknown, the dispersion coefficient can only be estimated using empirical or theoretical equations .

According to the comparative examination made on these eight methods, the equation developed by Deng et al. (2001) is found to be most reliable method for predicting longitudinal dispersion coefficient

Therefore, in the study the empirical relation developed by Deng et al (2001); Equation (5), was used for determining the dispersion coefficient of the surface water.

$$\frac{D}{HU} = \frac{0.15}{8 * \varepsilon} * \left(\frac{W}{H}\right)^{\frac{5}{3}} * \left(\frac{V}{U}\right)^2 \quad (5)$$

$$\varepsilon = 0.145 + \left(\frac{1}{3520}\right) * \left(\frac{V}{U}\right) * \left(\frac{W}{H}\right)^{1.38} \quad (6)$$

$$U = \sqrt{gsH} \quad (7)$$

$$A = \frac{Q}{V} \quad (8)$$

$$W = \frac{V}{H} \quad (9)$$

Where:

- H = marsh depth (m)
- W = marsh width (m)
- U = marsh bed shear velocity (m/sec.)

- g = gravitational constant.
- S = slope.

5.2. Numerical solution

All the above discussions are aimed on providing the model framework for the marsh which obtains solutions numerically (or the computational representation of the marsh). Due to the complexity of water quality modeling, it has been shown that the most appropriate approach is to utilize numerical solution techniques rather than analytical approaches (Marquette, 2005).

Therefore, in this study, a forward finite difference scheme based explicit finite difference discretization method was applied.

The upper limit of the study area is located between latitude N 31° 09' 55" and latitude N 31° 06' 25". The lower limit of the river section was estimated about 10.3 Km downstream from AZ14 and located between latitude N 31° 02' 31" and latitude N 30° 59' 02".

All the above discussions were aimed to provide the model framework for the marsh. How the model obtains solutions numerically (or the computational representation of the marsh) is presented.

To apply the finite difference method, the spatial domain $[0, x_f]$ was divided into M sections, each of length $\Delta x = x_f/M$, and divided the time domain $[0, T]$ into N segments, each of duration $\Delta t = T/N$, and then replace the second partial derivative on the left-hand side and the first partial derivative on the right-hand side of the equation (4) by the central difference approximation and the forward difference approximation, respectively, so that we have:

$$\frac{C_i^{k+1} - C_i^k}{\Delta t} = D \frac{C_{i+1}^k - 2C_i^k + C_{i-1}^k}{\Delta x^2} - V \frac{C_{i+1}^k - C_i^k}{\Delta x} \quad (10)$$

$$C_i^{k+1} = (1 - 2r - a)C_i^k + (r + a)C_{i+1}^k + rC_{i-1}^k \quad (11)$$

Which:

$$r = D \frac{\Delta t}{\Delta x^2} \quad (12)$$

$$a = V \frac{\Delta t}{\Delta x} \quad (13)$$

Equation (10) represent a set of simultaneous linear equations whose solution provides the values of C_i for all i 's. MATLAB computer language was used for solving this problem.

The model input data has an average values for flow rates, velocity, slope, marsh depth and width.

Initial concentration of dissolved Oxygen:

$C(x,0) = 0$ for lower and upper parts of the marsh.

Boundary conditions with average values:

$C(0,t) = 7.3$ (upper part) and 6.6 (lower part).

$C(x_f,t) = 6.6$ (upper part) and 6.25 (lower part)

6. Result and discussion

The contaminant transport model was solved by implementing the explicit finite difference numerical scheme, while varying the different parameter values. In general, a decrease in contaminant concentration was observed. The concentration of the point source measured for different time periods. The results calculated using the model are displayed in Figures (8,9,10 and 11).As shown in the figures the peak of the spill spreads as time progresses and progressively decays due to dispersion. As it was shown in Figure (8), the peak point reaches about 2 mg/l at $t = 10$ min. ($r=0.1$) for upper part and less than 2 mg/l for the lower part In Figure (10) and (11), after 1/2 hr time ($r=0.3$), the same effect but more decay in concentration due to the dispersion of the chemical and this peak point moved to the last nodal point due to advection mass transport.

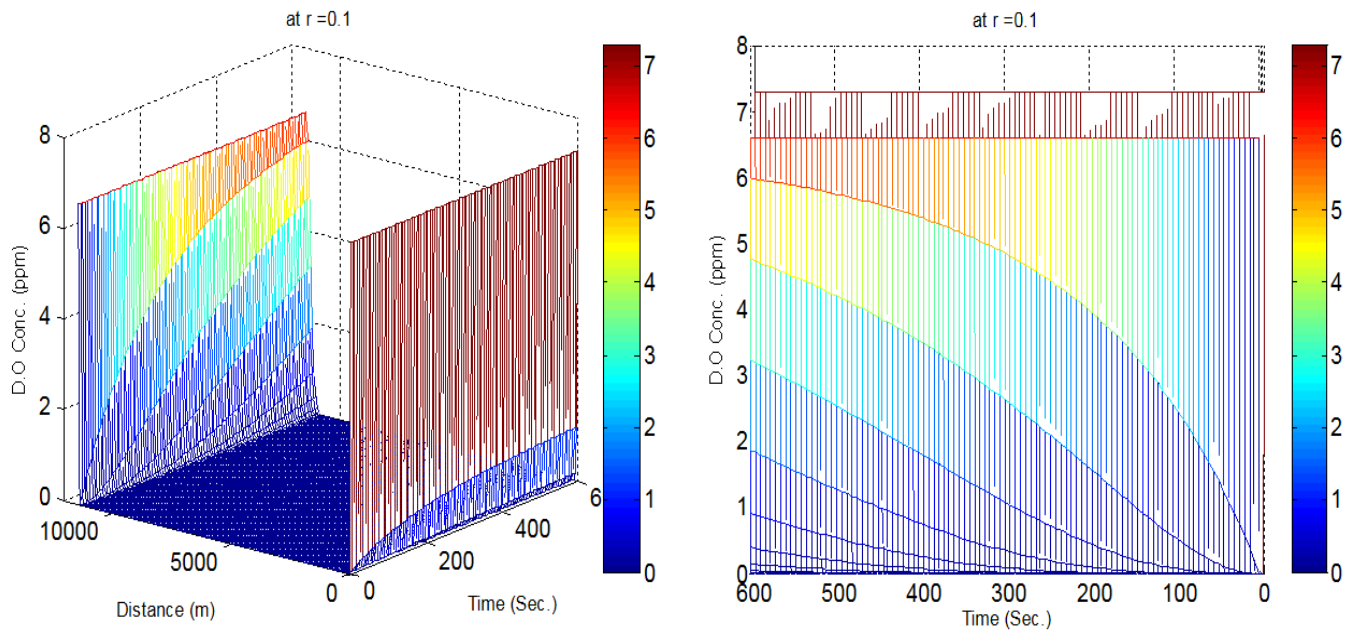


Figure (8).The spatial distribution of D.O conc. in the upper part after 10min .

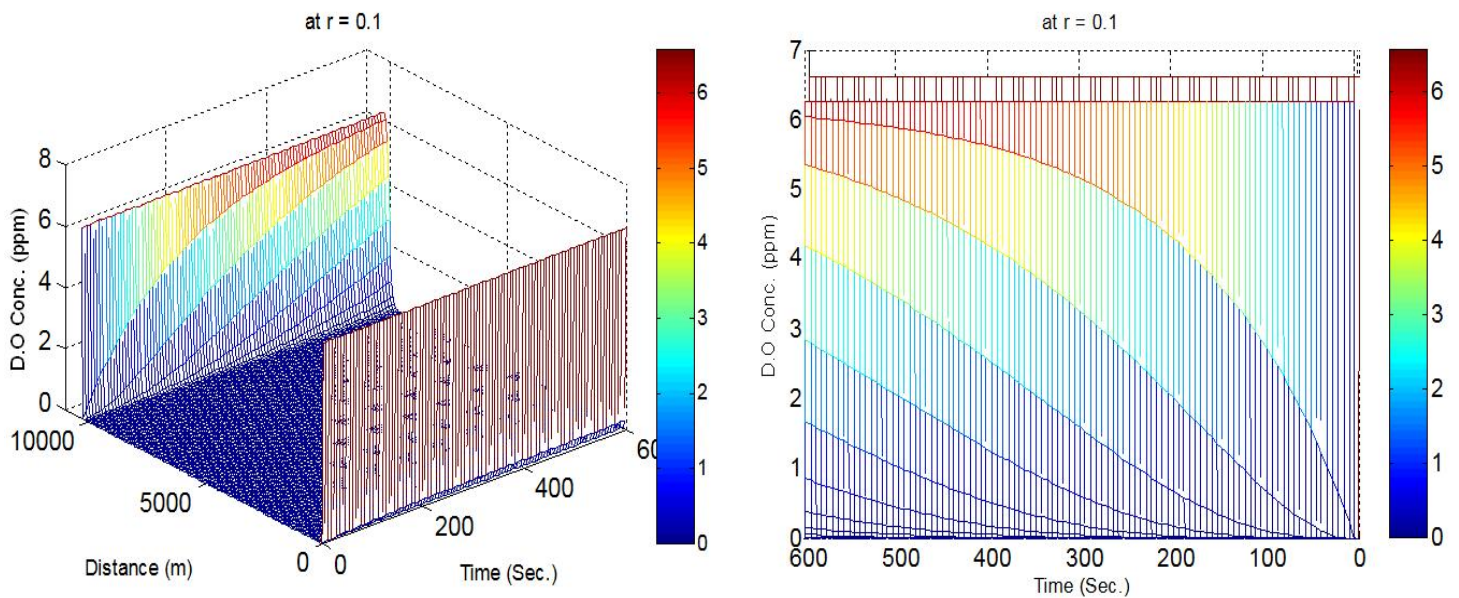


Figure (9).The spatial distribution of D.O conc. in the lower part after 10min .

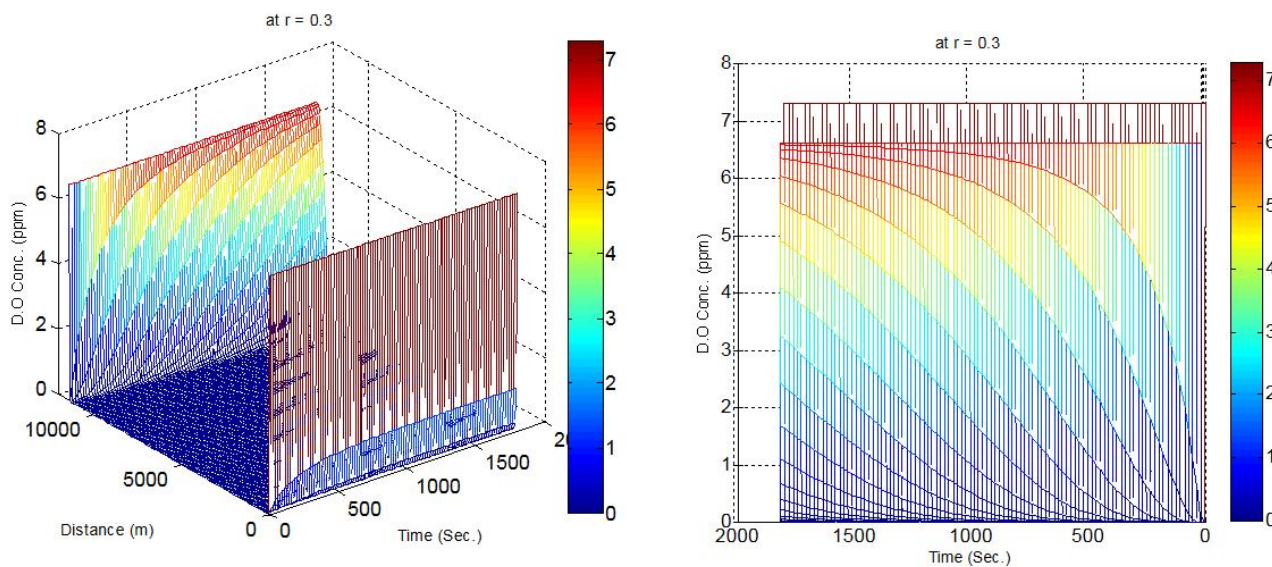


Figure (10).The spatial distribution of D.O conc. in the upper part after 1/2 hr .

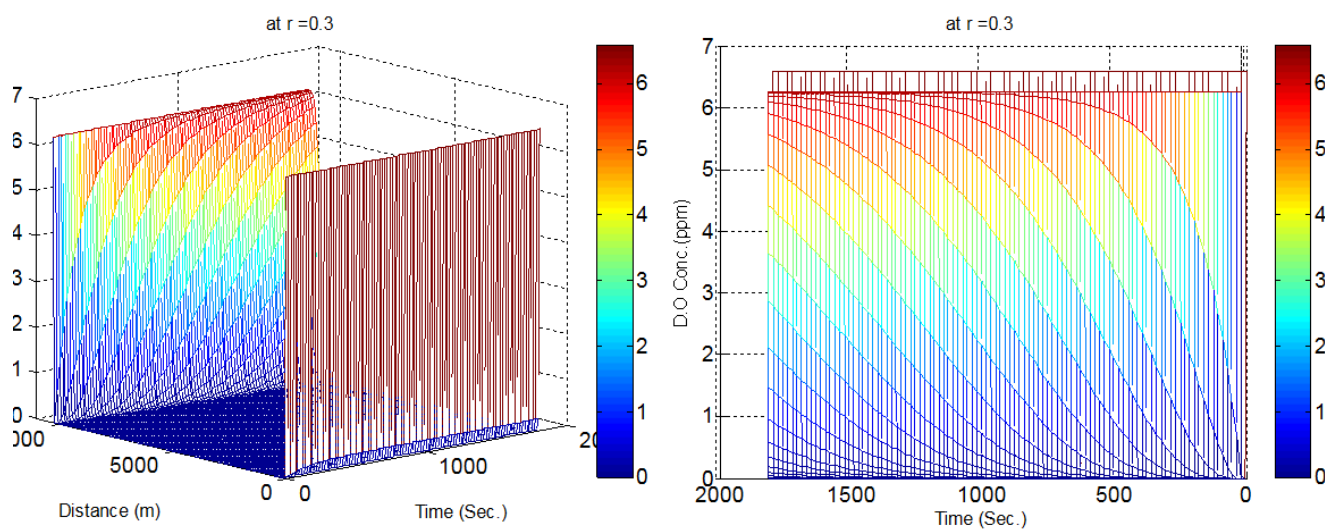


Figure (11).The spatial distribution of D.O conc. In the lower part after 1/2 hr .

As it was shown in all Figures, the concentration of the conservative chemical reaches a constant concentration level. A transition approaches a constant pattern, which is an asymptotic shape in which a zero concentration gradient reached with the upstream. The time required for reaching this constant concentration point varies from location to location. Such curves are referred to as “breakthrough” curves and they are used extensively in both surface water problems context. One of the important uses of these breakthrough curves is in determining the rivers flow and transport properties, particularly for determining the mean advective flow velocity and longitudinal dispersion coefficient of marsh and surface water. As displayed .

7. Conclusion

This paper describes the development of explicit finite difference central scheme for an advection diffusion method. The final model was used to predict the dissolved oxygen concentration. A general one – dimensional computer based mechanistic water quality model has been developed for the upper and lower sections of the Abu-Zirig marsh water. This general water quality model can represent the fate and transport of any contaminant transport in the long sections of the Marsh system.

8. Reference

- [1] Hassan F. M., (1988), "An ecophysiological and qualitative study on phytoplankton in Al-Hammar Marsh-Iraq" B.Sc. in University of Basrah –college of science –Biology- Arabic.
- [2] Saif , Abbas Fr. ,(2005), “Application of hydrodynamic model in Abu Zirig marshland” M.Sc .thesis Environmental Dept. College of Engineering .Al-Mustansiriya Un.
- [3] Abbas J. K. , (2005), “Water quality monitoring of Abu Zirig marsh in southern in Iraq (after drying)” M.Sc. thesis Environmental Dept. College of Engineering .Al-Mustansiriya Un.
- [4] Alwash A. at.el, 1st April (2005), "Technical Book 1 Abu Zirig Marshland Restoration Project", New Eden. <http://www.edenagain.org/marshlandinfo.html>.
- [5] Schaffranek, R.W., and Lai, C., (1996), "Friction term response to boundary-condition type in flow models" American Society of Civil Engineers, Journal of Hydraulic Engineering, New York, v, 122, no.2, p.73-81, Available on line: <http://water.usgs.gov/nrp/proj.bib/abstracts.96.html#schaffranek.lai>

- [6] Hussien N. A., (1994),"Ahwar of Iraq Environmental approach" Seas Researches Center: Number 18, 149p.central of scientific seas.
- [7] Rzoska J. at.el. ,(1980),"Euphrates and Tigris, Mesopotamian ecology and destiny", 119p. The Hague-Boston-London cited by “.Saif ,Fr.Abbas (2005) “Application of hydrodynamic model in Abu Zirig marshland .
- [8] IMET (Italian Ministry of Environment and Territory) and IF (Iraq Foundation-2) (August 2004),"Water and energy project (Interim report)", THE NEW EDEN PROJECT, 207p.
- [9] Al-Sedawi Mohmood S.,(1989),”Surface water Hydrology” 1st edition Bingazi (Arabic).
- [10] Rzoska J. at.el. ,(1980),"Euphrates and Tigris, Mesopotamian ecology and destiny", 119p. The Hague-Boston-London cited by “.Saif ,Fr.Abbas (2005) “Application of hydrodynamic model in Abu Zirig marshland .
- [11] Steven C.Chapra ,(1997), Surface Water Quality Modeling. WCB/McGraw Hill, USA.
- [12] Deng, Z.-Q., Singh, V.P. and Bengtsson, L. ,(2001), Longitudinal dispersion coefficient in straight rivers, Journal of Hydraulic Engineering, American Society of Civil Engineers, 127(11), 919-927.
- [13] Andre Marquette ,(2005), Modeling of Chemical Fate and Transport in the Environment. Master Thesis. Graduate Faculty of the Louisiana State University and Agricultural and Mechanical College, Louisiana, USA.
- [14] Taylor, R. and Krishna, R.: Multicomponent Mass Transfer. John Wiley & Sons, New York ,(1953).

Duplex Inhibition of CO₂ Corrosion in Iraqi Oilfield

Sami I.J. Al-rubaiey

Department of Production Engineering and Metallurgy

University of Technology Baghdad

Abstract

New method for inhibition CO₂ corrosion in Iraqi oilfield was used in this work. This new method included using combination of heat treatment of steel and added Aromatic (Tetrahydronaphthalene) compounds as corrosion inhibitor in different concentration (0.05%, 0.1%, 0.2%, 0.5% and 1%). The results referred that the weight loss was reduced as inhibitor concentration increased for all conditions of specimens whether, there were heat treated or not. The combination of annealing heat treatment of samples and using Aromatic compounds inhibitor offered a better corrosion resistance than the combination of quenching + tempering (Q+T) samples. The presence of inhibitor improves the corrosion resistance for annealed samples. For fully annealing, the weight loss was 5 times lesser than that for (Q+T) samples, while the weight loss of steel (as received condition) was 3 times lesser than that for (Q+T) samples.

Keywords : Inhibition, Oilfield, CO₂ corrosion, heat treatment, Aromatic (Tetrahydronaphthalene) , annealing, quenching , tempering weight loss, efficiency.

المستخلص

استخدمت في هذا البحث طريقة جديدة لحماية الفولاذ المستعمل في الحقول النفطية من التآكل بغاز ثاني اوكسيد الكربون. تتضمن الطريقة الجديدة حماية مزدوجة تعتمد على معاملة الفولاذ حراريا مع إضافة مثبط كيميائي إلى الوسط. استخدم نوعين من المعاملات الحرارية . يتضمن النوع الأول تلدين النماذج بينما أجريت عملية تقسية + عملية مراجعة للنوع الثاني. استخدم مثبط كيميائي من تتراهيدرونفتالين وبتراكيز مختلفة هي: (0.05%, 0.1%, 0.2%, 0.5% and 1%).

أوضحت نتائج البحث إن الفقدان بالوزن يقل بزيادة تركيز المثبط ولجميع حالات النماذج المستخدمة سواء كانت معاملة حراريا أو غير معاملة. إن الحماية المزدوجة المنجزة بإجراء عمليات التلدين للنماذج مع إضافة المثبط الكيميائي أعطت نتائج أفضل من الحماية المزدوجة المنجزة عن طريق إجراء معاملات حرارية تتضمن التقسية + المراجعة مع إضافة المثبط الكيميائي. إن وجود المثبط الكيميائي يحسن مقاومة التآكل للنماذج اللدنة بمقدار خمسة مرات عما هي للنماذج التي أجريت لها عمليات تقسية ومراجعة بينما كان الفقدان بالوزن اقل ثلاث مرات للفولاذ غير المعامل حراريا مقارنة بالفقدان بالوزن للعينات التي اجري لها عمليات تقسية + مراجعة.

1. Introduction

Corrosion in the oilfield is defined as deterioration of a metal by chemical or electrochemical reaction with the environment. Low carbon steel is the most common metal that is utilized in oil and gas production ^[1-3]. CO₂ and H₂S gases in combination with water are the main cause of corrosion in oil and gas production. The most predominant form of corrosion encountered in Oil and Gas production is the one caused by CO₂ ^[3]. Carbon steel has low resistance to CO₂ environments, it is widely used in the petroleum industry mainly due to economical reasons ^[4]. What makes feasible the use of carbon steels is the natural precipitation of protective iron carbonate (FeCO₃) ^[5,6].

The oil and gas industry has been given much attention in recent years because of an increased tendency to inject CO₂ into oil wells to reduce the viscosity of oil and increase its production ^[3].

Carbon dioxide that dissolves in water lowers the pH of the water and increases the corrosion rate. The pH of the water will increase (because of CO₂ evolution) at lower pressures. It should be noted that calcium carbonate and calcium sulfate scales often occur at points where there is a drop in gas pressure ^[3, 4]. Carbon dioxide dissolves in water to form H₂CO₃ carbonic acid (H₂CO₃) is produced with the characteristic that is more aggressive than hydrochloric acid at the same pH ^[5]. Carbonic acid reacts directly with iron to form Fe₂CO₃. The reaction is: $\text{H}_2\text{CO}_3 + \text{Fe} \rightarrow \text{FeCO}_3 + \text{H}_2$

Inhibitor protection seems to be one of the most appropriate and cost efficient ways to address the CO₂ Corrosion problem ^[6, 7]. The inhibitors applied during the operation of oil equipment and pipelines should satisfy a number of engineering requirements: they should be soluble or dispersible in water or brine, they should be easily separable, they should ensure a highly protective effect, they should prevent the formation of pitting, they should prevent the hydrogenation of steel (in the case of the presence of H₂S), and they should be non-toxic.

The more the inhibitor is maintained in the solution, the more the corrosion rate decreases up to a certain concentration which is defined as critical concentration of inhibitor. From the economical point of view, it is desirable to maintain the inhibitor level just on critical concentration, but the corrosion rate increases sharply if the inhibitor concentration become under critical value.

Selection of a particular corrosion inhibitor is usually made based on the f of corrosion, the type of production, prior experience, and laboratory or field testing ^[3]. Corrosion inhibitors which used for oil field applications are very complex compounds. The most

effective corrosion inhibitors, which have been widely used, when carbon steels are exposed to CO₂ environments, can be sorted into four generic groups: amine imidazoline, amines and amine alts, quaternary ammonium salts, and nitrogen heterocyclics. Inhibitors fall into four general categories based on mechanism and composition. These categories are ^[4, 7]:

- 1- Barrier layer formation.
- 2- Neutralizing.
- 3- Scavenging.
- 4- Other environment modification.

Adsorption-type inhibitors are the most common barrier layer inhibitors. These inhibitors form a stable bond with the metallic surface. Typical examples of this type of inhibitor are organic phosphates and chromates. In general, these organic compounds are adsorbed and form a stable bond with the metal surface. The successful application of carbon steels in oil and gas pipelines and production tubular in CO₂ containing environments depends mainly on the formation of protective corrosion product film or the use of corrosion inhibitors ^[1-5]. Barrier layer formation inhibitors form a layer on the corroding metal surface, modifying the surface to reduce the apparent corrosion rate. They represent the largest class of inhibitive substances.

There are three standard treatment methods used for corrosion inhibition in oilfield ^[4, 7]. Continuous treatment, displacement treatment, and squeeze treatment. Continuous treatment involves continuous injection of corrosion inhibitor into the production stream. Treatment concentrations normally range between 5 – 15 ppm for liquid production depending on the concentration of the corroding. The treatment concentration for gas production may be as high as 100 ppm ^[3].

Displacement treatments involve filling the production tubing with corrosion inhibitor, allowing it to stay in contact with the tubing for a period of time (up to several hours) and then producing the inhibitor back through the production equipment. Squeeze treatments are similar to displacement treatments except that the corrosion inhibitor is pumped into the formation. These two treatment methods are usually used in wells with lower production rates.

The use of inhibitor in CO₂ corrosion of carbon and low alloy steels with different chemical composition or different microstructure are not recognized in the literature. These variables are independent; different inhibition can be obtained for different microstructure with addition of different inhibitor or different inhibitor concentrations. Some authors ^[1-3, 8]

reported the effect of one of these parameters without taking into account that the other ^[5, 7, 9] has been also modified. Also the influence of microstructure on the inhibitors performance is still lacking.

The aim of the present work is to use new method for inhibition CO₂ corrosion in Iraqi oilfield. The new method included using combination of heat treatment of steel and added corrosion inhibitor at different concentrations. The effects of water content in oil and the effects of carbon steel microstructure on the efficiency of corrosion inhibitors in CO₂ environments is also considered in this work.

2. Experimental

2.1 Material & specimen preparation

Carbon steel is the most commonly used materials in the fabrication and manufacturing of oil field operating platforms because of their availability, low cost, ease of fabrication, and high strength, therefore rectangular specimens of a carbon steel grade API 5L X65 were used in this research. These specimens were obtained from Kirkuk oilfield. The chemical composition of the investigated specimens was given in Table (1).

Table (1). Chemical compositions of carbon steel samples.

Element	C	Si	Mn	P	S	Cu	Ni	Cr	Fe
Wt%	0.08	0.32	1.47	0.016	0.004	0.10	0.10	0.03	Remains

The specimens were sequentially polished with 240, 320, 420 and 600 grit sandpaper. Then the specimens wash with running tap water followed by distilled water, dried with clean tissue paper immersed in acetone & further cleaned successively with in an ultrasonic bath for 2 minutes. The final dimensions of the specimen were 10mm x 20mm x100 mm.

2.2 Heat treatment

The heat treating procedures were as follows:

2.2.1 Annealing; the specimens were heated to 850 °C in a rotary –diffusion vacuum furnace type (Vacscal VS2) for one hour and then slowly cooled to room temperature.

2.2.2 Quenching; the specimens were heated to 850 °C in vacuum furnace for one hour and then quickly cooled in water bath to room temperature.

2.2.3 Tempering; the quenching specimens were tempered by raising the temperature to 430 °C in vacuum furnace for 2 hours and then slowly cooled down to room temperature.

2.3 Solutions

2.3.1 Solution composition

Table (2) showed the chemical composition of water produced with oil in Kirkuk oilfield from well no. K184. Sodium chloride concentration varied within the range 26000-27000 ppm. A sketch of oil field gathering system is shown in Figure (1).

Table (2). Chemical compositions of water produced with oil.

Component	NaCl	CaHCO ₃	CaSO ₄	CaCl ₂	MgCl ₂
Conc.(ppm)	26500	5670	3450	513	3780

In the present work, water simulation is based only on NaCl concentration of highest level 27000 ppm in distilled water by using equivalent weight of analar NaCl i.e. 27000 ppm, the brine solution was prepared by dissolving analar NaCl in distilled water was being used as the single phase. Different water concentrations of water in oil were used as following: 15%, 25%, 35% and 45%. The solution was saturated by CO₂ with pH = 5 and $p\text{CO}_2 = 0.54$ bar. The experimental conditions are summarized in Table (3).

2.3.2 Inhibitor addition

The Aromatic compounds are chosen in this work to be good a corrosion inhibitor for CO₂ corrosion ^[5, 9, 10]. This compounds were imported from " Akzo Nobel Surfactants company, Stenungsund ,Sweden " .

Aromatic compounds – adsorb onto the steel surface by sharing π -electron density from the aromatic ring with the metal surface. This binding can possibly decrease corrosion rates or change the steel-oil interfacial tension. The aromatic chosen for this study is tetrahydronaphthalene in different concentration 0.05%, 0.1%, 0.2%, 0.5% and 1%.

Table (3). Experimental conditions and measurements.

Total Pressure	1 bar
$p\text{CO}_2$	0.54 bar
Temperature	25 ± 2 °C
Water conc. in oil	15%, 25%, 35% and 45%
pH	5 ± 0.05
Material	X65 steel
Inhibitor	Aromatic (1,2,3,4-Tetrahydronaphthalene) $\text{C}_{10}\text{H}_{12}$ (Molecular weight $\text{g}\cdot\text{mol}^{-1} = 132.2$)
Inhibitor concentrations	(0.05, 0.1, 0.2, 0.5 and 1) %

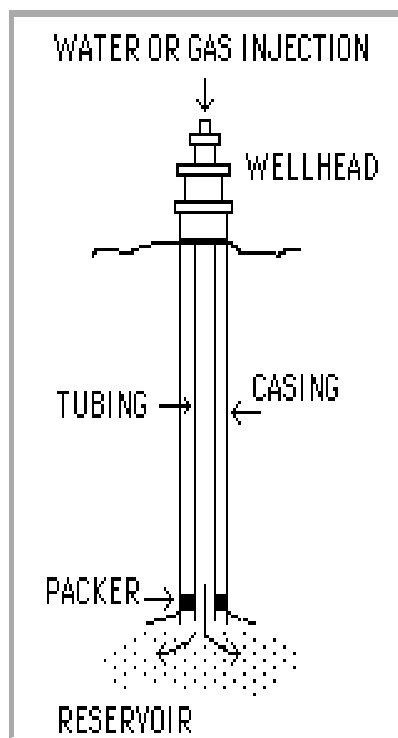


Figure (1). A sketch of a typical oil field gathering system.

2.3.3 Inhibitor Efficiency (λ)

The inhibition efficiency (λ) as calculated according to the following equation ^[1]:

$$(\lambda) = [(W_u - W_i) / W_u] \times 100 \quad (1)$$

Where:

W_u = weight loss of metal in uninhibited solution.

W_i = weight loss of metal in inhibited solution.

2.4 Weight loss technique

The glass cell (beaker) was filled with 250 mL of tested solution that was purged with CO₂ during 2 hrs prior the immersion of the metal coupons. After 2 hrs the oxygen concentration was measured to be less than 10 ppb and the pH was constant (5 ± 0.5) meaning that the system was in equilibrium and saturated with CO₂. The pH of the test solution was adjusted to the desired pH by adding deoxygenated hydrochloric acid solution (HCl). It is important to point out that the CO₂ injection was maintained during the test with the aim of avoiding any oxygen contamination. The cleaned specimens were weighed and exposed to the tested solution. Only one specimen was suspended in each beaker. Test duration was 24 hrs.

After each test, specimens were visually observed. At the end of the experiment, the specimens were final cleaning with brush to remove the corrosion products, immersed in 5% HCl containing hexamine, washed by tap water, rinsed with distilled water, then left to dry and accurately weighed to the 4th decimal of gram. A digital balance with 4 decimal points was used weight the specimens, (type Sartorius BL 2105 Max. 210g, d= 1mg, Germany). The mean value of the weight loss in milligrams was calculated for three test specimens. .

3. Results and discussions

3.1 Effect of water content

The effect of water content in oil solution was studied for the percentages (15%, 25%, 35% and 45%). The carbon steel was found to corrode in the tested solution as shown in Figures (2-4). This was evidenced by the decrease in the original weight of the specimens as the water percent increased. Depending on the water content in oil, the weight loss increase in order:

45% (H₂O) > 35 % (H₂O) > 25% (H₂O) > 15% (H₂O)

These findings were in agreement with results in works ^[1, 5]. The increase in weight loss at high water concentration can attribute to mass transfer rate leading to more water bubbles colliding with the metal surface ^[7]. The water slugs in oil flow pattern appear at high ratios of water in oil (35% and 45%). The slugs of water make good contact with the metal surface. Hence the system is controlled by oxygen diffusion rate.

3.2 Effect of inhibitor concentration

It was observed from Figures (2-4) that, in all cases studied the extent of weight loss decreased with increase in the concentration of the inhibitor. However, the extent of inhibition did not increase in proportion to the increase in the water content in oil, i.e. the inhibitor works relatively more efficiently in dilute solutions of 35% water content in oil. At an inhibitor concentration of 0.05%, the weight loss was 216 mg, whereas when the inhibitor concentration increased to 1%, the weight loss became 102 mg in the same solution as shown in Tables (4-6).

According to ^[1, 10] the inhibitors are believed to be generally molecularly absorbed on the active centers of the metal surface. Thus an absorbed layer characterized by a high electrical resistance is formed on the metal surface which may also be responsible for the reduction in the rate of diffusion of ions necessary for the corrosion process. In the present case also, the

percentage inhibition vs. inhibitor concentration Figures (2-4) resemble absorption and therefore, confirm the theory that, an absorption phenomenon is occurring on the metal surface.

3.3 Inhibitor efficiency

When the extent of inhibition was examined at different concentrations (0.05-1%) in different water content in oil, it was observed that, the extent of inhibition decreased with increase in the concentration of the water content in oil at a fixed inhibitors concentration of all conditions were used. The inhibitive efficiencies of various concentrations of inhibitors Figures(5-7) increased in the order:

At 45% H₂O: 61.2 at 1% Aromatic compounds, 56.8 at 0.5% Aromatic compounds, 53.7 at 0.2% Aromatic compounds, 48.2% at 0.1% Aromatic compounds and 47.3% at 0.05% Aromatic compounds.

The lowest inhibitive efficiency (72%) was obtained with 0.1% concentration whereas the highest efficiency (86%) was achieved at 1% concentration in solution, containing 45% water in oil. Tables (7-9) showed the inhibitor efficiency results of API 5L X65 carbon steel (as received and after heat treatment) in oilfield solution, containing different water content: X1-15% X2-25% X3- 35% X4-45% with different inhibitor concentrations (Y).

The decrease in inhibitive efficiency with increase in H₂O content in oil may be attributed to the high rate of evolution of hydrogen in concentrated solution which may interfere with the absorption of the inhibitor on the metal surface ^[9, 10]. Further, it is interesting to note that, in the case of annealing microstructure the inhibition efficiency remains almost at values about (80.6-84.8%) at all water content with concentrations of inhibitors equal 1%. This may be due to better absorptivity of annealing structure in comparison to other structures.

3.4 Effect of heat treatment

The corrosion behavior of used steel was very dependent on the heat treatment. In order to assess the affectivity of different heat treatment, experiments were carried out at annealing and quenching and tempering samples. It was observed that in all cases the extent of inhibition decreased with a rise in water content in oil. The effect being more prominent in the case of annealing, followed by the received condition and then the samples which quenching + tempering. However in the case of quenching + tempering the decrease was not so perceptible.

At constant water content the inhibitive efficiency of Aromatic compounds increases with increase in the concentration of the inhibitor, whereas at constant inhibitor concentration, the efficiency decreases with increase in the water content in oil.

Annealing condition appears to be good microstructure to decrease weight when an Aromatic compound was used. For this microstructure, the weight loss decreased from 284 mg without inhibitor addition in 45% water content in oil to 22mg when 1% Aromatic compounds added to solution, containing 45% H₂O in oil, whereas the inhibitor efficiency reached to 84.8% in solution of 45% H₂O in oil when inhibitor concentration was 1%. Annealing samples reveal better corrosion resistance compared to Q+T samples (as shown in Tables (7-9)). Works ^[9, 10] analyzed the structure of corrosion scales. They described two types of scales. The primary scale, formed directly on the corroding surface, which is non-compact, porous, with layer crystals and well adhered. Secondary scale, which can be formed on the top of the primary scale due to the recrystallization on iron carbonate. The secondary scale is compact: non-porous & detaches easily. It was concluded that the corrosion products thickness as well as the adherence to the metal surface depend on the microstructure of the specimen. The primary iron carbonate scales formed on normalized samples were thicker, less porous, more tenacious, better adhered than those formed on the samples, which had (Q+T) ones. Moreover, the crystals forming the scale on normalized steel specimens were found to be larger & more densely packed than those for the (Q+T) specimens. The secondary scale has the same characteristics for both types of microstructures.

The combination of annealing heat treatment of samples and using Aromatic compounds inhibitor offered a better corrosion resistance than the combination of (Q+T) samples.

Annealed samples have better corrosion resistance than the Q+T samples ones. In annealing condition, the corrosion rate was further decreased as inhibitor content increased. In Q+T heat treatment. The corrosion rate was higher than that in annealing condition. The difference in corrosion rate is assigned to the different precipitated phases and their shape & distribution resulting from different heat treatment. The corrosion rate decreases as the ferrite increase as shown in condition of steel as received which contain ferrite more than those in (Q+T) condition of steel.

The microstructure of used steel (as received) presented a weight loss equal to 38 mg in solution containing 15% water and 1% Aromatic compounds in oil solution. These values were higher than that values for the microstructure in the annealed condition in which weight loss equal to 22 mg in the same condition for steel as received. Even more, for (Q+T) microstructure of steel, weight loss was 102 mg in solution contained 35% H₂O and 1%

Aromatic compounds in oil solution, while in solution contained 15% H₂O and 1% Aromatic compounds, the weight loss was 115 mg. It is necessary to note that, the inhibition action due to combination of (Q+T) and using Aromatic compounds as inhibitor had independent relationships.

The adherence of the corrosion product film was higher in the quenched samples and they were stiff & tough. The annealed samples surface contained large carbides in the corrosion product therefore; the corrosion rates in this condition were lower than those of Q+T samples. However, the Q+T lead to a decrease in corrosion rate. No protective film was formed on the F/P.

Figures (1-3) showed the relationship between Inhibitor concentration and weight loss of specimens. The inhibitor dosage had been increased from 0.05% to 1%. It should be noted that the weight loss was reduced as inhibitor concentration increased for all conditions of specimens whether, there were heat treated or not. These results are attributed to increase the resistivity of solution and decrease the contact between the metal and the aqueous solution [1, 7, 8].

By comparing Figures (1-3) it can be seen that the presence of inhibitor improves the corrosion resistance for annealed samples. For fully annealing, the weight loss was 5 times lesser than that for (Q+T) samples, while the weight loss of steel (as received condition) was 3 times lesser than that for (Q+T) samples.

These results could be attributed to the microstructures as shown in Figure (8), when the samples had annealed ferrite & pearlite were precipitated while for quenching and tempering samples of temper martensite phase would precipitated ^[9]. The structure of annealed steel served to show the difference between the phase and constituent concepts. In Figure (8 B), two basic types of structures were clearly evident: the white areas are ferrite and the dark (black) areas are pearlite. The constituents of these specimens are, accordingly, pearlite and ferrite.

Steels that have undergone a simple hardening quench are usually mixtures of austenite and martensite, with the latter constituent predominating. Both of these structures are unstable and slowly decompose, at least in part, if left at room temperature: the retained austenite transforms to martensite. A structure, which is almost completely martensite is extremely brittle and is also very liable to develop quench cracks if aged at room temperature, therefore steels with a simple martensitic structure are of little useful value, and a simple heat treatment called tempering is almost used to improve the properties of quenching steels. In this treatment, the temperature of steel is raised to 430 °C in vacuum furnace, held there for a

fixed 2 hours, after which the steel slowly cooled down to room temperature. The obvious intent of tempering is to allow diffusion processes time to produce both a dimensionally more stable structure and one that is inherently less brittle.

They also observed differences in the inhibitor efficiency Figures (4-6) that were attributed to variations in the microstructure in the steel Figures (7 and 8). The inhibitor efficiency increased with an increase in the inhibitor concentration for all microstructures.

In the case of CO₂ corrosion the anodic and cathodic reactions are the oxidation of iron and the reduction of hydrogen, respectively ^[6]. If it is considered that the active sites on the metal surface are the same for both reactions before adding the inhibitor. When the inhibitor is present because its adsorption changes those active sites and therefore the anodic and cathodic reaction rates. Another important aspect is that the change in inhibitor concentration is proportional to the inhibitor efficiency Figure (3), Table (2). Higher efficiencies were observed when the change in inhibitor concentration was toward more values.

Works ^[5, 10] reported similar results. They attributed the loss of inhibition efficiency, with the inhibitor concentration, to the tendency of inhibitor molecules to repel each other. When the inhibitor concentration was greater than 10 ppm, the inhibitor molecules tended to perpendicularly adsorb on the metal surface due to a repellent function ^[1,6]. As a consequence, instead of adsorbing parallel to the metal surface, decreasing the active sites, the inhibitor molecules would cover a smaller metal surface area, which resulted in a less corrosion efficiency.

The adsorption of inhibitors on the metal surface has been studied recently by ^[7] by molecular modeling. The inhibitor molecules had larger adsorption energy than the water molecule. This means that the inhibitor molecules adsorb preferentially on the metal surface in aqueous medium, justifying the rapid decrease weight loss when the inhibitor is added.

4. Conclusions

1- Weight loss increases as water content in oil solution increases in order:

45% (H₂O) > 35 % (H₂O) > 25% (H₂O) > 15% (H₂O)

2- In all cases studied the extent of weight loss decreased with increase in the concentration of the inhibitor but the extent of inhibition did not increase in proportion to the increase in the water content in oil, i.e. the inhibitor works relatively more efficiently in dilute solutions of 35% water content in oil. .

3- The inhibitive efficiencies of various concentrations of inhibitors increased in the order:

At 45% H₂O: 61.2 at 1% Aromatic compounds, 56.8 at 0.5% Aromatic compounds, 53.7 at 0.2% Aromatic compounds, 48.2% at 0.1% Aromatic compounds and 47.3% at 0.05% Aromatic compounds.

- 4- The corrosion behavior of used steel was very dependent on the heat treatment. The effect being more prominent in the case of annealing, followed by the received condition and then the samples which quenching + tempering.
- 5- The combination of annealing heat treatment of samples and using Aromatic compounds inhibitor offered a better corrosion resistance than the combination of (Q+T) samples.

5. References

- [1] Durnie W. H., Marco R. D., Kinsella B. J., and Jefferson A., 1998, "Predicting the performance of oil field corrosion inhibitors from their molecular properties", Corrosion and prevention conference, 23-25th November 1998, Hobart, Australia, pp. 187-192.
- [2] Osarolube, E., Owate, I. O. and Oforka, N. C., June 2008, "Corrosion behaviour of mild and high carbon steels in various acidic media". Scientific Research and Essay Vol.3 (6), pp. 224-228.
- [3] Fontana M.G. & N.D. Greene Corrosion Engineering, 3rd ed. Mc Graw-Hill International Ed. 1987. p.171.
- [4] Efirid K. D., 1988, "Petroleum"; Corrosion tests and standards metal, American Society for Testing and Materials, Chap. 36, pp. 350-358.
- [5] Farelal F., Ramirez A., 2010, "Carbon Dioxide Corrosion Inhibition of Carbon Steels Through Bis-imidazoline and Imidazoline Compounds Studied by EIS" Int. J. Electrochem. Sci., Vol. 5, pp. 797 – 814.
- [6] Marsh J. and Teh T.; Ionik Consulting/JPKenny Caledonia, September 2007, "Conflicting Views: CO₂ Corrosion Models, Corrosion Inhibitor Availability Philosophies, and the Effect on Subsea Systems and Pipeline Design" paper SPE 109209, Offshore Europe 2007 held in Aberdeen, Scotland, U.K., 4-7.
- [7] Durnie W. H., Marco R. De, Jefferson A. and Kinsella J., 2003, "In situ study of the adsorption of inhibitors of carbon dioxide corrosion"; Surface and interface analysis, Vol. 35, pp. 536-543.

- [8] Ruslan Vagapov , 2009,"Corrosion Inhibitors for the Protection of Oil Production Equipment" Scientific Research Institute of Natural Gases and Gas Technologies. J. Exploration & production Vol.7, ISSUE 1, pp.66-68.E.
- [9] A.J. Szyprowski, 2000, "Relationship between chemical structure of imidazoline inhibitors and their effectiveness against hydrogen sulphide corrosion of steels"; British Corrosion Journal, Vol. 35, pp. 155.
- [10] M.A. Deyab, H.A. Abo Dief, E.A. Eissa, A.R. Taman, 2007, "Electrochemical investigations of naphthenic acid corrosion for carbon steel and the inhibitive effect by some ethoxylated fatty acids", Electrochimica Acta 52, pp 8105–8110. O L U M E 7 I S.

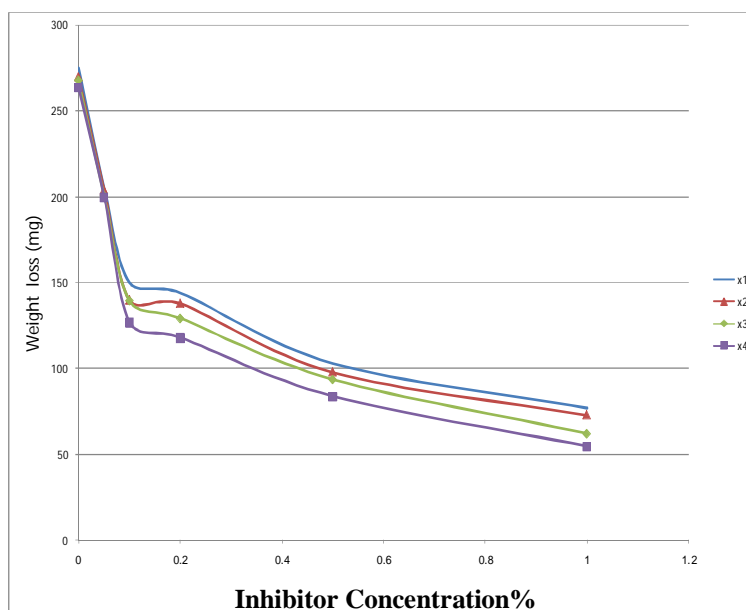


Figure (2). Variation of weight loss with different inhibitor concentrations for API 5L X65 carbon steel (as received) in oilfield solution, containing different water content: 1- 15% 2-25% 3- 35% 4-45%.

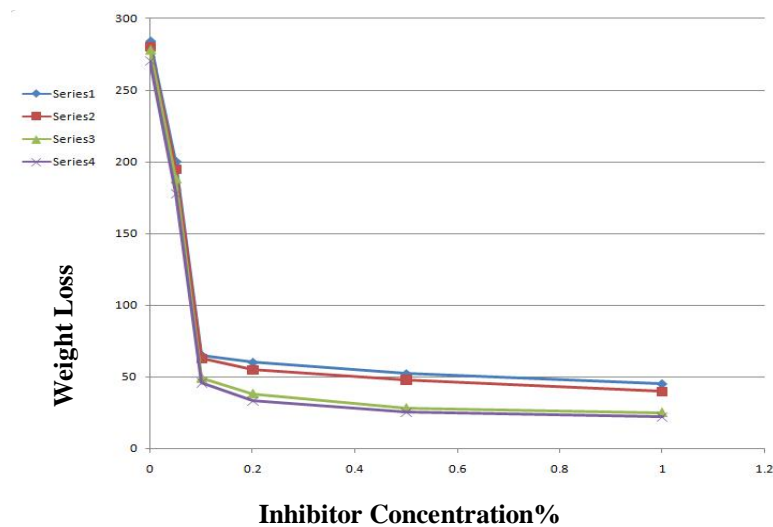


Figure (3). Variation of weight loss with different inhibitor concentrations for API 5L X65 carbon steel (after annealing) in oilfield solution, containing different water content: 1-15% 2-25% 3- 35% 4-45%.

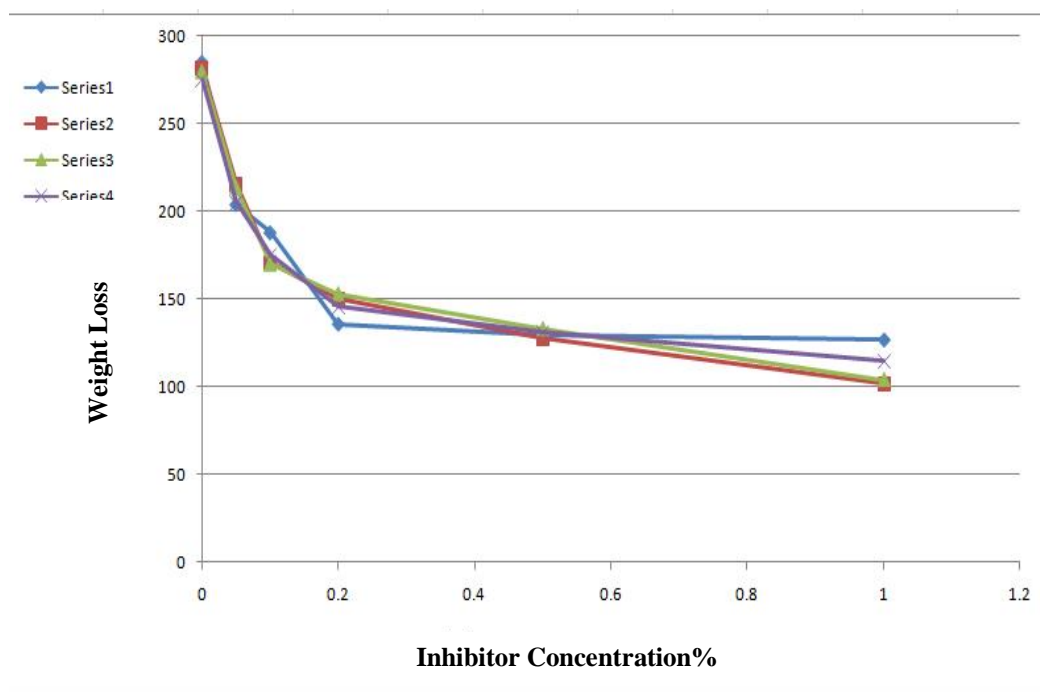


Figure (4). Variation of weight loss with different inhibitor concentrations for API 5L X65 carbon steel (after quenching + tempering) in oilfield solution, containing different water content: 1-15% 2-25% 3- 35%4-45%45%.

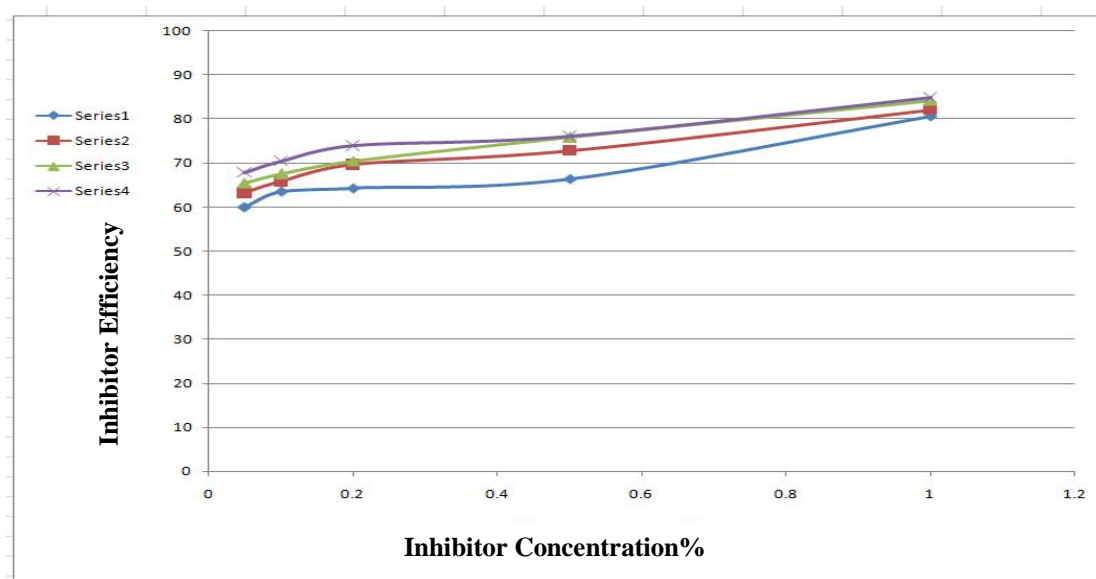


Figure (5). Effect of concentration of Aromatic compounds on their efficiency as inhibitors for API 5L X65 carbon steel (after annealing) in oilfield solution, containing different water content: 1-15% 2-25% 3- 35% 4-45%.

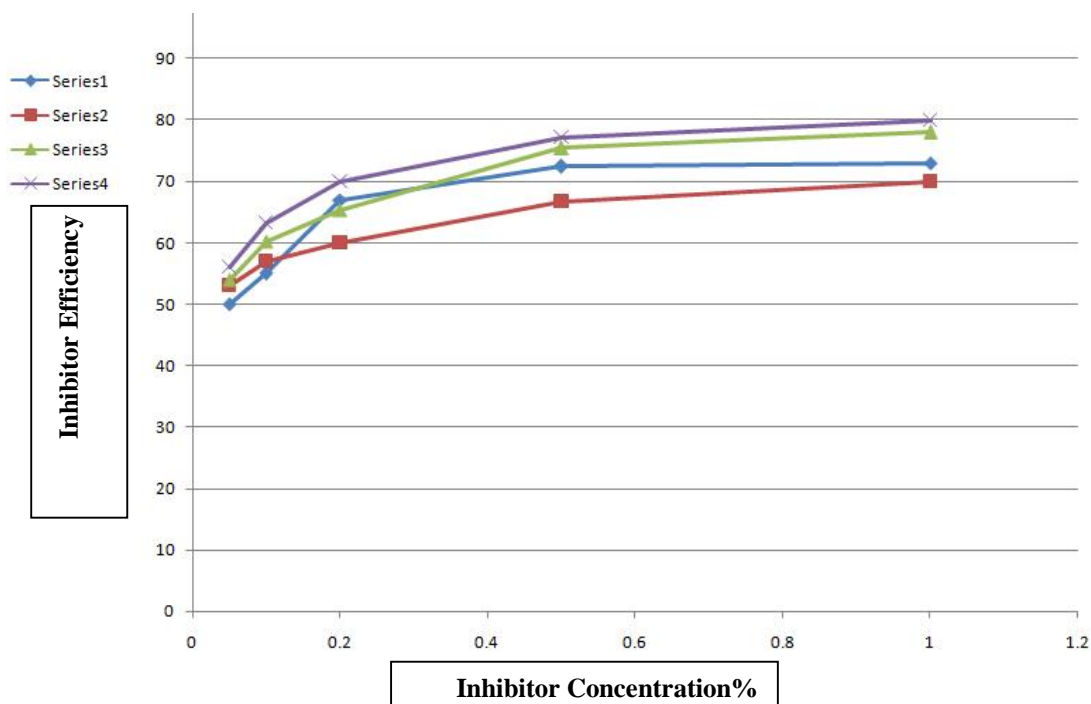


Figure (6). Effect of concentration of Aromatic compounds on their efficiency as inhibitors for API 5L X65 carbon steel (as received) in oilfield solution, containing different water content: 1-15% 2-25% 3- 35% 4-45%.

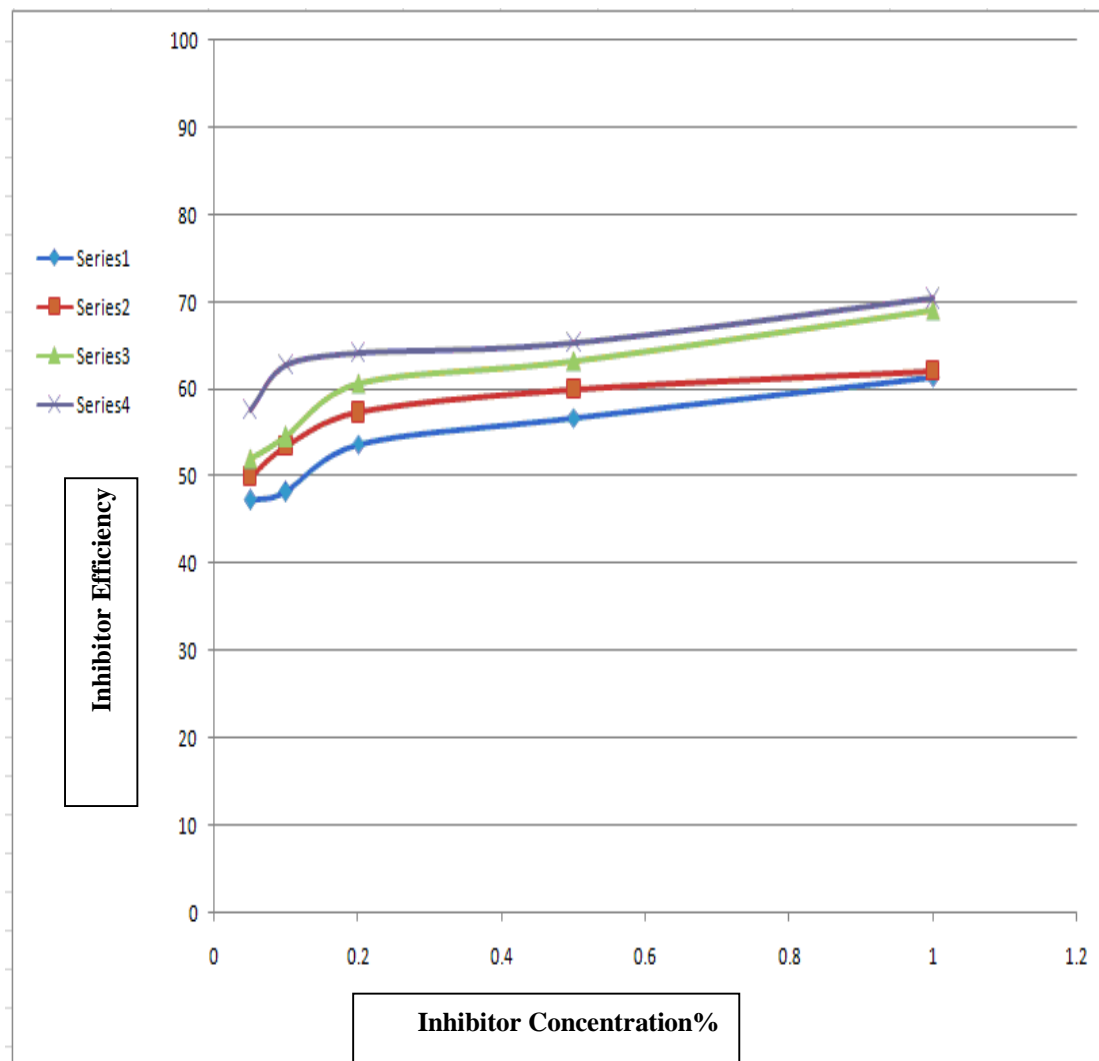


Figure (7). Effect of concentration of Aromatic compounds on their efficiency as inhibitors for API 5L X65 carbon steel (after quenching + tempering) in oilfield solution, containing different water content: 1-15% 2-25% 3- 35% 4-45%

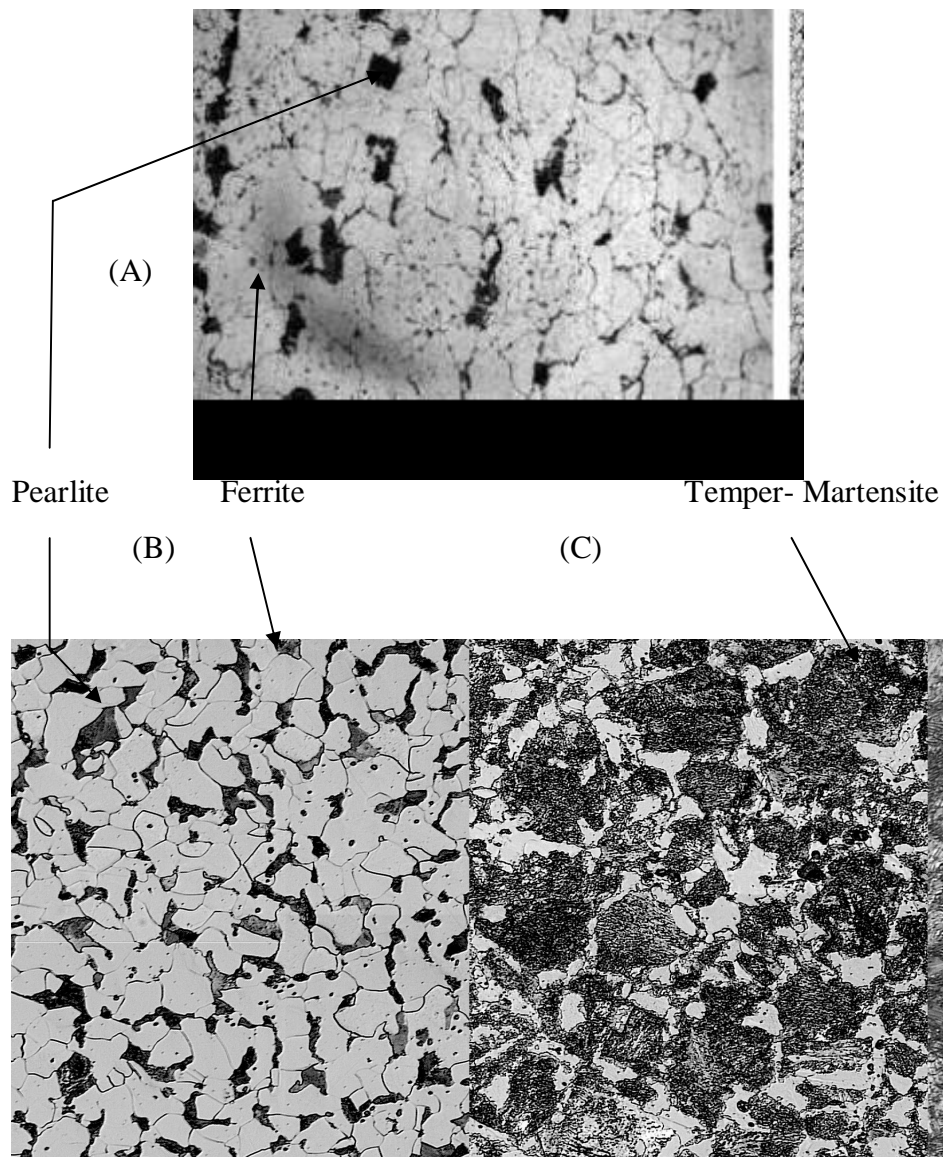


Figure (8). Optical micrographs of API 5L X65 carbon steel samples:{Approximately 250X}.

(A) as received (B) after annealing. (C) after quenching + tempering.

Table (4). The weight loss results of API 5L X65 carbon steel (as received) in oilfield solution, containing different water content: X1-15% X 2-25% X3- 35% X4-45% with different inhibitor concentrations (Y).

Inhibitor Concentration (Y)	Weight Loss, mg.			
	X1	X2	X3	X4
Nil	242	266	279	282
0.05	195	200	212	218
0.1	112	124	168	175
0.2	103	135	140	143
0.5	51	63	85	96
1.0	38	48	55	60

Table (5). the weight loss results of API 5L X65 carbon steel (After annealing) in oilfield solution, containing different water content: X1-15% X 2-25% X3- 35% X4-45% with different inhibitor concentrations (Y).

Inhibitor Concentration (Y)	Weight Loss, mg.			
	X1	X2	X3	X4
Nil	270	278	280	284
0.05	178	188	195	200
0.1	46	49	63	65
0.2	33	38	55	60
0.5	25	28	48	52
1.0	22	25	40	45

Table (6). The weight loss results of API 5L X65 carbon steel (After Quenching + Tempering) in oilfield solution, containing different water content: X1-15% X 2-25% X3- 35% X4-45% with different inhibitor concentrations (Y).

Inhibitor Concentration (Y)	Weight Loss, mg.			
	X1	X2	X3	X4
Nil	275	280	282	285
0.05	205	214	216	204
0.1	175	170	171	188
0.2	146	153	150	136
0.5	131	133	128	130
1.0	115	104	102	127

Table (7). The inhibitor efficiency results of API 5L X65 carbon steel(after annealing)) in oilfield solution, containing different water content:15% X1-X 2-25% X3-35%X4-45% with different inhibitor concentrations(Y).

Inhibitor Concentration (Y)	Weight Loss, mg.			
	X1	X2	X3	X4
0.05	67.8	65.4	63.2	60
0.1	75.0	67.5	65.8	63.5
0.2	73.9	70.5	69.6	64.5
0.5	76	75.8	72.8	66.4
1.0	84.8	84.2	82.1	80.6

Table (8). The inhibitor efficiency results of API 5L X65 carbon steel (as received) in oilfield solution, containing different water content: X1-15% X2-25% X3- 35% X4-45% with different inhibitor concentrations Y).

Inhibitor Concentration (Y)	Weight Loss, mg.			
	X1	X2	X3	X4
0.05	56	54	53	50
0.1	63.1	60.3	57	55
0.2	70	65.1	60	67
0.5	77.2	74.5	66.7	72.3
1.0	80	78.	70	73

Table (9). The inhibitor efficiency results of API 5L X65 carbon steel (After Quenching + Tempering) in oilfield solution, containing different water content: X1-15% X2- 25% X3- 35% X4-45% with different inhibitor concentrations (Y).

Inhibitor Concentration (Y)	Weight Loss, mg.			
	X1	X2	X3	X4
0.05	57.7	52	50	47.3
0.1	62.8	54.5	53.4	48.2
0.2	64.2	60.7	57.3	53.7
0.5	65.3	63.3	60.0	56.8
1.0	70.4	69.1	62.1	61.2

Study of the Condenser Performance in Al-Nassiriyah Thermal Power Plant

Khalid N. Hassan

Mechanical Engineering
Department
College of Engineering
University of Basrah

Qais A. Rishack

Mechanical Engineering
Department
College of Engineering
University of Basrah

Ahmed K. Mohammed

Mechanical Engineering
Department
College of Engineering
University of Basrah

Abstract

This paper includes a study of the performance of Al-Nassiriyah thermal power plant condenser. Which includes a calculations of the main variables of condenser (heat transfer, condensation rate, overall heat transfer coefficient and vapour pressure) by applying two dimensional mathematical model and depending on the empirical equations of heat transfer.

Comparison was made between the theoretical results for Al-Nassiriyah thermal power plant condenser before operation it (standard power plant) with practical data which taken from the plant for the second unit in year 2007. The comparison showed that there was a large difference between theoretical results and the values taken from the plant as a result to the effect of operation conditions.

Keywords : Thermal power plant , comparison, condensation.

المستخلص

يتضمن هذا البحث دراسة أداء مكثف محطة الناصرية الحرارية. تضمنت الدراسة حساب المتغيرات الرئيسية للمكثف (معدل انتقال الحرارة، معدل التكثيف، معامل انتقال الحرارة الإجمالي، ضغط البخار) وذلك باستخدام نموذج رياضي ثنائي الأبعاد بالاعتماد على المعادلات التجريبية لانتقال الحرارة. أجريت مقارنة بين النتائج النظرية لمكثف محطة الناصرية قبل تشغيلها مع قراءات أخذت من المحطة للوحدة الثانية ولسنة 2007 وقد تبين من خلال المقارنة ان هناك انحراف كبير بين النتائج النظرية والقيم المأخوذة من المحطة نتيجة لتأثير الظروف التشغيلية.

1. Introduction

Thermal power plants are responsible for the production of most of the electric power in the world, and even small increases in thermal efficiency could cause large saving of the fuel consumption. Therefore, large efforts were made to improve the efficiency of the power plant and one mean is by proper operation of the condenser. Surface condenser has a shell whose

ends are covered by the plates with condenser tubes. The ends of tubes are communicated with water boxes. The water boxes are divided by a partition into two sections of tubes, which form passes for water. Water is fed into the water boxes through an inlet pipe connection and first runs through the below partition. In the opposite water box, which has no partition, water flow is turned and moves in the opposite direction through the upper section condenser tubes, above the partition. When completing second pass, water enters the first water box and is drained through the outlet pipe connection ^[1].

Steam from the final stage of the steam turbine enters into the steam space of the condenser and moves, in cross flow, over the tubes. With cooling water, steam is condensed on the outer surface of the tubes causing a sharp drop of the specific volume of steam and, as a consequence, of low pressure (vacuum) is created in the condenser. The condensate rate runs down into the lower portion of the condenser and is collected in hotwell ^[2].

Chisholm et al., 1965, ^[3] developed a numerical method of evaluation heat and mass transfer coefficient and local heat fluxes in surface condensers. Al-ka'abiy, 2000, ^[4] Study The effect of Tigris water quality upon fouling rate in the condenser of Al-Daura power plant. AL-Chalaby and Rishack, 2001, ^[5] studied the reasons behind the loss in vacuum pressure of the condenser in Al-Hartha power plant. Tarrad and kamal, 2004, ^[6] studied the performance prediction of thermal power plant condensers in a quasi-two dimensional model and the proposed model showed a good agreement with field data. An experimental and analytical study was performed by Seungmin and Revankar, 2005, ^[7] to investigate the effect of non-condensable gas in a passive condenser system for three operation modes.

Al-Nassiriyah power plant was constructed by Technoprome (Russian) company which commissioned in 1979. It consists of four units. The electrical generating power (design power) for each unit is 210 MW. The unit condenser is of the surface tubular type and consists of two identical exchangers. Each carrying half load of the cooling water is forced through 8380 tubes, arranged in two passes and in a staggered configuration, the number of bays is 9 and the number of rows is 94 for all condenser. The design heat load is 210 MW and 27°C inlet cooling water temperature. The centrifugal pump with a maximum flow rate is 20000 m³/h for each pump and 1000 kW power input was used for cooling water. The condensers of Al-Nassiriyah power plant are surface condenser ^[8].

Table (1). Geometrical input data for condenser of Al-Nassiriyah thermal power plant.

Geometrical input data	value
External diameter of tube (m)	0.028
Internal diameter of tube (m)	0.026
Tube pitch (m)	0.035
Width of tube sheet (m)	4.45
Number of bays	9
Length of bay (m)	0.984, 0.876, 1.042, 1.042, 1.042, 1.042, 1.042, 0.876, 0.984
Number of tubes for condenser	8380
Number of rows for upper pass of condenser	46
Number of rows for lower pass of condenser	48
Number of tubes for upper pass of condenser	3874
Number of tubes for lower pass of condenser	4506

The main objectives of the present work are to:

1. Build a computer program (Fortran 90 language) to study the performance of thermal power plant condensers by calculating the main variables under various operating conditions which have direct effect on condenser performance, such as overall heat transfer coefficient, heat transfer rate and vacuum pressure.
2. Compare the theoretical results with the obtained data from Al-Nassiriyah power plant to know the reasons of the difference between them.

2. Theory

In the heat transfer analysis of the surface condenser, various thermal resistance in the direction of heat flow from the vapour to the cooling water are combined into the overall heat transfer coefficient (U_o). This thermal resistance includes cooling water resistance, fouling

(inside tube) resistance, tube wall resistance, condensing resistance and non-condensable gas resistance ^[9].

The heat flux can be calculated from:

$$Q = U_o \text{ LMTD} \quad (1)$$

The overall heat transfer coefficient that refers to the outside tube area may be expressed as:

$$\frac{1}{U_o} = \frac{d_o}{d_i h_i} + R_{fou} + \frac{d_o \ln\left(\frac{d_o}{d_i}\right)}{2 k_w} + \frac{1}{h_c} + \frac{1}{h_v} \quad (2)$$

Where:

R_{fou} : fouling resistance inside tube, in the present work, fouling factor is taken as (0.0-0.0005 $\frac{m^2 \cdot ^\circ C}{W}$), ^[10].

2.1 Forced Convection inside Tube

Petukhov as cited by ^[11] presented the results of a theoretical analysis of heat transfer coefficient in pipes to variable property fluids as:

$$h_i = \frac{Re_i^{0.8} Pr_i^{0.4} \left(\frac{\eta}{\eta_s}\right)}{1.07 + 12.7 \left(Pr_i^{\frac{1}{3}} - 1\right) \sqrt{\frac{\eta}{\eta_s}}} \left(\frac{k_i}{d_i}\right) \left(\frac{\mu_{i,b}}{\mu_{i,w}}\right)^{0.11} \quad (3)$$

Where:

$$Re_i = \frac{\rho_i u_i d_i}{\mu_i}$$

and

$$\eta = (1.82 \log(Re_i) - 1.64)^{-2}$$

$\mu_{i,b}$: Dynamic viscosity evaluated at bulk temperature.

$\mu_{i,w}$: Dynamic viscosity evaluated at wall temperature.

2.2 Nusselt equation for a laminar film

The following relation of Nusselt theory for the heat transfer coefficient for circular tube ^[12].

$$h_{CN} = 0.725 \left(\frac{\rho_c (\rho_c - \rho_v) h_{fg} g k_c^3}{d_o \mu_c (T_{cs} - T_w)} \right)^{1/4} \quad (4)$$

The cooling of the liquid below the saturation temperature can be accounted by replacing (h_{fg}) by the modified latent heat of condensation (h_{fg}^*) which is defined as ^[13]:

$$h_{fg}^* = h_{fg} + 0.68 C_{p_c} (T_v - T_w) \quad (5)$$

The condensate heat transfer coefficient can be calculated from Fujii equation as cited by ^[14],

$$h_c = \frac{0.9 (1 + G)^{1/3} + 0.728 F^{1/2}}{(1 + 3.44 F^{1/2} + F)^{1/4}} Re_{TP}^{1/2} \left(\frac{k_c}{d_o} \right) \quad (6)$$

Where:

$$Re_{TP} = \frac{\rho_c u_{\infty} d_o}{\mu_c} ,$$

$$G = \frac{\mu_c h_{fg}^*}{k_c (T_{cs} - T_w)} \left(\frac{\rho_v \mu_v}{\rho_c \mu_c} \right)^{1/4} \quad \text{and}$$

$$F = \frac{\mu_c h_{fg}^* d_o g}{u_{\infty}^2 k_c (T_{cs} - T_w)}$$

2.3 Effect of inundation in tube banks

During shell side condensation in tube bundles, the conditions are much different than for a single tube. As condensate flows by gravity to lower tubes in a bundle, the thickness of the liquid film at lower tubes becomes much bigger, this effect known as inundation effect. Kern derived a non-dimensional equation which accounted for the predominant physical mechanism as ^[15]:

$$\frac{h_{c,n}}{h_{c,1}} = \left(1 + \frac{\sum_{i=1}^{n-1} m_{cT,i}}{m_{cT,n-1}} \right)^{-0.16} \quad (7)$$

2.4 Mass transfer coefficient and Sherwood number

The dimensionless mass transfer coefficient or Sherwood number is defined as ^[16]:

$$Sh = \frac{\beta d_o}{\rho_{mix} D} \quad (8)$$

For condensation of vapour in the presence of a non-condensable gas, the condition that the surface is impermeable to the gas gives:

$$m_c = \beta (w_{v\infty} - w_{vcs}) / (1 - w_{vcs}) = \beta (w_{cs} - w_{\infty}) / w_{cs} \quad (9)$$

Where (m_c) is towards the surface, total vapour mass flux or condensation rate at the vapour condensate interface. Equations (8) and (9) give:

$$Sh = \frac{m_c d_o}{\rho_{mix} D} \left(\frac{w_{cs}}{w_{cs} - w_{\infty}} \right) \quad (10)$$

By taking

$$Q = m_c h_{fg}^* \quad (11)$$

Combining equations (10) and (11) give:

$$Q = h_{fg}^* \rho_{mix} \frac{D}{d_o} \left(\frac{w_{cs} - w_{\infty}}{w_{cs}} \right) Sh \quad (12)$$

Where (Sh) can be obtained from Rose equation ^[17]:

$$Sh = \left[\left(1 + 2.28 Sc^{1/2} \frac{(w_{cs} - w_{\infty})^{1/2}}{w_{\infty}} \right)^2 - 1 \right] \frac{w_{cs}}{2 (w_{cs} - w_{\infty})} Re_{mix}^{1/2} \quad (13)$$

Where:

$$Re_{mix} = \frac{\rho_{mix} u_{\infty} d_o}{\mu_{mix}}$$

and

$$Sc = \frac{\mu_{mix}}{\rho_{mix} D}$$

Assuming vapour as an ideal-gas mixture, the interface equilibrium conditions give ^[18]:

$$w_{cs} = \frac{P_{mix} P_{cs}}{P_{mix} \left[1 + \left(\frac{M_v}{M_a} \right) \right] P_{cs}} \quad (14)$$

The diffusion coefficient is obtained by ^[17]:

$$D = \frac{0.926}{P_{mix}} \left(\frac{T^{2.5}}{T + 245} \right) \quad (15)$$

Where T is taken at $(T_v + T_{cs})/2$ in (K) and P_{mix} in (Pa).

2.5 Velocity distribution in shell side of surface condenser

As vapour passes across the tubes in the shell side of the surface condenser, its velocity would change due to two reasons. Firstly; the reduction in the mass flow rate of vapour where it condensates around the tubes. Secondly; the change of flow area between the rows. Accordingly, the vapour velocity for the first row differs from that for other rows below ^[19]:

a) For the tube in the first row:

$$u_{\infty} = \frac{m_v + m_a}{\rho_v A_{vd}} \quad (16)$$

Where:

$$A_{vd} = w_{ts} L$$

b) For the next tube in the other rows:

$$u_{\infty(n+1)} = \frac{(m_v + m_a) - \sum_{i=1}^n m_{cr,i}}{\rho_{mix} A_{mv}} \quad (17)$$

Where A_{mv} is the mean void area of flow in the vapour space for an equivalent triangular pitch-tube layout, which defined as ^[19]:

$$A_{mv} = L (NTR_n - 1) \left(Pt - \frac{\pi d_o^2}{2\sqrt{3}Pt} \right) \quad (18)$$

The pressure amount at each tube in the column can be calculated from this equation ^[20]:

$$P_{mix_{n+1}} = P_{mix_n} - \left[\left(0.2 c_r^2 \frac{\dot{m}_v^2}{\rho_v} \right)_n - \left\{ \left(\frac{\dot{m}_v^2}{\rho_v} \right)_n - \left(\frac{\dot{m}_v^2}{\rho_v} \right)_{n+1} \right\} \right] \quad (19)$$

Where:

$$c_r = \frac{A_{vd}}{A_{mv}}$$

and

$$\dot{m}_v = \rho_v u_{\infty}$$

$$P_{vac} = \left[\frac{(P_{atm} - P_{mix})}{P_{atm}} \right] * 760 \quad (20)$$

2.6 Calculation method

The step by step method (this method divides the condenser into a number of bays and a number of rows, the calculation starts from upper pass where the vapour inlets to condenser and continuous from row to row towards the bottom in specified bay) is applied to calculate the performance of power plant condenser, the bays are numbered from cooling water inlet to condenser and the rows numbered from the top of condenser to the bottom.

Considering the heat flux which includes the convection inside tube, fouling resistance and wall resistance is:

$$Q = h_{iwf} (T_w - T_{in}) \quad (21)$$

Where:

$$h_{iwf} = \left(\frac{d_o}{d_i h_i} + \frac{d_o \ln\left(\frac{d_i}{d_o}\right)}{2 k_w} + R_{fou} \right)^{-1} \quad (22)$$

Where (h_i) calculate from equation (3).

Considering heat flux across condensate film as:

$$Q = h_c (T_{cs} - T_w) \quad (23)$$

Combining equations (23), (4), (6) and (7) give:

$$Q = C (T_{cs} - T_w)^{3/4} \quad (24)$$

Where (C) is parameter defined as:

$$C = Y * Z \quad (25)$$

Where:

$$Y = 0.725 \left(\frac{\rho_c (\rho_c - \rho_v) h_{fg} g k_c^3}{d_o \mu_c} \right)^{1/4} \left(1 + \frac{\sum_{i=1}^{n-1} m_{cr,i}}{m_{cr,n-1}} \right)^{-0.16} \quad (26)$$

The parameter (Z) is defined as:

$$Z = \frac{h_c}{h_{cN}} \quad (27)$$

$$Z = \frac{0.9 (1 + G)^{1/2} + 0.728 F^{1/2}}{h_{cN} (1 + 3.44 F^{1/2} + F)^{1/4}} Re_{TF}^{1/2} \left(\frac{k_c}{d_c} \right) \quad (28)$$

Considering heat flux through bulk of mixture as:

$$Q = h_v (T_v - T_{cs}) \quad (29)$$

Combining equations (29), (12) and (13) give:

$$Q = S (T_v - T_{cs})^{2/3} \quad (30)$$

Where (S):

$$S = h_{fg}^* \rho_{mix} \frac{D}{2 d_o} \left[\frac{1}{T_v - T_{cs}} \right]^{2/3} \left[\left(1 + 2.285 C^{1/3} \left(\frac{W_{cs} - W_{\infty}}{W_{cs}} \right) \right)^{1/2} - 1 \right] Re_{mix}^{1/2} \quad (31)$$

Combining equations (21), (24) and (30) gives:

$$\left[\frac{Q}{S} \right]^{3/2} + \left[\frac{Q}{C} \right]^{4/3} + \left[\frac{Q}{h_{iwf}} \right] = T_v - T_m \quad (32)$$

Or

$$Q_{new} = (T_v - T_m) / \left[\frac{Q_{old}^{1/2}}{S^{3/2}} + \frac{Q_{old}^{1/3}}{C^{4/3}} + \frac{1}{h_{iwf}} \right] \quad (33)$$

The overall heat transfer coefficient between vapour and cooling water is evaluated from:

$$U_o = \frac{Q}{T_v - T_m} \quad (34)$$

And The outlet temperature of cooling water (T_o) is evaluated from heat balance over tube as:

$$m_i C_{pi} (T_o - T_i) = \pi d_o L U_o LMTD \quad (35)$$

Where:

$$LMTD = \frac{(T_v - T_i) - (T_v - T_o)}{\ln \left(\frac{T_v - T_i}{T_v - T_o} \right)} = \frac{T_o - T_i}{\ln \left(\frac{T_v - T_i}{T_v - T_o} \right)} \quad (36)$$

Combining equation (35 and 36) gives:

$$T_o = T_v - \frac{T_v - T_i}{\exp\left(\frac{U_o \pi d_o L}{m_i C_{p_i}}\right)} \quad (37)$$

Calculate effectiveness of condenser which defined by the ratio of cooling water temperature differential throughout the condenser to the maximum temperature differential ^[5]:

$$\varepsilon_{eff} = \frac{T_o - T_{in}}{T_{vt} - T_{in}} \quad (38)$$

3. Results and discussion

a. Heat transfer

Figure (1) shows that the general trend of the curves for heat transfer rate with row number in upper pass, undergoes increasing from the first row to the row number (11), because of the number of tubes in the first row which have (58 tubes) is less than that in the row number (11) which have (84 tubes). Then the trend shows after decreasing as going down across the upper pass. This is because of steam pressure drop between the two rows results in a reduction in the overall heat transfer coefficient and, hence, a decrease in heat transfer rate.

Figure (2) shows that the heat transfer increases from the first row to the row number 16 in lower pass, this is because the number of tubes in the first row (78 tubes) is less than that in row number 16 which have (96 tubes). The trend of the curves is the same. The extreme drop in curves for lower passes in the rows number (35) and (36), because the number of tubes in these rows (38 tubes) less than that in the other rows. This makes the quantity of cooling water less than that in other rows, and that explains decreasing of heat transfer rate. The heat transfer rate approaches zero at row number (46) because of the condensation of all vapour and causing subcooling from this row to the last row.

b. Overall Heat Transfer Coefficient

Figure (3) shows the variation of the overall heat transfer coefficient (U_o) across the rows in the upper pass. The general trends of curves show a reduction in (U_o) as going down across the rows in upper pass. This is attributed to the increase in condensation resistance. The overall heat transfer coefficient in bay number (1) is larger than that in the other bays because of the small temperature difference between the vapour and cooling water.

Figure (4) describes the variation of overall heat transfer coefficient across the rows in the lower pass. There is a decrease in (U_o) as going down across the rows. This is due to the increase in all resistances as going down across the rows in the lower pass. The extreme drop

in curves for lower pass in the rows number (35) and (36), since the heat transfer in this rows are less than that in the other rows. The overall heat transfer coefficient in bay number (1) is larger than that in the other bays because it has the largest heat transfer rate.

c. Vacuum pressure

Figure (5) shows that the curves of vacuum pressure increase from the first row towards the end of the rows at the same trend for upper pass because of large pressure drop in this pass and this leads to a decrease in the vapour pressure and an increase in vacuum pressure and a decrease in the temperature of vapour.

Figure (6) illustrates the distribution of vapour vacuum pressure through the rows for lower pass. The vacuum pressure curves increases from first row to the vent and then decreases to the end of the rows because the pressure drop at the vent increases so that the pressure of vapour decrease and the vacuum pressure increase. The reason of the decrease in the vacuum pressure after the vent is due to the decrease in mass flow rate of vapour.

d. Comparison of results

Figure (7) shows that the calculated results which obtain from computer program (assume new power plant with fouling resistance equal to zero) and the operational results which obtained from the log sheet for Al-Nassiriyah power plant (five days per a month for several months in year 2007). The average was taken for these days in the month. The figure shows that the vacuum pressure for performance curve (new power plant) is greater than that for operational data and the difference between two curves about (20 mm Hg). The reason of this difference is the effect of operation factors.

Figure (8) illustrates the effectiveness of condenser with inlet cooling water temperature for calculated and operational curves. The calculated data obtained from computer program (assume new power plant) and the operational data obtain from the log-sheet for Al-Nassiriyah power plant. The figure shows that the difference between the two curves about 30 percent as a result to the effect of operational conditions and resistances such as fouling factor.

4. Conclusions

From study the performance of Al-Nassiriyah thermal power plant condenser can be noticed:

1. Heat transfer for the lower pass of condenser, where river water first enters, is higher than that for upper pass. While the overall heat transfer coefficient is lower, due to the increase in temperature difference between vapour and cooling water.
2. Comparison of the results shows a difference between the operational data and standard results (new power plant), this attributed to the age of power plant and due to the effect of operational factors.

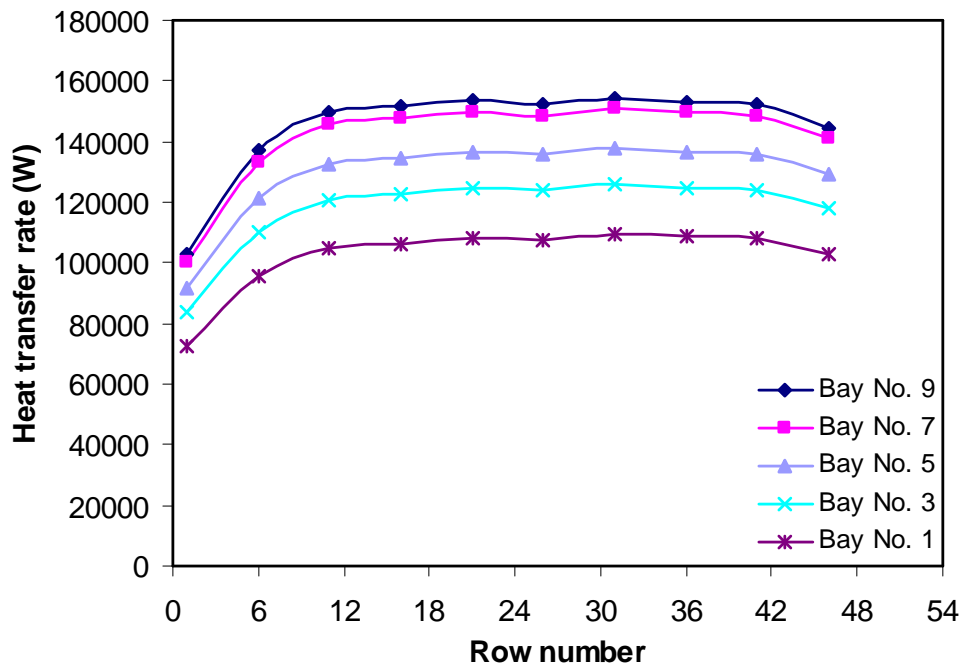


Figure (1). Heat transfer Vs. row number at different bay for upper pass.

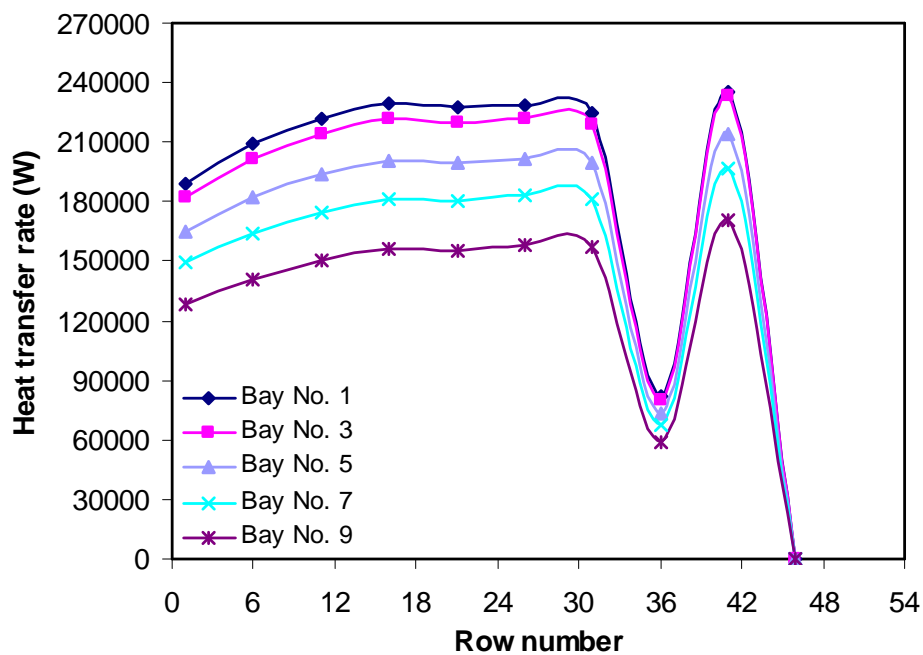


Figure (2). Heat transfer Vs. row number at different bay for lower pass.

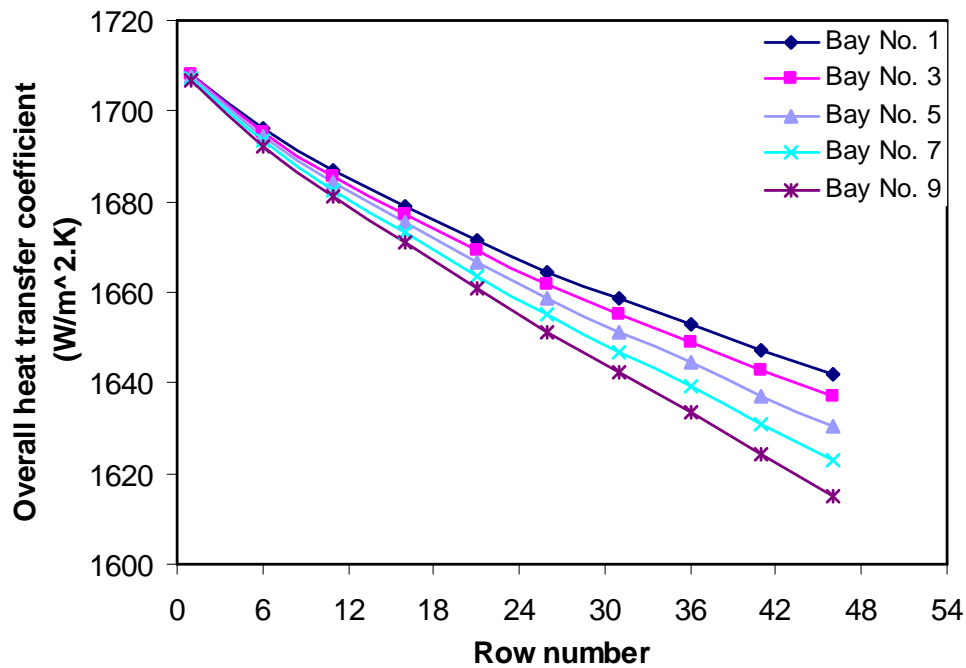


Figure (3). Overall heat transfer coefficient Vs. row number at different bay for upper pass.

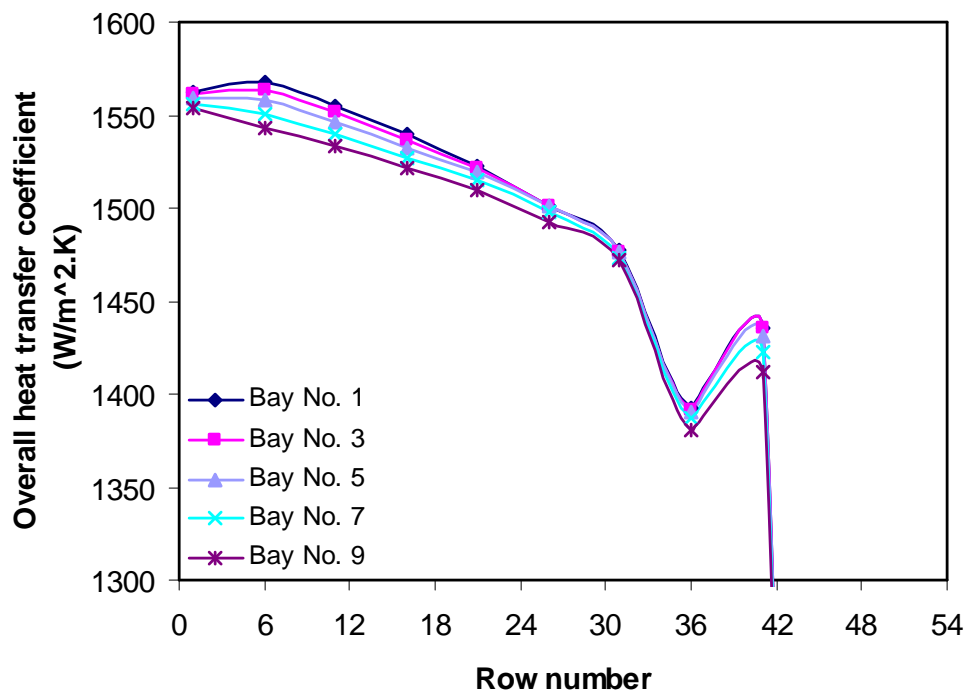


Figure (4). Overall heat transfer coefficient Vs. row number at different bay for lower pass.

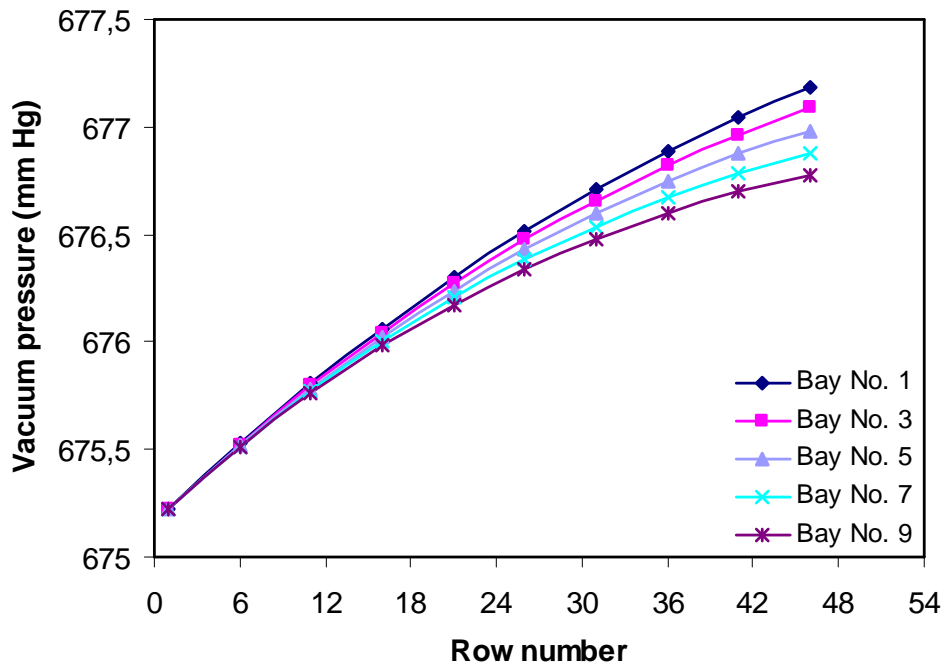


Figure (5). Vacuum pressure Vs. row number at different bay for upper pass.

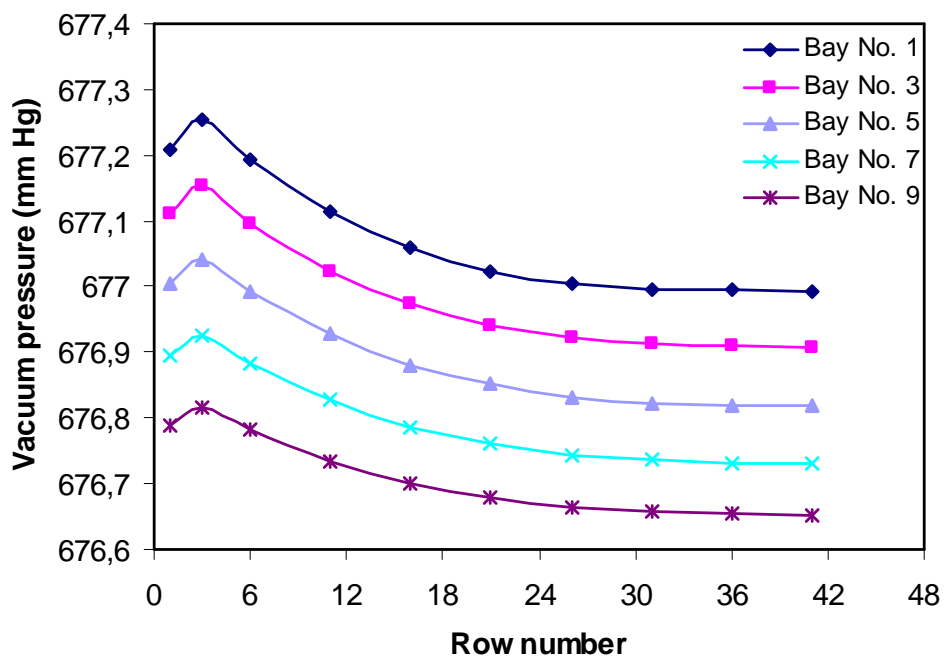


Figure (6). Vacuum pressure Vs. row number at different bay for lower pass.

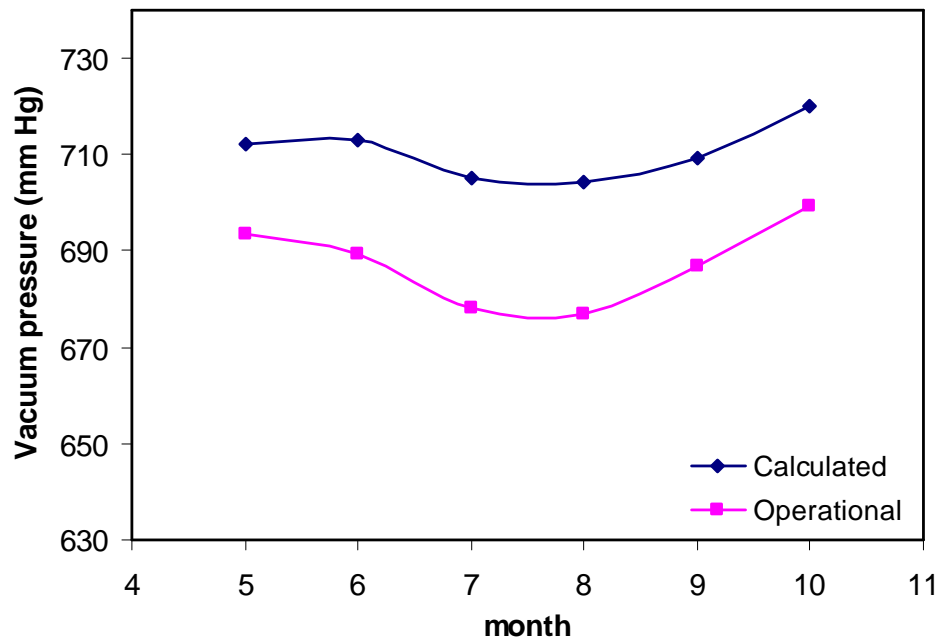


Figure (7). Vacuum pressure Vs. months for calculated and operational data.

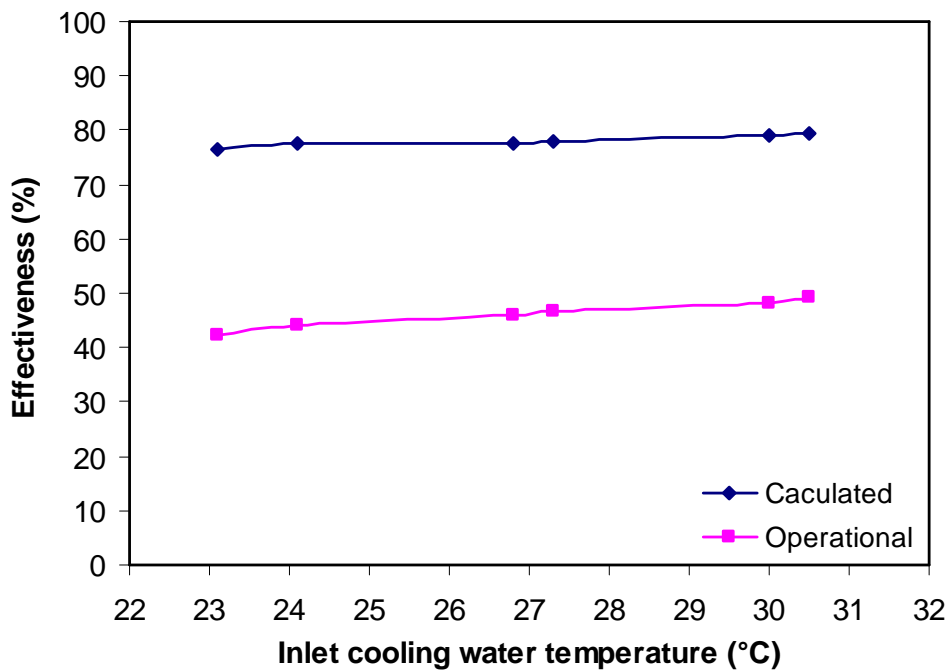


Figure (8). Effectiveness Vs. inlet cooling water temperature for calculated and operational data.

5. References

- [1] Ozisik M.N., 1985,"Heat Transfer: A Basic Approach", McGraw-Hill Book Company, International Edition.
- [2] Kostyuk A. and Frolov V., 1988,"Steam and Gas Turbines" Mir Publishers Moscow.
- [3] Chisholm D., Provan T.F. and Mitchell D., 1965,"Digital Computation Methods for Evaluating Heat Flux in Condensers", Journal of Mechanical Engineering Science, Vol.7, No.2, pp.177-184.
- [4] Al-Ka'abiy A.J.H., 2000,"A Study of the Performance of Al-Dura Power Plant Condenser and Its Relation with Water Cooling Problems", M.sc Thesis, University of Al-Mustansiriyah.
- [5] AL-Chalaby, A.A. and Rishack, Q.A. , 2001,"The Effect of High Fouling Rates and Subcooling on Surface Condenser", Eng. Technology, Suppl. Of Vol.20, No.4.
- [6] Tarrad A.H. and Kamal H.M., 2004,"A Model for Prediction of Surface Condenser Performance in Thermal Power Plants", Journal of Eng. And Development, Vol.8, No.3.
- [7] Seungmin Oh. and Revankar S.T., 2005,"Investigation of a Passive Condenser System of Advanced Boiling Water Reactor", 11th, Int. Topical Meeting on Nuclear Reactor Thermal-Hydraulics (Nureth-11) Popes Place Conference Center, University of Purdue.
- [8] Manual of Al-Nassiriyah Thermal power plant.
- [9] Davidson B.J., 1987,"Condensers for Large Turbines", in Aerothermodynamics of Low Pressure Steam Turbines and Condensers, Eds. Moore, Mj., and Severing, C.h., pp.217-251, Hemisphere.
- [10] Macnair E., 1981,"Fouling: Typical Experimental Results and Observations", power condenser heat transfer technology, Eds. By Marto P.J. and Nunn R.H., PP.431-438, Hemisphere.
- [11] Slecher C.A. and Rose M.W.,1975,"A Convenient Correlation for Heat Transfer to Constant and Variable Property Fluids in Turbulent Pipe Flow", Int. Journal Heat Mass Transfer, pp.677-683.
- [12] Owen R.G., Sardesai R.G., Smith R.A. and Lee W.C., 1983,"Gravity Controlled Condensation on a Horizontal Low-Fin Tube", in Condensers: Theory and Practice, Published by Inst. Chem. Eng. Symposium Series, no.75, pp.415-428.
- [13] Collier G.J., 1972,"Convective Boiling and Condensation", McGraw-Hill Book Company.

- [14] Rose J.W. , 1984,"Effect of Pressure Gradient in Forced Convection Film Condensation on a Horizontal Tube", Int. J. Heat Mass Transfer, vol.27, pp.39-47.
- [15] Chisholm D., 1981,"Modern Developments in Marine Condensers: Non-condensable gases", An Overview, in power condenser heat transfer technology, Eds. By Marto P.J. and Nunn R.H., PP.95-142, Hemisphere.
- [16] Lee W.C. and Rose J.W., 1983,"Comparison of Calculation Methods for Non-Condensing Gas Effects in Condensation on a Horizontal Tube", in Condensers: Theory and Practice, Published by Inst. Chem. Eng. Symposium Series, no.75, pp.342-351.
- [17] ASHRAE Fundamentals Handbook, ch.5, 1997,"Mass Transfer".
- [18] Rose J.W., 1980,"Approximate Equations for Forced Convection Condensation in the Presence of Non-Condensing Gas on a Flat Plate and Horizontal Tube", Int. J. Heat Mass Transfer, vol.23, pp.539-546.
- [19] Michael A.G., Lee W.C. and Rose J.W., 1992,"Forced Convection Condensation of Steam on a Small Bank of Horizontal Tubes", Trans. of ASME Journal of Heat Transfer, vol.114, pp.708-713.
- [20] Fujii T. , 1983,"Condensation in Tube Banks", in Condensers: Theory and Practice, I. Chem. E. Symp. Series, no.75, pp.3-22, Pergamon Press., London.

6. Nomenclature

A_{mv} : Mean void area in the vapour space (m^2)

A_{vd} : Cross-sectional area of the vapour duct (m^2)

c_p : Specific heat at constant pressure ($J/kg.K$)

c_r : Parameter defined by equation (19)

D : Molecular diffusion coefficient (m^2/s)

d_i : Inner tube diameter (m)

d_o : Outer tube diameter (m)

g : Gravitational acceleration (m/s^2)

h : Convective heat transfer coefficient ($W/m^2.K$)

h_{fg} : Latent heat of vapourization (J/kg)

h_{fg}^* : Modified latent heat of vapourization (J/kg)

k : Thermal conductivity ($W/m.K$)

L : Length of bays (m)

LMTD : Logarithmic mean temperature difference

M : Molecular weight ($kg/kg\ mole$)

m : Mass flow rate (kg/s)

\dot{m}_v : Mass velocity ($kg/m^2.s$)

NTR : Number of tubes in each row in the bundle

P : Pressure (Pa)

P_{vac} : vacuum pressure of vapour (mmHg)

Pr : Prandtl number

Pt : Tube pitch (m)

Q : Heat flux (W/m^2)

Re : Reynolds number

R_{fou} : Fouling resistance ($m^2.K/W$)

Sc : Schemidt number

Sh : Sherwood number

T : Temperature (K)

U_o : Overall heat transfer coefficient ($W/m^2.K$)

u : Velocity (m/s)

w : Mass fraction

w_{ts} : Width of tube sheet (m)

β : Mass transfer coefficient ($kg/s.m^2$)

μ : Dynamic viscosity(Pa.s)

ρ : Density (kg/m^3)

η : Parameter defined by equation (3)

ϵ_{eff} : Effectiveness

Subscript

a : Air

atm: atmosphere

CN : Nusselt

c : Condensate

cr : Condensation rate

cs : Vapour/condensate interface

i : Cooling water inside tube

m : Mean water temperature

mix : Mixture

n : Order of certain row

o : outlet

v : Vapour

vcs : Vapour at vapour condensate interphase

w : Tube wall

∞ : Free stream

Study of Mixed Convection Heat Transfer Inside a Vented Square Cavity with Inner Heated Cylinder

Falah A.Abood

Mechanical Engineering Department
College of Engineering
University of Basrah

Sana M. Shrama

Mechanical Engineering Department
College of Engineering
University of Basrah

Zainab K. Radhi

Mechanical Engineering Department
College of Engineering
University of Basrah

Abstract

The problem of mixed convection heat transfer for laminar air flow in a square cavity with inner heated cylinder is numerically analyzed by finite element method using software package (FlexPDF) to solve the conservation of governing equations. The right vertical wall is kept at constant temperature and the others are adiabatic. An external flow enters the cavity through an opening in the left vertical wall and exits from another opening in the right vertical wall. Results of streamlines, isotherms, average temperature and average Nusselt number of the heated wall are presented for $Ri = 0$ to 12 , $50 \leq Re \leq 200$, $Pr = 0.71$ and inlet position $hi = 0.2$. From the present analysis it is found that with increases of Re and Ri numbers the convective heat transfer becomes predominant over the conduction heat transfer. The results of streamlines and isotherms are compared with available result of Rahman et al.[8], a good agreement has been achieved.

Keywords : Heat transfer , mixed convection , fluid flow .

دراسة عملية انتقال الحرارة بالحمل المختلط داخل فجوة مربعة الشكل تحوي اسطوانة داخلية مسخنة

المستخلص

مسألة انتقال الحرارة بالحمل المختلط لجريان الهواء الطبقي داخل فجوة مربعة تحوي اسطوانة داخلية مسخنة تم تحليلها عددياً بطريقة العناصر المحددة باستخدام الحقيبة البرمجية (FlexPDF) لحل معادلات الحفظ الحاكمة. الجدار العمودي الأيمن للفجوة مثبت عند درجة حرارة ثابتة إما الجدران الأخرى فتكون معزولة. الجريان الخارجي يدخل الفجوة من خلال فتحة موجودة في الجدار العمودي الأيسر ويخرج عن طريق فتحة مثبتة بالجدار العمودي الأيمن. النتائج تمثلت بخطوط الجريان، خطوط ثابتة درجة الحرارة، معدل درجة الحرارة ومعدل رقم نسلت عند رقم ريتشارد Ri يتراوح من (0-12) ورقم رينولدز $50 \leq Re \leq 200$ ، رقم برانثل $Pr = 0.71$ عند موقع فتحة الدخول $hi = 0.2$. أظهرت النتائج

الحالية بأنه مع زيادة Re و Ri فإن عملية انتقال الحرارة بالحمل سائدة على عملية انتقال الحرارة بالتوصيل. نتائج خطوط الجريان وخطوط التحارر قورنت مع ما منشور في [8] Rahman et al. وأظهرت توافقاً جيداً.

1. Introduction

Mixed convection flows are present in many transport processes in nature and in engineering devices. Applications of mixed convection flows can be found in heat exchangers, nuclear reactors, solar energy storage, heat rejection systems, heaters and refrigeration devices, etc. Various geometries of fluid-filled rectangular enclosures have been theoretically and experimentally modeled in order to look at the effects of some design parameters on the thermal performance of simulated systems.

Thermal buoyancy forces play a significant role in forced convection heat transfer when the flow velocity is relatively small and the temperature difference between the surface and the free stream is relatively large. The buoyancy force modifies the flow and the temperature fields and hence the heat transfer rate from the surface. Problems of heat transfer in enclosures by free convection or combined free and forced convection have been the subject of investigations for many years. The influence of the physical characteristics of heat sources on the mixed convection heat transfer performance has been examined by many researchers. Kumar and Yuan [1] studied the laminar, two-dimensional mixed convection flow in a rectangular enclosure with inlet and outlet ports. Papanicolaou and Jaluria [2] investigated mixed convection in a cavity with a localized heat source.

Ajay and Jeffrey [3] studied mixed convection within a recirculating flow in an insulated lid-driven cavity of rectangular cross section (150mm X 450mm) and depth varying between 150mm and 600 mm, by appropriately varying the lid speed, the vertical temperature differential, and the depth by taking Gr/Re^2 ratios from 0.1 to 1000. The mean flux values over the entire lower boundary were analyzed to produce Nusselt number and Stanton number correlations which should be useful for design applications. Raji and Hasnaoui [4] reported the results of a numerical study of air laminar mixed convection in a rectangular cavity, including radiation, for $10^3 \leq Ra \leq 5 \times 10^6$ and $5 \leq Re \leq 5000$.

Mixed convection in an open cavity with a heated wall bounded by a horizontally insulated plate was studied by Oronzio et al. [5], three basic heating modes are considered: the heated wall is on the inflow side, the heated wall is on the opposing flow, and the heated wall is the horizontal surface of the cavity (heating from below). Manca et al. [6] worked out a numerical investigation of three different cases of mixed convection in a channel with an open cavity for various ratios of channel opening and cavity height and the range of governing parameters

were $0.1 \leq Ri \leq 100$, and $Re=100$ and 1000 . Investigated a mixed convection problem in a two sided lid-driven and differentially heated cubic for Ri number range $0.01 \leq Ri \leq 10$.

The finite-element procedure based on the projection method for solving the primitive variables form of the Navier-Stokes equations and energy equation in three dimensions, proposed by Lo et al [7], used numerical algorithm involves the operator splitting technique, balance tensor diffusivity (BTD), the Runge-Kutta time-stepping method, and a bi-conjugate gradient iterative solver. Two benchmark flows, lid-driven cavity flow and laminar flow over a 3-D backward-facing step, are validated with numerical solutions. Mixed-convection problem in a two-sided lid-driven and differentially heated cubic cavity is investigated. The Richardson number in the range $0.01 \leq Ri \leq 10$, serves as a measure of the relative importance of forced- and natural-convection modes on the heat transfer.

Rahman et al. [8] investigated mixed convection in a vented enclosure. An external fluid flow enters the enclosure through an opening in the left vertical wall and exits from another fixed opening in the right vertical wall. For mixed convection, the significant parameters are Grashof number (Gr), Richardson number (Ri) and Reynolds number (Re) by which different fluid and heat transfer characteristics inside the cavity are obtained. Results show that with the increase of Re and Ri the convective heat transfer become dominant. Behzad et al. [9] studied the numerically investigate the cooling performance of electronic devices with an emphasis on the effects of the arrangement and number of electronic components. The analysis uses a two dimensional rectangular enclosure under combined natural and forced convection flow conditions and considers a range of Rayleigh numbers. Rahman et al. [10] studied the mixed convection in cavity contains a heat conduction horizontal square block located inside the cavity. The investigations are conducted for various values of geometric size, location and thermal conductivity of the block under constant Re and Pr . The results indicated that the average Nusselt number and the temperature at the center of solid block are strong dependet on the system configurations studied under different geometrical and physical conditions. The objective of this study to analyze the effects of Richardson and Reynolds numbers and the location of the inner heated cylinder on the heat transfer characteristics of laminar mixed convection. Finite element method has been used to solve the governing equations by using software package (FlexPDF).

density variations causing a body force term in the momentum equation. The governing equations for steady mixed convection flow can be expressed in the dimensionless form as:

$$\frac{\partial U}{\partial X} + \frac{\partial V}{\partial Y} = 0 \quad (1)$$

$$U \frac{\partial U}{\partial X} + V \frac{\partial U}{\partial Y} = -\frac{\partial P}{\partial X} + \frac{1}{\text{Re}} \left(\frac{\partial^2 U}{\partial X^2} + \frac{\partial^2 U}{\partial Y^2} \right) \quad (2)$$

$$U \frac{\partial V}{\partial X} + V \frac{\partial V}{\partial Y} = -\frac{\partial P}{\partial Y} + \frac{1}{\text{Re}} \left(\frac{\partial^2 V}{\partial X^2} + \frac{\partial^2 V}{\partial Y^2} \right) + \text{Ri} \theta \quad (3)$$

$$U \frac{\partial \theta}{\partial X} + V \frac{\partial \theta}{\partial Y} = \frac{1}{\text{Pr Re}} \left(\frac{\partial^2 \theta}{\partial X^2} + \frac{\partial^2 \theta}{\partial Y^2} \right) \quad (4)$$

Where X and Y are the coordinates varying along horizontal and vertical directions respectively, U and V are the velocity components in the X and Y directions respectively, θ is the dimensionless temperature and P is the dimensionless pressure.

The dimensionless parameters in the above equations can be given as:

$$X = \frac{x}{L}, \quad Y = \frac{y}{L}, \quad U = \frac{u}{u_i}, \quad V = \frac{v}{u_i}, \quad \theta = \frac{T - T_i}{T_h - T_i}, \quad P = \frac{p}{\rho u_i^2}$$

$$\text{Pr} = \frac{\nu}{\alpha}, \quad \text{Ri} = \frac{g\beta(T - T_i)L}{u_i^2}, \quad \text{Re} = \frac{L u_i}{\nu}$$

Where ρ , β , ν , α and g are the fluid density, coefficient of volumetric expansion, kinematics viscosity, thermal diffusivity, and gravitational acceleration, respectively. The following boundary conditions are used:

Inlet: $U = 1, V = 0, \theta = 0$

Exit: Convective boundary condition, $P = 0$

At the cavity walls (except the right vertical wall): $U=V=0, \quad \partial\theta/\partial n = 0$

At the heated right vertical wall: $U=V=0, \theta=1$

At the cylinder $U=V=0, \theta=1$

The local Nusselt number at the heat wall is defined as:

$$\text{Nu}_L = \frac{\partial\theta}{\partial n} \quad (5)$$

The average Nusselt number

$$\overline{Nu} = \frac{1}{L_h} \int_0^{L_h} Nu_L ds \quad (6)$$

And the bulk average temperature in cavity is defined as

$$\theta_{av} = \int \frac{1}{V} \theta dV \quad (7)$$

Where L_h is the length of the heat wall and \bar{V} is the cavity volume.

4. Numerical solution

The code FlexPDE is used to perform the numerical calculations using finite element method to analyze the laminar mixed convection heat transfer and fluid flow in a vented square cavity contain of inner heated cylinder. It is well known in the numerical solution field that the set of equations above (1-4) may be highly oscillatory or even sometimes undetermined because of inclusion of the pressure term in the momentum equations. In finite element method there is a derived approach with purpose of stabilizing pressure oscillations and allowing standard grids and elements. This approach enforces the continuity equation and the pressure to give the following, what called, penalty approach [11].

$$\nabla^2 P = \gamma \left(\frac{\partial U}{\partial X} + \frac{\partial V}{\partial Y} \right) \quad (8)$$

Where γ is a parameter that should be chosen either from physical knowledge or by other means [11]. A most convenient value for γ was attained in this study to be $1E5\mu/L^2$. Hence, the continuity eq. (1) is excluded from solution system and replaced by eq. (8).

5. Validation

5.1 Software validation

The grid dependency is checked together with continuity equation and obtained results showed an exactly validation of the velocity distribution for a grid size obtained by imposing

an accuracy of 10^{-4} . This accuracy is a compromised value between the result accuracy and the time consumed in each run. The girded domain for $Ri=1$, $Re=100$ is shown in Figure (2a) and the distribution of $\left(\frac{\partial U}{\partial X} + \frac{\partial V}{\partial Y}\right)$ over the domain is presented in Figure (2b).

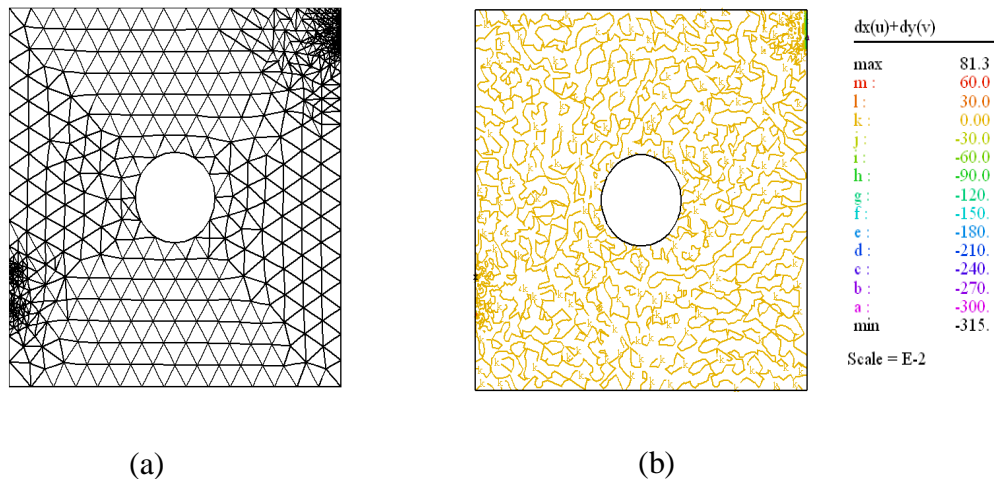


Figure (2). (a) grid distribution over the domain (b) validation of continuity equation .

5.2 Numerical results validation

A computational model is validated for mixed convection heat transfer by comparing the correlation of mixed convection in ventilated cavity with uniform heat flow in left wall performed by Rahman et al. [8]. Figure (3) shows the comperasion of the flow and thermal fields between the present investigation and Rahman et al.[8]. Figure (4) also shows another comparison of average dimensionless temperature as a function of Richarson numbers at $Re=100$, $hi=0.2$ and $Pr=0.71$. The results show a good agreement and from these comparisons it can be decided that the current code can be used to predict the flow field for the present problem.

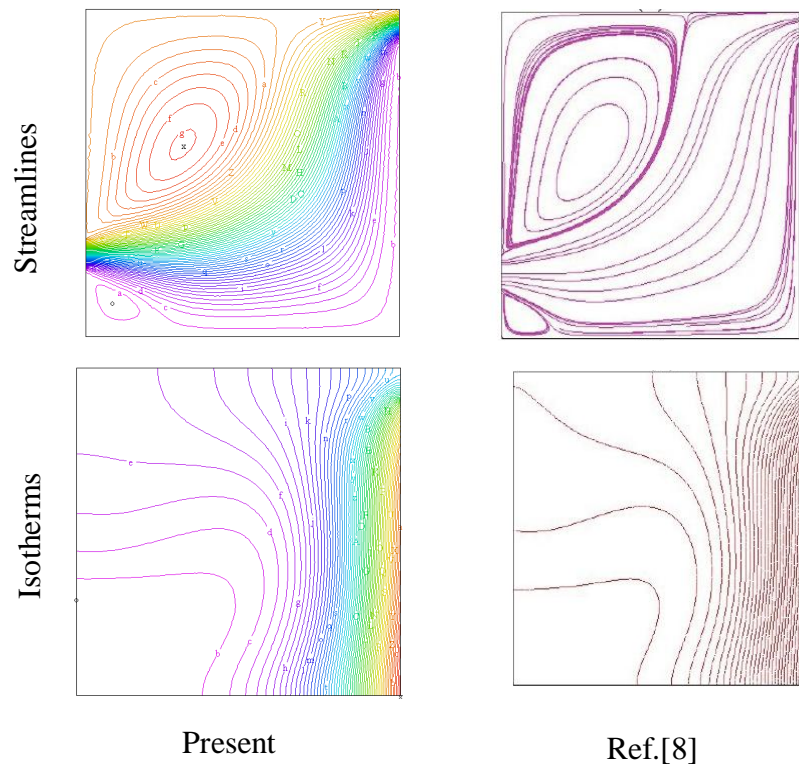


Figure (3). Comparison of streamlines and isotherms for validation at $Pr = 0.71$, $Re = 100$, $Ri = 1.0$ with the results of Ref.[8].

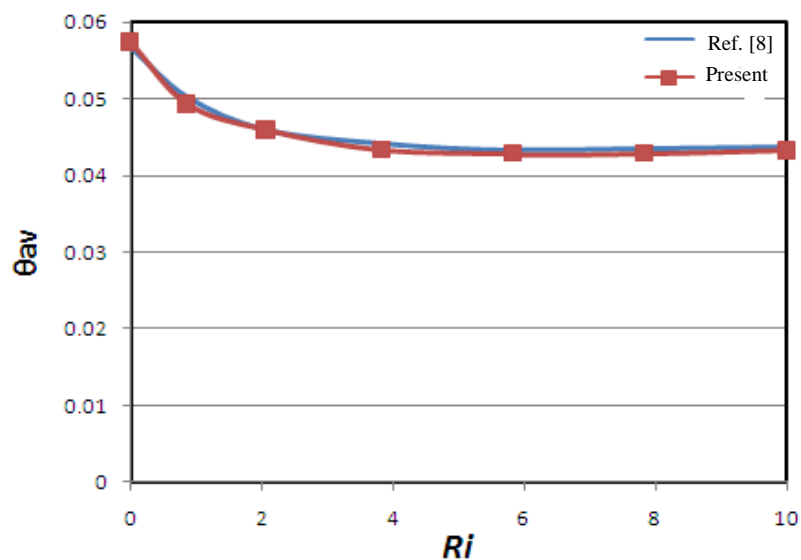


Figure (4). Comparison of average temperature as a function of Richardson numbers at for validation at $Pr = 0.71$, $Re = 100$ and $hi=0.2$ with the results of Ref.[8].

6. Results and discussion

A numerical study has been performed to analyze the laminar mixed convection heat transfer and air flow in a vented square cavity consist of a horizontal rod . Effect of the parameters such as Richardson number Ri , Reynolds number Re and the location of the inner cylinder on the heat transfer and fluid flow of the enclosure have analyzed.

6.1. Flow and temperature fields

Figure (5) show distribution of streamlines (on the left) and isotherms (on the right) for various locations of the inner heated cylinder at $Ri=1$ and $Re=100$. It can be seen from this figure that two circulating cells are formed, one is located at the top of the inlet port and the other cell at the bottom. The size of the upper cell is decreases when the inner cylinder location is moved from the lower part of the cavity $e1=0.25$ toward the upper part $e3=0.75$. Also figures show that for $e1=0.25$, the streamlines are arranged in parallel lines and cover all the surface of the cylinder while its cover the lower space of the cavity when the cylinder is moved toward the upper part of the enclosure. The formation of circulating cell is because of the mixing of the fluid due to buoyancy driven and convective current

Similarly the isotherms (on the right) are shown in the Figures (5a), (5b) and (5c) for different locations of inner heated cylinder $e1=0.25$, $e2=0.5$ and $e3=0.75$ respectively. For $e1=0.25$ (the heated cylinder is located at the bottom part of cavity) the wide heated region is concentrated at the space between the cylinder and the left vertical wall of the cavity. With moving the inner cylinder toward the upper, the isotherms are observed to have plum like distribution and occupy the upper part of the inner heated cylinder due to the growth of the thermal boundary layer. Because the effect of the location of inner heated cylinder, the isotherms show wavy variation and no vortices are observed contours.

Figure (6) shows the effect of Reynolds number on flow and isothermal fields at $Ri=1$ and the location of the inner cylinder at the center of the cavity ($e2=0.5$). It can be seen from Figure (6) (left) the intensity of the streamlines is increased with increasing of Re . Also with increases Re a bi-cellular vortex is seen just above and bottom the inlet port and occupies the left top and bottom space of the cavity. For isotherms this Figure show that with increasing of Reynolds number, the curvature of the isotherms lines is increased at the region which cover all the space between the heated walls due to dominant of forced convection. For a low value of Re a plum like distribution of isotherms is formed near the upper part of the heated cylinder and its direction is inclined to the right. As Re increases, the direction of the plum is

changed to the left. This indicated that with low Re the effect of the buoyancy is increased leading to reducing the air density and induced the flow toward the exit.

Figure (7) shows the effect of Richardson number on the distribution of streamlines and isotherms at $Re=100$. Figure (7) (left) is depicted that the cellular motion just above the inlet port and the intensity of the stream lines are increased with increasing of Ri . It can be seen from this figure the plum like distribution of the hot isothermal lines is increased with increasing of Ri and cover most the space between the heated surfaces. The distribution of isotherms in the cavity at higher Ri is significantly different from that at lower values of Ri , because the buoyancy induced convection becomes more dominant.

6.2 Heat transfer characteristics

Plot of the average temperature (θ_{av}) of the fluid in cavity as a function of Re , at $Ri=1$ for different locations of inner cylinder is shown in Figure (8). It can be seen that the average temperature (θ_{av}) is decreased with increasing of Re due to the dominant of forced convection. It is clearly from this figure that the maximum values of average temperature of fluid is occurred when the inner cylinder is located at the center but when it moves toward the upper the values of the average temperature is decreased. This is because a significant effect of free convection when the inner cylinder is located at the center. This is because of a large heated area is cover most space of the cavity.

Figure (9) illustrate the variation of θ_{av} with Ri at $Re=100$. It has been observed that the average temperature of the fluid increases with increasing of Ri . When the cylinder moves closer to the upper cavity that transfers less than when it moves to the lower due to the secondary heat source that enhanced the natural convection at the lower part of the enclosure. The average Nusselt number at the hot wall of the enclosure as a function of Reynolds number for different locations of inner cylinder is shown in Figure (10). It observed that the value of Nusselt number increases with increasing of Re , also the \overline{Nu} increases with moving the inner cylinder toward the upper location due to dominant of forced convection .

The effect of Richardson number on the average Nusselt number at heated vertical wall for different locations of inner cylinder at $Re=100$ is shown in Figure (11). For all locations of cylinder when Ri increases the average Nusselt number is gradually increases and the higher values of Nusselt number are observed for the upper location of heated cylinder. The behaviors results due to decrease of the average bulk fluid temperature when the heated cylinder in the upper location.

7. Conclusion

A numerical investigation is made of laminar mixed convection in a square cavity with concentric heated horizontal cylinder. The results are obtained for wide ranges of Richardson number (Ri) from 0 to 12 and range of Reynolds number (Re) from 50 to 200.

In view of the obtained results, the following findings have been summarized:

- The location of the solid cylinder has significant effect on the flow and thermal fields. The value of average Nusselt number is the highest in the mixed convection when the cylinder is located near the top wall of the cavity.
- The values of θ_{av} decreases with the increasing Re and with decreasing of Ri for different locations of the cylinder.
- The average Nusselt number at the heated surface is the highest for the highest value of Re and Ri.

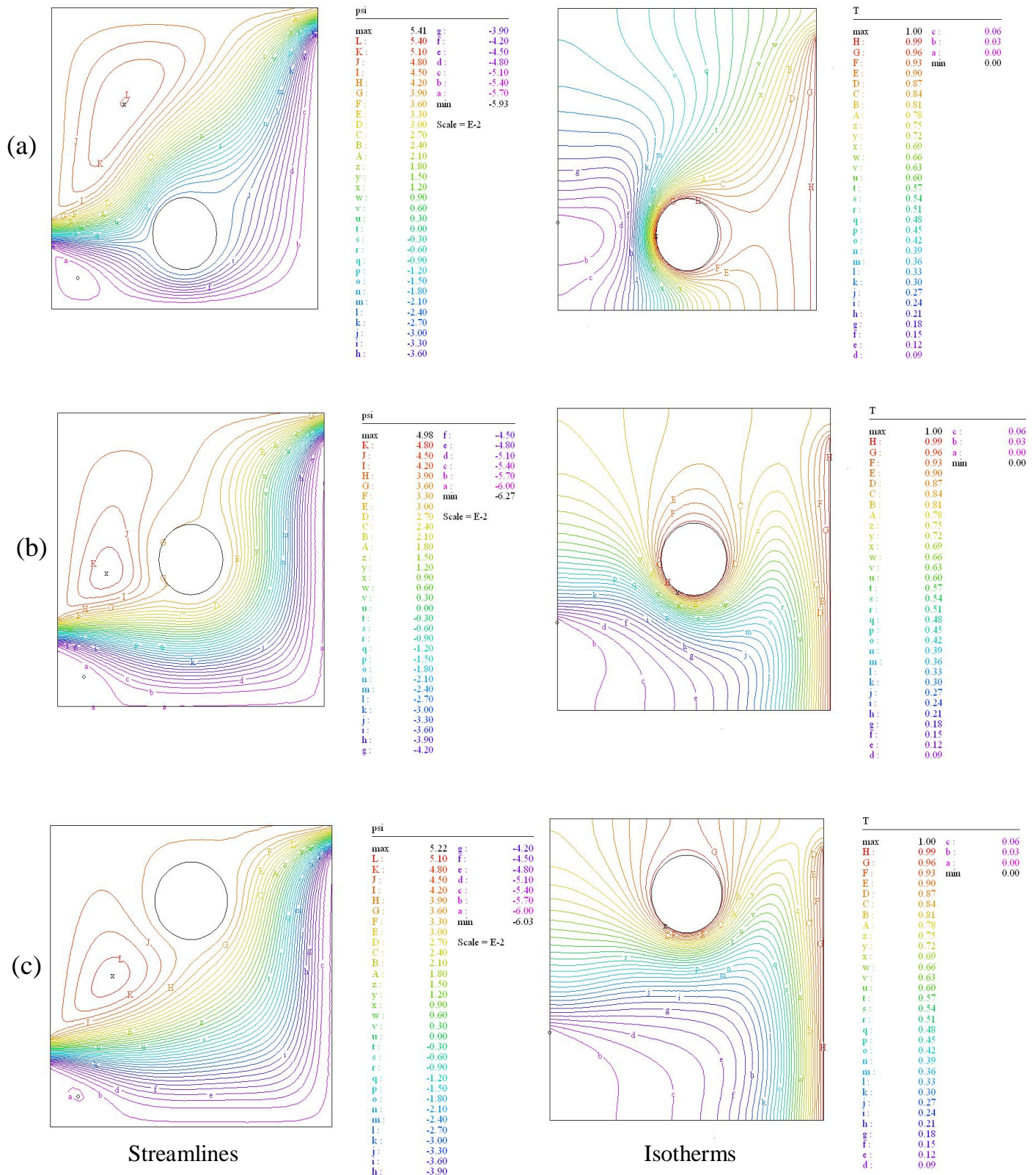
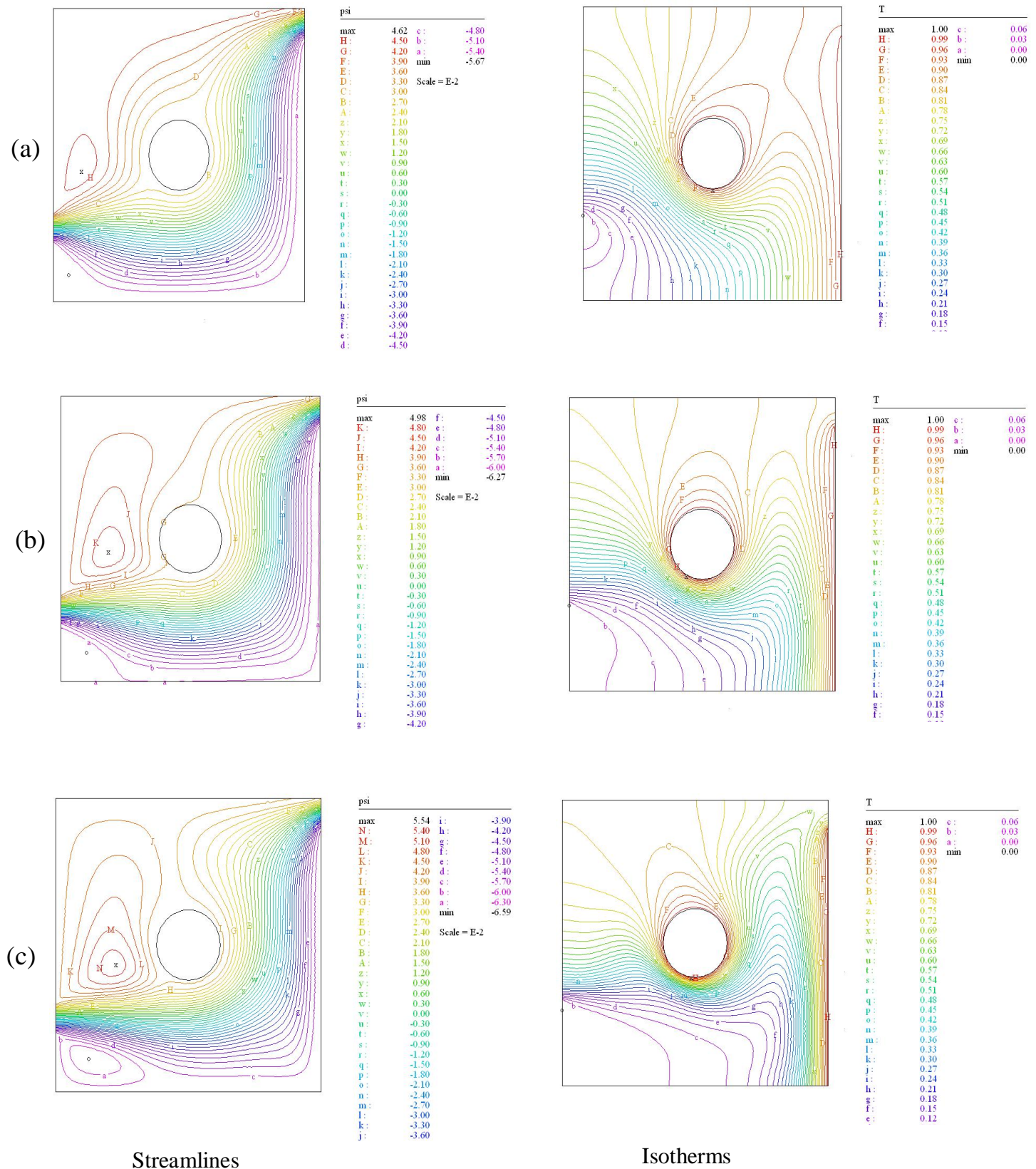
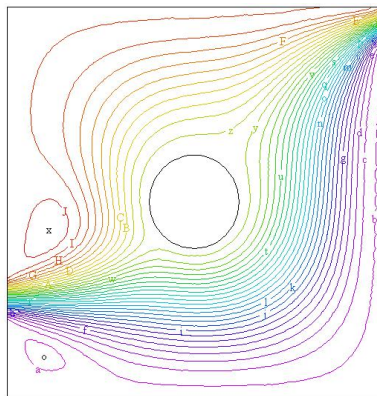


Figure (5). Streamlines(left) and isotherms(right) at $Ri=1$ and $Re=100$, (a) lower location ($e_1=0.25$), (b) central location ($e_2=0.5$), (c) upper location ($e_3=0.75$).



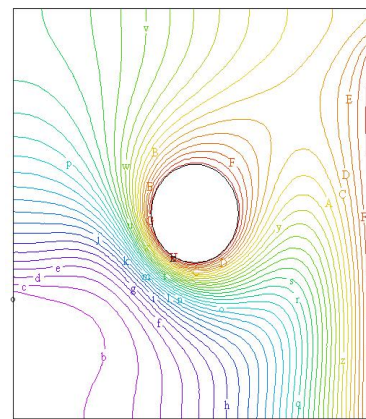
Figure(6). Streamlines (left) and isotherms (right) at $Ri=1$, (a) $Re =50$, (b) $Re=100$, (c) $Re=200$.

(a)



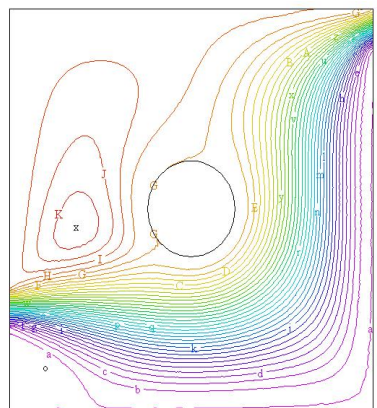
psi			
max	5.02	e:	-4.50
J:	4.80	d:	-4.80
I:	4.50	c:	-5.10
H:	4.20	b:	-5.40
G:	3.90	a:	-5.70
F:	3.60	min	-5.80
E:	3.30		
D:	3.00		
C:	2.70		
B:	2.40		
A:	2.10		
z:	1.80		
y:	1.50		
x:	1.20		
w:	0.90		
v:	0.60		
u:	0.30		
t:	0.00		
s:	-0.30		
r:	-0.60		
q:	-0.90		
p:	-1.20		
o:	-1.50		
n:	-1.80		
m:	-2.10		
l:	-2.40		
k:	-2.70		
j:	-3.00		
i:	-3.30		
h:	-3.60		
g:	-3.90		
f:	-4.20		

Scale = E-2



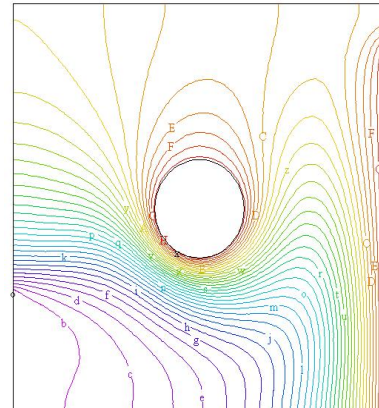
T			
max	1.00	c:	0.06
H:	0.99	b:	0.03
G:	0.96	a:	0.00
F:	0.93	min	0.00
E:	0.90		
D:	0.87		
C:	0.84		
B:	0.81		
A:	0.78		
z:	0.75		
y:	0.72		
x:	0.69		
w:	0.66		
v:	0.63		
u:	0.60		
t:	0.57		
s:	0.54		
r:	0.51		
q:	0.48		
p:	0.45		
o:	0.42		
n:	0.39		
m:	0.36		
l:	0.33		
k:	0.30		
j:	0.27		
i:	0.24		
h:	0.21		
g:	0.18		
f:	0.15		

(b)



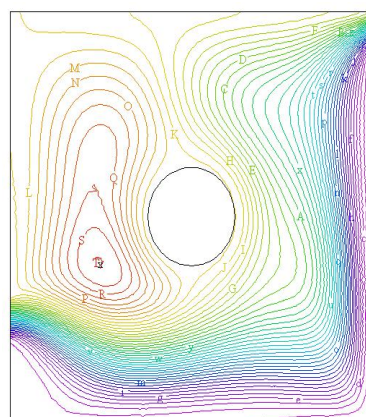
psi			
max	4.98	f:	-4.50
K:	4.80	e:	-4.80
J:	4.50	d:	-5.10
I:	4.20	c:	-5.40
H:	3.90	b:	-5.70
G:	3.60	a:	-6.00
F:	3.30	min	-6.27
E:	3.00		
D:	2.70		
C:	2.40		
B:	2.10		
A:	1.80		
z:	1.50		
y:	1.20		
x:	0.90		
w:	0.60		
v:	0.30		
u:	0.00		
t:	-0.30		
s:	-0.60		
r:	-0.90		
q:	-1.20		
p:	-1.50		
o:	-1.80		
n:	-2.10		
m:	-2.40		
l:	-2.70		
k:	-3.00		
j:	-3.30		
i:	-3.60		
h:	-3.90		

Scale = E-2



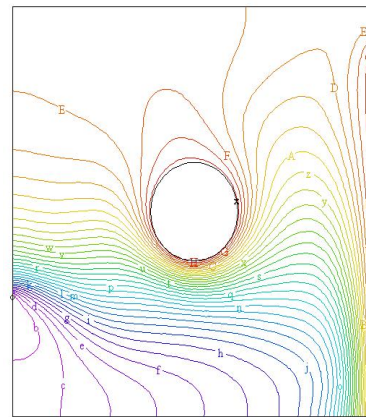
T			
max	1.00	c:	0.06
H:	0.99	b:	0.03
G:	0.96	a:	0.00
F:	0.93	min	0.00
E:	0.90		
D:	0.87		
C:	0.84		
B:	0.81		
A:	0.78		
z:	0.75		
y:	0.72		
x:	0.69		
w:	0.66		
v:	0.63		
u:	0.60		
t:	0.57		
s:	0.54		
r:	0.51		
q:	0.48		
p:	0.45		
o:	0.42		
n:	0.39		
m:	0.36		
l:	0.33		
k:	0.30		
j:	0.27		
i:	0.24		
h:	0.21		
g:	0.18		
f:	0.15		

(c)



psi			
max	5.12	o:	-4.20
T:	5.10	n:	-4.50
S:	4.80	m:	-4.80
R:	4.50	l:	-5.10
Q:	4.20	k:	-5.40
P:	3.90	j:	-5.70
O:	3.60	i:	-6.00
N:	3.30	h:	-6.30
M:	3.00	g:	-6.60
L:	2.70	f:	-6.90
K:	2.40	e:	-7.20
J:	2.10	d:	-7.50
I:	1.80	c:	-7.80
H:	1.50	b:	-8.10
G:	1.20	a:	-8.40
F:	0.90	min	-8.47
E:	0.60		
D:	0.30		
C:	0.00		
B:	-0.30		
A:	-0.60		
z:	-0.90		
y:	-1.20		
x:	-1.50		
w:	-1.80		
v:	-2.10		
u:	-2.40		
t:	-2.70		
s:	-3.00		
r:	-3.30		

Scale = E-2



T			
max	1.00	c:	0.06
H:	0.99	b:	0.03
G:	0.96	a:	0.00
F:	0.93	min	0.00
E:	0.90		
D:	0.87		
C:	0.84		
B:	0.81		
A:	0.78		
z:	0.75		
y:	0.72		
x:	0.69		
w:	0.66		
v:	0.63		
u:	0.60		
t:	0.57		
s:	0.54		
r:	0.51		
q:	0.48		
p:	0.45		
o:	0.42		
n:	0.39		
m:	0.36		
l:	0.33		
k:	0.30		
j:	0.27		
i:	0.24		
h:	0.21		
g:	0.18		
f:	0.15		

Streamlines

Isotherms

Figure (7). Streamlines (left) and isotherms (right) at $Re = 100$, (a) $Ri=0$, (b) $Ri=1$, (c) $Ri=12$.

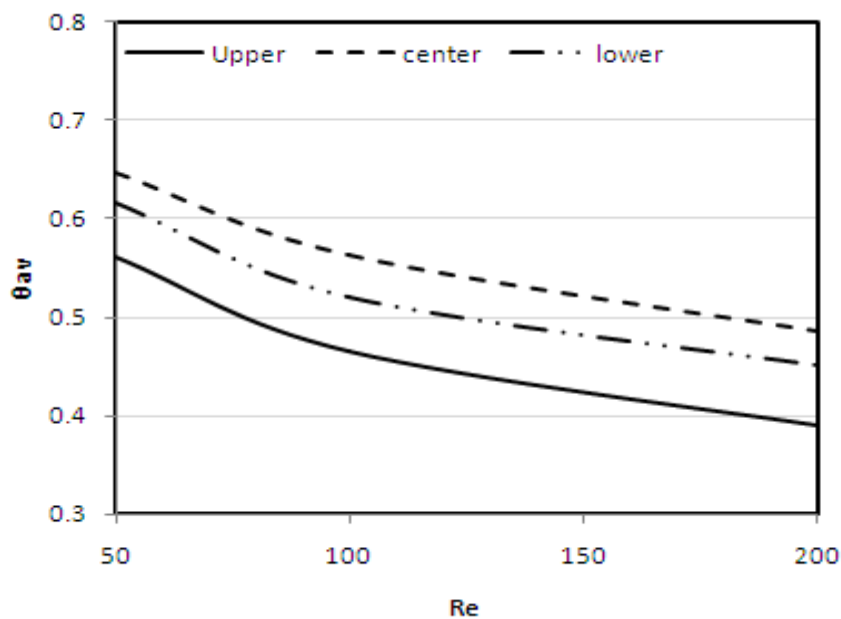


Figure (8). Variation of average fluid temperature with Reynolds numbers at $Ri=1$ for different location of inner cylinder .

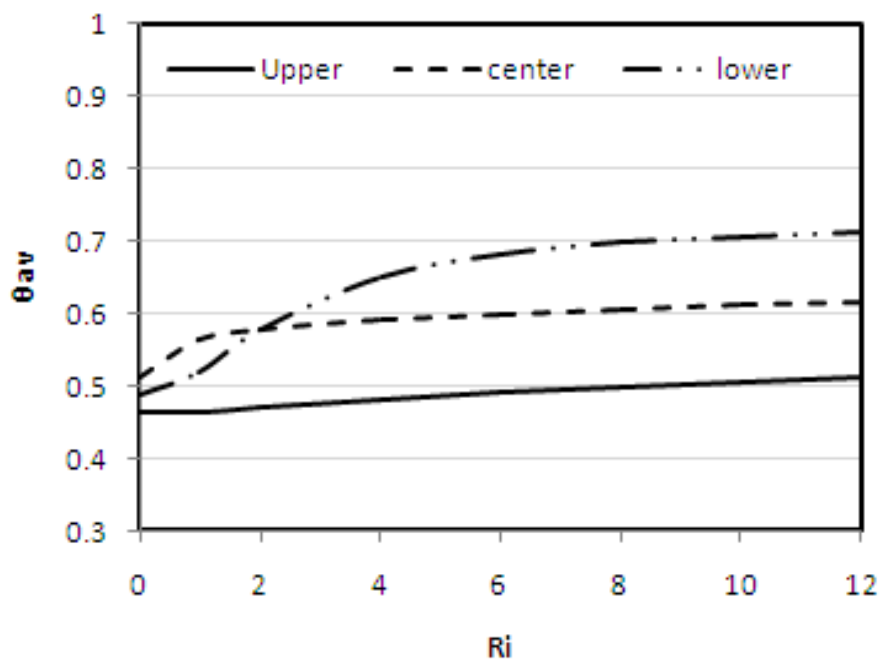


Figure (9). Variation of average fluid temperature with Richardson numbers at $Re=100$ for different location of inner cylinder.

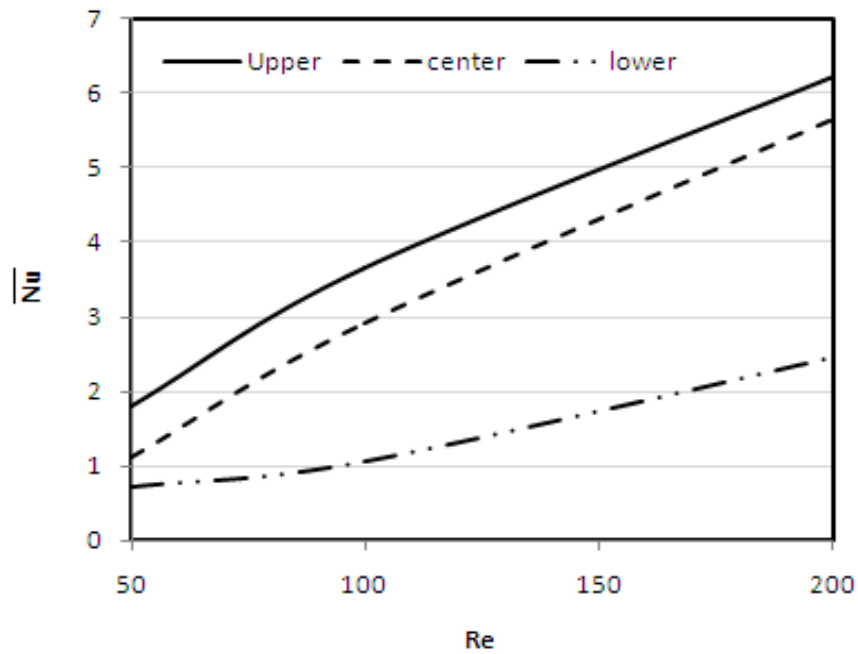


Figure (10). Variation of average Nusselt number with Re for different location of inner cylinder at $Ri=1$ at the heated wall .

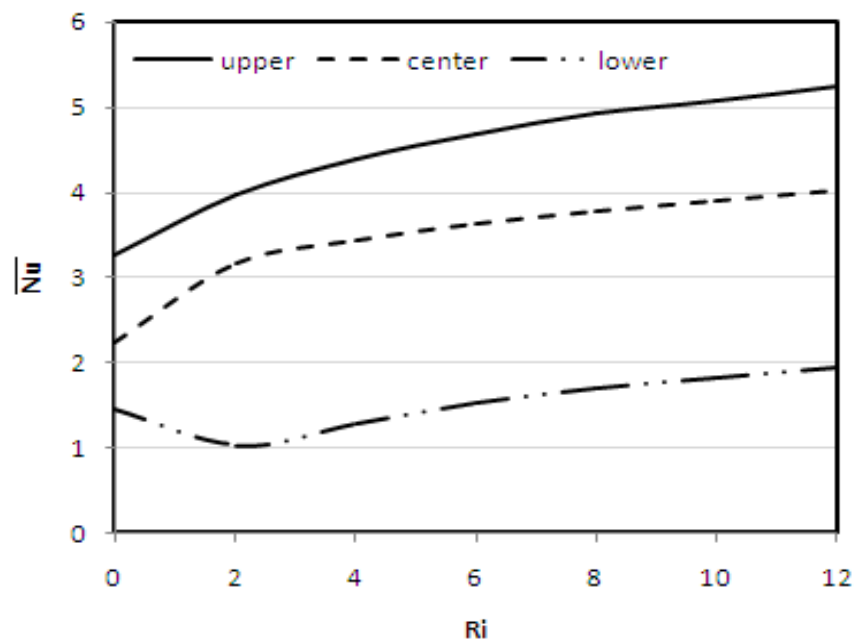


Figure (11). Variation of average Nusselt number with Ri for different location of inner cylinder at $Re=100$ at heated wall .

8. References

- [1] Kumer, R., Yuan, T.D.,1989,"Re- circulating mixed convection flows in rectangular cavities" AIAA J. Thermophys. Heat Transfer. Vol3:321-329.
- [2] Papnicolaou, E. ,and Jaluai,Y.,1993,"Mixed convection from a localized heat source in a cavity with conducting walls" A numerical study. Numerical heat transfer , part A. Vol.23 463-484.
- [3] Ajay K. Prasad and Jeffrey R. Koseff,1996," Combined forced and natural convection heat transfer in a deep lid-driven cavity flow",Int. J. Heat and fluid flow 17:460-467.
- [4] Raji, A.,and Hasnaoui, M.,2001,"combined mixed convection and radiation in ventilated cavities"Engineering computation, Int.J.computer.Aided Eng. Software.Vol.18(7) 922-949.
- [5] Oronzio M., Sergio N.,Khalil K.,and Kambiz V.,2003,"Effect of Heated Wall Position on Mixed Convection in a Channel With an Open Cavity", Numerical Heated Transfer ,Part A, 43: 259-282.
- [6] Manca, O., Nardin, S.,Khanafer, K.,Vafai,K.,2003,"Effect of heat wall position on mixed convection in a channel with an open cavity" Numerical heat transfer. A.43 259-282
- [7] D. C. Lo, D. L. Young, and Y. C. Lin,2005 , " Finite-Element Analysis of 3-D Viscous Flow and Mixed-Convection Problems by the Projection Methomd", Numerical Heat Transfer, Part A, 48: 339–358.
- [8] M. M. Rahman, M. A. Alim, M. A. H. Mamun, M. K. Chowdhury and A. K. M. S. Islam ,2007, "Numerical Study of Opposing Mixed Convection in a Vented Enclosure", ARPN Journal of Engineering and Applied Sciences, VOL. 2, NO. 2.
- [9] Behzad and Saiied Mostafa,2008," Numerical Simulation of Mixed Convection in a Rectangular Enclosure With Different Numbers and Arrangements of Discrete Heat Sources", The Arabian Journal for Science and Engineering, Vol. 33, NO. 1B.
- [10] Md.M.Rahman ,M.Alim, S.Saha, M.K.Chowdhury,2009, "Effect of the Presence of Heat Conducting Horizontal Square Block on Mixed Convection inside a Vented Square Cavity ", Nonlinear Analysis Modelling and Control ,Vol.14,No.4,531-548.
- [11]Langtangen H.P., Mardal K.A. and Winther R.,2002, "Numerical methods for incompressible viscous flow ",Advances in water Resources 25 1125-1146.

9. Nomenclature

c_p	specific heat of the fluid at constant pressure ($\text{Jkg}^{-1} \text{K}^{-1}$)
g	gravitational acceleration (ms^{-2})
h_i	inlet port location
H_i	non-dimensional inlet port location
w	height of the inflow and outflow openings (m)
k	thermal conductivity of the fluid ($\text{Wm}^{-1} \text{K}^{-1}$)
L	length of the cavity (m)
L_s	length of the heated wall
Nu	Average Nusselt number
N	non-dimensional distance
p	pressure (N/m^2)
P	non-dimensional pressure, $p/\rho u_i^2$
Pr	Prandtl number, ν/α
Ra	Rayleigh number, $Gr \cdot Pr$
Re	Reynolds number, $u_i L / \nu$
Ri	Richardson number, Gr/Re^2
T	temperature (K)
T_h	Hot temperature (K)
T_i	Inlet temperature (K)
θ	non-dimensional temperature, $(T-T_i)/(T_h-T_i)$
θ_{av}	average non-dimensional temperature
u, v	velocity components (ms^{-1})
U, V	non-dimensional velocity components, $u/u_i, v/u_i$
V	cavity volume
x, y	Cartesian coordinates (m)
X, Y	non-dimensional Cartesian coordinates, $x/L, y/L$

Greek symbols

α	thermal diffusivity, $k/\rho C_p$ (m^2s^{-1})
β	thermal expansion coefficient (K^{-1})
ρ	density of the fluid (kgm^{-3})
ν	kinematic viscosity of the fluid (m^2s^{-1})

Subscripts

av	average
s	heated surface
i	inlet state